Aalto University

Aaltodoc
OPEN ACCESS

This is an electronic reprint of the original article.
This reprint may differ from the original in pagination and typographic detail.

Author(s): Hofer, Werner A. & Foster, Adam S. & Shluger, Alexander L.

Title: Theories of scanning probe microscopes at the atomic scale

Year: 2003

Version: Final published version

Please cite the original version:

Hofer, Werner A. & Foster, Adam S. & Shluger, Alexander L. 2003. Theories of scanning probe microscopes at the atomic scale. Reviews of Modern Physics. Volume 75, Issue 4. 1287-1331. ISSN 0034-6861 (printed). DOI: 10.1103/revmodphys.75.1287.

Rights: © 2003 American Physical Society (APS). This is the accepted version of the following article: Hofer, Werner A. & Foster, Adam S. & Shluger, Alexander L. 2003. Theories of scanning probe microscopes at the atomic scale. Reviews of Modern Physics. Volume 75, Issue 4. 1287-1331. ISSN 0034-6861 (printed). DOI: 10.1103/revmodphys.75.1287, which has been published in final form at http://journals.aps.org/rmp/abstract/10.1103/RevModPhys.75.1287.

All material supplied via Aaltodoc is protected by copyright and other intellectual property rights, and duplication or sale of all or part of any of the repository collections is not permitted, except that material may be duplicated by you for your research use or educational purposes in electronic or print form. You must obtain permission for any other use. Electronic or print copies may not be offered, whether for sale or otherwise to anyone who is not an authorised user.

Theories of scanning probe microscopes at the atomic scale

Werner A. Hofer

Surface Science Research Centre, The University of Liverpool, Liverpool, L69 3BX, United Kingdom

Adam S. Foster

Laboratory of Physics, Helsinki University of Technology, P.O. Box 1100, Helsinki 02015, Finland

Alexander L. Shluger

Department of Physics and Astronomy, University College London, Gower Street, London WC1E 6BT, United Kingdom

(Published 20 October 2003)

Significant progress has been made both in experimentation and in theoretical modeling of scanning probe microscopy. The theoretical models used to analyze and interpret experimental scanning probe microscope (SPM) images and spectroscopic data now provide information not only about the surface, but also the probe tip and physical changes occurring during the scanning process. The aim of this review is to discuss and compare the present status of computational modeling of two of the most popular SPM methods—scanning tunneling microscopy and scanning force microscopy—in conjunction with their applications to studies of surface structure and properties with atomic resolution. In the context of these atomic-scale applications, for the scanning force microscope (SFM), this review focuses primarily on recent noncontact SFM (NC-SFM) results. After a brief introduction to the experimental techniques and the main factors determining image formation, the authors consider the theoretical models developed for the scanning tunneling microscope (STM) and the SFM. Both techniques are treated from the same general perspective of a sharp tip interacting with the surface—the only difference being that the control parameter in the STM is the tunneling current and in the SFM it is the force. The existing methods for calculating STM and SFM images are described and illustrated using numerous examples, primarily from the authors' own simulations, but also from the literature. Theoretical and practical aspects of the techniques applied in STM and SFM modeling are compared. Finally, the authors discuss modeling as it relates to SPM applications in studying surface properties, such as adsorption, point defects, spin manipulation, and phonon excitation.

CONTENTS

I. Introduction 1288
II. Experimental Setups 1288
III. Main Factors Determining Image Formation 1291
A. Controling interactions 1291
B. Tunneling current 1291
C. Bias voltage 1292
D. Electrostatic forces 1292
1. Effect of electrostatic forces in scanning tunneling microscopy 1292
2. Macroscopic electrostatic forces in scanning force microscopy 1293
E. Chemical forces 1294
F. Magnetic forces 1294
G. Summary 1295
IV. Model Development 1295
A. The surface 1296
B. The tip 1296
1. Idealized tips 1297
2. Modeling of real tips 1297
3. Combining microscopic and macroscopic tip models 1299
C. Tip-surface interaction 1299
1. van der Waals forces 1299
2. Calculating microscopic forces 1300
D. Modeling currents 1301
1. Tersoff-Hamann approach 1301
2. Perturbation approach 1301
3. Easy modeling: applying the Tersoff-Hamann model 1302
4. Magnetic tunneling junctions 1303
5. Landauer-Bütticker approach 1304
6. Keldysh-Green's-function approach 1304
E. Modeling oscillations 1304
F. Generating a theoretical surface image 1305
G. Summary 1305
V. Studying the Surface 1305
A. Metal surfaces 1306
B. Semiconductor surfaces 1308
1. Silicon surfaces 1308
2. Binary semiconductor surfaces 1309
C. Insulating surfaces 1309
1. The calcium fluoride (111) surface 1310
a. Tip characterization with force curves 1311
b. Simulating scanning 1311
c. Standard images 1312
d. Distance dependence of images 1314
e. Ideal silicon tip 1317
2. $CaCO_3(10\bar{1}4)$ surface 1318
D. Thin insulating films 1320
1. NaCl trilayer on Al(111) surface 1320
2. MgO thin films on Ag(001) surface 1320
3. NaCl thin films on Cu(111) surface 1321
VI. Studying Surface Properties 1321
A. Adsorbates on surfaces 1322

0034-6861/2003/75(4)/1287(45)/$35.00 ©2003 The American Physical Society

1. $C_4O_3H_2$ on Si(100) (2×1) surface 1322
2. O on Fe(100) surface 1323
B. Point defects 1324
C. Surface magnetism 1324
1. Mn surface 1324
2. NiO surface 1325
D. Spin manipulation 1326
E. Phonon excitations 1326
F. Electron dynamics 1327
VII. Conclusion and Outlook 1327
Acknowledgments 1327
References 1327

I. INTRODUCTION

Scanning probe methods have developed into ubiquitous tools in surface science, and the range of phenomena studied by these techniques is continuing to grow. These include surface topography, electronic and vibrational properties, film growth, measurements of adhesion and strength of individual chemical bonds, friction, studies of lubrication, dielectric and magnetic properties, contact charging, molecular manipulation, and many other phenomena from the micrometer down to the subnanometer scale. The family of scanning probe microscope (SPM) techniques is very diverse, with different methods specializing in different surface properties. In this review, we shall focus on the two most commonly used techniques—scanning tunneling microscopy and scanning force microscopy. In both techniques a sharp tip is interacting with the surface and a topographic surface image is produced by scanning. However, the parameters controlling the image formation are different. In a scanning tunneling microscope (STM) the control parameters of operation are the tunneling current and/or the voltage, whereas in a scanning force microscope (SFM) the control parameter is the force between tip and sample. In both cases information about the system under research is encoded in a change of these parameters as the tip scans along the surface. The highly nontrivial relationship between these variables and the physical environment they reveal is the main topic of this review.

While early research in these fields often took experimental results at face value, many seemingly paradoxical results have now taught experimentalists to be cautious and even skeptical when they are confronted with an image. This is where theoretical modeling has proven to be essential and a driving force in any progress made. In addition, SPM methods increasingly employ other methods of analysis like external magnetic fields or electron/phonon excitations, so that ever more subtle changes of the current in an STM, or the force in an SFM need to be measured and accounted for. In itself this poses tremendous challenges to experimental methods and thus drives the development of new tools to keep track of subtle changes. As the complexity of the experimental techniques continues to increase, experimental and theoretical groups have started to work together, realizing that both sides of a problem need to be studied in order to arrive at sustainable models. The aim of theory is to provide an understanding of the basic principles of operation and the origins of image contrast, and to interpret particular experimental images. In this paper we review the potentials and pitfalls of different approaches and hope to give newcomers and nonspecialists some sense of how experimental results can be backed by sophisticated theoretical models. We also discuss the real computational cost of these models and where the current frontier lies in our abilities and our understanding of the physical processes. We compare theoretical modeling of two of the most popular SPM methods—scanning tunneling microscopy and scanning force microscopy—from a common perspective, and demonstrate many similarities of these two methods. However, when discussing applications of the methods, we focus on those demonstrating true atomic resolution, and in particular for the SFM, this has only been achieved using a noncontact SFM (NC-SFM) in ultrahigh-vacuum (UHV) conditions.

We shall limit our discussion to working methods, which is to say we do not consider in full detail the large number of published papers which contain theoretical suggestions and propose new methods that have not yet been implemented. In principle, it is the goal of theory to develop a reliable model that can be used to interpret experimental images without resorting to direct simulation. However, this goal has not yet been achieved with either SPM technique. For the STM, the various methods that neglect the effect of a tip on the tunneling current and the obtained images have provided some insight into the imaging mechanism and can be trusted in standard situations. Yet even so, groundbreaking experiments require complex simulation for their interpretation. For the SFM, no simple model yet exists, and all unambiguous assignment of chemical identities to image features is based on direct simulation.

Theoretical methods used in scanning probe microscopy are in many ways similar to those used in other branches of surface science. The main difference between SPM modeling and, for example, studies of adsorption, adhesion, or cluster growth at surfaces, is that the SPM tip is a macroscopic object and is very rarely in force or thermal equilibrium with the surface. Image contrast represents the difference in the tip-surface interaction (with the SFM), or the tip-surface current (with the STM) at different surface sites, and all nonequivalent surface sites should be probed. Many events observed experimentally are unique and are not subject to statistical averaging. Until recently, theory has been mainly concerned with qualitative predictions. However, continuous refinement of experimental and theoretical methods makes quantitative comparison increasingly possible. This requires determination of parameters for comparison, formulation of criteria of agreement, and common calibration for theory and experiment.

II. EXPERIMENTAL SETUPS

The experimental setup of scanning probes for an STM or an SFM (Binnig and Rohrer, 1982; Binnig *et al.*,

1982a, 1982b, 1986; Güntherodt *et al.*, 1995; Bonnell, 2000; García and Pérez, 2002; Morita *et al.*, 2002; Giessibl, 2003) is determined mainly by the desired thermal and chemical environment. For traditional applications in surface science like the research of surface reconstructions, surface growth, surface dynamics, and surface chemistry, the instrument is mounted in a UHV chamber of less than 10^{-9} Torr. The UHV chamber and the analytical instruments themselves are mounted on rigid frames. This frame is externally damped by active (this is the latest trend) or passive damping elements, or mounted on rubber legs. Internally, vibrations of the UHV chamber and the analytical instruments are minimized by a combination of springs and eddy-current damping. The purpose of this elaborate scheme is to eliminate all vibrations from the environment, which would make the periodic motion of an SPM tip of less than 1 Å invisible due to background noise. The best instruments today, which are mostly homebuilt, are capable of a vertical resolution better than 1 pm, or one two-hundredth of an atomic diameter.

For biological applications, e.g., research on DNA and single cells, as well as for electrochemical purposes, the SPM is operating under liquid conditions (see, for example, Driscoll *et al.*, 1990; Ohnesorge and Binnig, 1993; Güntherodt *et al.*, 1995; Engel and Müller, 2000; Aoki *et al.*, 2001; James *et al.*, 2001; Jandt, 2001; Philippsen *et al.*, 2002). From an experimental point of view these conditions substantially limit the obtainable information and spatial resolution at a given surface structure. It is, however, an important step towards a realistic environment. In biological applications a liquid is the environment of all living organisms, and is therefore in a sense indispensable. True atomic resolution, however, has yet to be achieved under these conditions, hence we do not treat that aspect of scanning probe microscopy in this review.

The only experimental limitation for an STM is the requirement of conducting surfaces. Insulator interfaces for STM analysis are therefore grown to a few monolayers on a metal base [e.g., NaCl (Hebenstreit *et al.*, 2000), or MgO (Schintke *et al.*, 2001)]. Provided the tunneling current is still detectable, the insulator can be scanned in the same way as a conducting crystal interface. An SFM is generally free from these limitations and could be used to study any surface. However, for achieving atomic resolution it seems crucial that surfaces be smooth enough and that there be no strong, long-range, tip-surface forces, e.g., those due to charging. In recent years, the emphasis in both STM and SFM studies has gradually shifted from surface topography and surface reconstructions (Behm *et al.*, 1990; Chen, 1993) to surface chemistry (Fukui *et al.*, 1997b; Hla *et al.*, 2000; Hahn and Ho, 2001a; Sasahara *et al.*, 2001) and surface dynamics (Molinas-Mata *et al.*, 1998; Nishiguchi *et al.*, 1998; Bennewitz *et al.*, 2000; Lauhon and Ho, 2000; Schulz *et al.*, 2000; Hoffmann *et al.*, 2001).

Most STM experiments on semiconductors are done at room temperature, while high-resolution scans on metals rely, with but few exceptions (Biedermann, 1991), on a low-temperature environment of 4–16 K. Low-temperature scanning force microscopy is still a less than common practice. However, several home-built instruments have already demonstrated great improvement in resolution with respect to room-temperature instruments (Allers *et al.*, 1998; Lantz *et al.*, 2000; Uozumi *et al.*, 2002) and there are commercial low-temperature SFM's on the market. In this case the sample and/or the whole SPM system are cooled by liquid helium. Thermal motion in this temperature range is greatly reduced, and high-resolution images of close-packed atomic structures can then be obtained much more routinely.

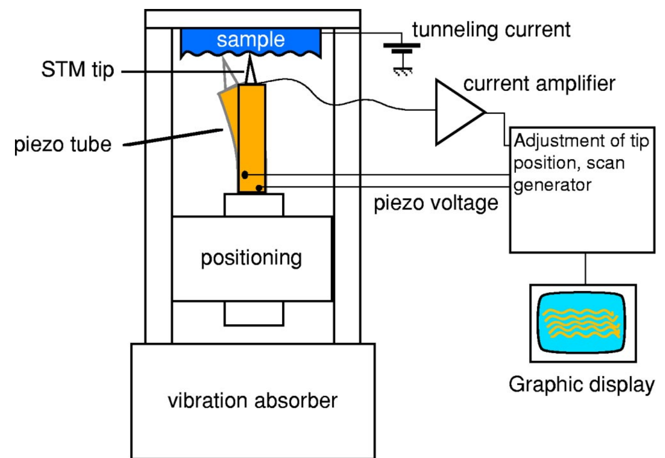

FIG. 1. (Color in online edition) Setup of a scanning tunneling microscope (STM). The tip is mounted on a piezotube, which is deformed by applied electric fields. This deformation translates into lateral and vertical manipulation of the tip. Via an electronic feedback loop, the position of the tip is adjusted according to the tunneling current (constant-current mode), and a two-dimensional current contour is recorded. This contour encodes all the information about the measurement. Courtesy of M. Schmid (Schmid, 1998).

Figure 1 shows the setup of an STM. In most cases the STM is built into a UHV chamber. Its main components are a sample holder, on which the surface under study is mounted; a piezotube, which holds the STM tip; an electronic feedback loop; and a computer to monitor and record the operation.

An SFM has quite similar components, as shown schematically in Fig. 2. They can be effectively categorized into three areas: (i) tip—macroscopic size and shape, conductivity, microscopic chemical structure, charge; (ii) surface—macroscopic thickness, conductivity, microscopic chemical structure, charge; and (iii) experimental setup—type of control of cantilever motion, electric circuit and bias between tip and sample or sample holder. Thus, to really simulate the experimental process, one needs not only to know the tip-surface interaction and model the cantilever oscillations, but also to take into account capacitance force, possible sample charging, and other macroscopic effects.

Measuring very small forces and force variations over the surface places more emphasis on the cantilever and the tip. Most observations are made by monitoring normal and torsional cantilever deflections induced by the

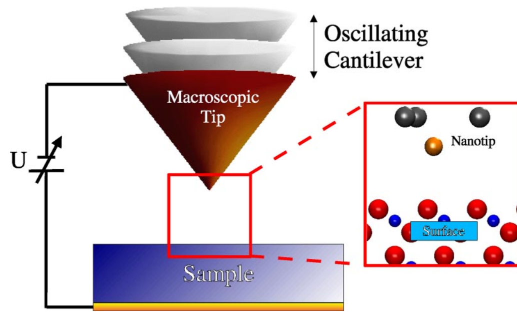

FIG. 2. (Color in online edition) Idealized schematic of the setup needed to model a noncontact scanning force microscope (NC-SFM) experiment on an insulating surface. The tip approaches the surface with frequency f_0 and U is a bias voltage between the conducting tip and the conductive sample support.

tip-surface interaction using various optical methods (Güntherodt *et al.*, 1995; Morita *et al.*, 2002). In early SFM designs the tip was pressed to a surface either by the van der Waals force or by the external elastic force of the cantilever, and imaging was performed in the so-called "contact mode." However, relatively recently it has been demonstrated that one can obtain much better sensitivity in measuring force variations on the atomic scale by employing dynamic force microscopy (García and Pérez, 2002; Morita *et al.*, 2002). In this case the cantilever is vibrated above the surface at a certain frequency, and the surface image is constructed by monitoring minute frequency changes due to the tip-surface interaction. Since in this case the tip is thought not to be in direct hard contact with the surface, this technique is often called noncontact scanning force microscopy (NC-SFM). It is currently the only reliable way of achieving true atomic resolution in an SFM, and in this review we shall focus primarily on the theoretical modeling underpinning this method. In later discussion, if a section of the review applies to SFM's in general then it will be specifically stated, otherwise it is written in the context of NC-SFM. Several reviews of contact-mode SFM's can be found (Giessibl, 1994; Güntherodt *et al.*, 1995; Shluger *et al.*, 1999; Bonnell, 2000).

Not every surface can be imaged with high resolution in an STM or SFM. To achieve atomic resolution, the surface in most cases needs extensive preparation. Sputtering (bombardment with ions, mostly Ar^+), and annealing (heating to the point where the surface defects are smoothed out) over weeks and even months in controlled cycles is not uncommon for studies of metal surfaces (Bischoff *et al.*, 2001). Surface preparation in itself is a sophisticated art and one of the keys to successful imaging (Chen, 1993; Himpsel *et al.*, 1998; Briggs and Fisher, 1999). In contrast to k-space methods like ion scattering or electron diffraction, a surface need not be ordered to be imaged by SPM. In fact, single impurities and step edges on a surface are often used by experimentalists to check the quality of their images. Such an impurity is only imaged as a single structure, assuming no distorting effects like double tips are present.

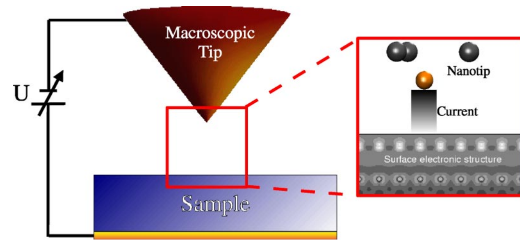

FIG. 3. (Color in online edition) Tunneling current in a scanning tunneling microscope. The surface of the tip is generally not smooth. A microtip of a few atoms will bear the bulk of the tunneling current; due to this spatial limitation of current flow, the electronic properties of a scanned surface can be extremely well resolved (resolution laterally better than 1 Å).

The tip is the crucial part in imaging for all SPM methods. STM tips are often made from a pure metal [tungsten, iridium (Chen, 1993)], a metal alloy [PtIr (Braun and Rieder, 2002)], or a metal base coated with 10–20 layers of a different material [e.g., Gd or Fe on polycrystalline tungsten (Wiesendanger and Bode, 2001)], and are often produced in the lab from metal wire. In some cases heavily doped Si tips are also used for STM imaging. Although similar tips could also be used for SFM measurements, this is very rare. This is due to the fact that the cantilever holding the tip plays a very important role in monitoring force changes in an SFM: (i) in many SFM realizations, cantilever deflections are measured by detecting light reflected from the back of the cantilever; and (ii) the cantilever spring constant, tip shape, and tip sharpness all play crucial roles in image formation. Standard cantilevers are therefore required. In most cases these are produced from silicon by microfabrication in very much the same way as semiconductor chips.

In some cases the tip is modified by controlled adsorption of molecules (Wertz *et al.*, 1997; Capella and Dietler, 1999; Hahn and Ho, 2001b; Nishino *et al.*, 2001). In STM's it has been shown that this affects the apparent height of molecules on a surface (Hahn and Ho, 2001b; Nishino *et al.*, 2001). The exact geometry of the tip is commonly unknown except for some outstanding STM measurements, where the tip structure was determined before and after a scan by field-ion microscopy (Cross *et al.*, 1998). To complicate matters further, the tip geometry is decisive for reproducible scanning tunneling spectroscopy measurements (Crommie *et al.*, 1993). Unfortunately, the tip most suitable for scanning tunneling spectroscopy is also shown to be unsuited for topographic measurements because it does not yield a high enough resolution (Feenstra *et al.*, 1987). Currently the most widely held opinion is that SPM tips consist of a base with rather low curvature and an atomic tip cluster with a single atom at the foremost position.

In an STM, all the current in the tunneling junction is transported via this "apex" atom. The area of conductance is consequently rather small and in the range of a few $Å^2$ (Chen, 1993; see Fig. 3). This is the origin of STM precision: the current is very sensitive to the electronic environment of a very small area of the surface.

Variations in the interaction of the last several atoms of the sharp tip apex with the surface atoms also determine the image contrast in SFM images. However, this sensitivity to atomic structure is also the origin of the features that make the interpretation of STM and SFM images so difficult because the actual geometry and chemistry of the tip apex, which influences the conductance in the vacuum barrier between surface and tip and tip-surface forces, cannot usually be determined. Even for simple metal surfaces like Cu(100) and NaCl(100), this leads to different experimental results for different scans (Clarke *et al.*, 1996; Bennewitz *et al.*, 2000).

As the determining factors in SPM experiments are not fully known, their relevance needs to be inferred from simulations. Simulations need to be done in a systematic manner, e.g., by studying the effect of adsorbates on the electronic structure of model tips (Hofer, Redinger, and Varga, 1999; Hofer, Redinger, and Podloucky, 2001), and by modeling the effect of these adsorbates on STM scans (Hofer and Redinger, 2000). Experimentally, the difficulty is circumvented, at least in careful measurements, by recording a series of scans and presenting decisive measures like the surface corrugation as a statistical average.

III. MAIN FACTORS DETERMINING IMAGE FORMATION

A. Controling interactions

The control parameter in an STM, the current in the tunneling junction, is always due to the same physical process. An electron in one lead of the junction has a nonvanishing probability of passing the potential barrier between the two sides, and tunneling into the other lead. However, this process is highly influenced by (i) the distance between the leads, (ii) the chemical composition of surface and tip, (iii) the electronic structure of both systems, (iv) the chemical interactions between surface and tip atoms, and (v) the electrostatic interactions of sample and tip. The main problem, from a theoretical point of view, is that the order of importance of all these effects depends generally on the distance, and therefore on the tunneling conditions.

In contrast to the operation of an STM, force controls SFM imaging, and it is not always due to just one physical process. Although it is impossible to discuss every possible interaction that might occur during an experiment, it is clear that for a technique to be reliable a consistent set of significant forces must exist. If the interactions varied wildly between experiments, then no useful comparisons or conclusions can be made. In this section the interactions significant to standard imaging are discussed, with specific reference to those forces important to the applications discussed later. Several other interactions, e.g., image forces, capacitance forces, and forces due to discrete charges, can be important for specific tip-surface setups and environments (Burnham *et al.*, 1993; Capella and Dietler, 1999; Morita *et al.*, 2002). These components of long-range electrostatic interaction between tip and surface can normally be minimized by applying a compensating bias during scanning (Bennewitz *et al.*, 1999a).

B. Tunneling current

The tunneling current is the control parameter in most STM experiments. It is set to a fixed value, and the position of the STM tip relative to the scanned surface is varied via the distortions of a piezocrystal, so that the current remains constant. The tip in this case describes a constant current contour. The extreme sensitivity of the tunneling current with respect to the tip-sample distance is the basis of vertical resolution in scanning tunneling microscopy. Qualitatively, it can be described in the following way.

The potential barrier in the vacuum range of the two subsystems determines the decay of surface wave functions in the same range. For a square potential barrier, the current decays exponentially with a constant exponent, which is proportional to $\sqrt{\phi}$, where ϕ is the work function of the two surfaces:

$$I(z) \propto e^{-k\sqrt{2\phi}z}. \tag{1}$$

Here k is a constant, and z is traditionally the distance between the two surfaces—to be precise, it is the distance from the nucleus of surface atoms to the nucleus of the tip apex.

In practice, this relation is only a good approximation. The work functions of sample and tip are in general not equal; the decay of electron states is not constant, but depends on their location in the surface Brillouin zone; and the density of states above the surface is typically varied.

It has been noted by experimentalists that the decay constant, or the apparent barrier height, remains remarkably stable even for low distances (Binning *et al.*, 1984; Payne and Inkson, 1985; Schuster *et al.*, 1992). This seems at odds with the expectation that the mutual penetration of surface and tip electron charge, as well as the existence of image charges, should lower the potential barrier in the low-distance regime. In fact, the opposite has been observed: the decay constant increases as the two surfaces approach each other (Binnig *et al.*, 1984). This behavior is due to interactions: as the distance between the atoms of surface and tip becomes small enough, chemical forces change the atomic positions. This shift of positions increases the tunneling current faster, during an approach, than expected from the electronic structure alone (Hofer, Fisher, Wolkow, and Grütter, 2001). It more than compensates for the saturation of current and thus the decrease of the apparent barrier height, as the two systems come into contact. Experiments reveal substantial oscillations of the tunneling current immediately before the two surfaces jump into contact (Gimzewski and Moeller, 1987). This is also an indication of the low stability of STM operation in this range.

The tip-sample distance can be experimentally estimated by a two-step procedure:

(i) the decay constant is determined from the current decay at a suitably large distance and consequently low currents; and
(ii) given a constant decay, the point where the conductivity equals $2e^2/h$, one conductance quantum is determined: this is seen as the point where the two surfaces are in contact.

The procedure is wrought with problems, because current decay at large distances is no indication of its behavior at small distances, and the movement of atoms due to chemical forces is neglected. Therefore experimentalists usually describe the distance in terms of their piezovoltage, or the voltage applied to the z coordinate of the STM positioning device. A difference in this voltage corresponds to a difference in the z coordinate of the STM tip; the scale is usually calibrated by comparisons with the (known) step height on sample surfaces. This is without doubt an objective measure, but it has the drawback that it describes the distance correctly only for a suitably large separation, and it fails in the range where high-resolution measurements are usually performed. For this reason, tip-surface separations have usually been overestimated by 1–2 Å. It took detailed simulations of coupled surface-tip systems to establish the actual distance range in high-resolution scans (Hofer and Redinger, 2000; Hofer, Redinger, *et al.*, 2000; Hofer, Fisher, Wolkow, and Grütter, 2001).

C. Bias voltage

Yet another parameter important in both STM and SFM experiments is the bias voltage. The relation between tunneling current and bias voltage is directly measured in scanning tunneling spectroscopy experiments. In these experiments, the current feedback loop is disengaged and the STM tip positioned at one point above the surface, usually described by its lateral position and the tunneling conditions, e.g., bias potential and tunneling current. A spectrum can be produced in two ways, either by (i) sweeping the bias voltage from a defined lower to a defined upper limit (the resulting $I-V$ is then recorded and numerically differentiated); or by (ii) extracting the differential directly from an experiment, where the bias voltage is oscillating with low frequency (in the range of kHz). The differential $I-V$ curve is then compared with simulations of the electronic surface structure. Tunneling spectra are very sensitive to surface states (Stroscio *et al.*, 1995; Bidedermann *et al.*, 1996; Hofer, Redinger, *et al.*, 2000) and states in the bulk band gap of semiconductors (Briggs *et al.*, 1992).

In general the change of bias voltage has two effects: (i) it shifts the Fermi level of one lead (sample or tip) relative to the other lead; and (ii) it compensates for this effect by the creation of a surface dipole. Both of these effects are understood in principle, even though no detailed simulations actually exist. The reason is that a simulation requires treating the coupled system of two leads and the interaction range in a nonequilibrium situation. Even though the theoretical framework for such a treatment in the STM context, the nonequilibrium Green's-function formalism of Keldysh, has been known for some 40 years (Keldysh, 1965), its numerical implementation only recently became possible (Taylor *et al.*, 2001). Provided the electronic density of states of the surface and tip structure are fairly smooth, then the current increases approximately linearly with the applied bias voltage. This is due to the energy difference between the Fermi level of sample and tip, which increases the number of electron states provided by one lead, increases the number of empty states provided by the other, and leads to the condition of resonant tunneling.

Application of voltage in the SFM setup is usually used to compensate for the macroscopic electrostatic forces described below. Again, although the effect is well known on the empirical level, calculations of real systems are still quite rare (see, for example, Jacobs and Stemmer, 1999; Gomez-Moñivas *et al.*, 2001). This is mainly due to the complexity of the tip shape and difficulty in describing surface charging and work-function anisotropies.

D. Electrostatic forces

The differences in Fermi level due to bias voltage, combined with the general differences between the Fermi level of a sample and the tip, introduce electrostatic effects into the interfaces. Although of the same origin, these effects have different consequences in STM and SFM measurements.

1. Effect of electrostatic forces in scanning tunneling microscopy

These effects have been analyzed by theoretical models of scanning tunneling microscopy in various instances: (i) the effect of the tip potential on semiconductor surfaces with an adsorbed organic molecule like acetylene (Ness and Fisher, 1997a, 1997b; Stokbro *et al.*, 1998); (ii) the effect of the tip potential on the electronic structure of metal surfaces (Hofer, Redinger, *et al.*, 2000); and (iii) the effect of electrostatic fields on the structure of sample and tip in a continuum model (Hansen *et al.*, 1998). In the first case the effect leads to a change of the tip-sample distance of about 0.1 at 6 Å. This effect depends on the distance. In actual measurements under normal experimental conditions [~2 V and 50 pA lead to a median distance of about 6 Å on Si(100) (Hofer, Fisher, Lopinski, and Wolkow, 2001)], the effect is present, but not substantial enough to alter the image in a decisive way. In cases (ii) and (iii), the applied field had to be very high. On an Fe(100) surface, for example, even though it is known to be very volatile, decisive changes of the electronic structure are limited to fields of more than 1 V/Å. Even in high-resolution scans, this value is beyond the limit of topographic imaging. It seems therefore safe to conclude that electrostatic fields of the STM tip do not substantially alter the electronic surface structure. In case (iii), the continuum model of tip and sample deformations due to fields, the minimum bias potential for observable changes on a metal surface

was about 2 V. Since STM images on metals are usually recorded with a bias potential of less than 0.1 V, even a difference of the Fermi levels of about 1 eV would not have a substantial effect. Hence we may conclude that field effects on metal or semiconductor surfaces can safely be neglected.

The effect of static fields due to nonconducting overlayers on metals or semiconductors has so far not been analyzed in STM theory. There is some indication from SFM theory that these fields via their forces may lead to a distortion of the system. However, since these measurements are still comparatively rare and in most cases satisfactorily explained by an analysis of the surface electronic structure (Hebenstreit *et al.*, 2000; Schintke *et al.*, 2001; Kliewer and Berndt, 2002), it seems implausible that they might lead to significant effects. To sum up, even though electrostatic effects are known to exist for acetylene on silicon and under the condition of very-high-bias voltages on metal surfaces, these effects are either confined to very low distances between tip and sample (Hofer, Fisher, Wolkow, and Grütter, 2001) or depend on very specific configurations.

2. Macroscopic electrostatic forces in scanning force microscopy

Macroscopic forces are those which generally do not depend on the atom directly under the tip and can be approximated by some sort of continuum or analytical expression. These forces are generally important in scanning force microscopy under any conditions, but obviously also play a role in NC-SFM. In this section we shall focus on those macroscopic forces most relevant to applications we discuss later. More detailed general information can be found in Burnham *et al.* (1993) and Capella and Dietler (1999).

The *van der Waals force* represents the electromagnetic interaction of fluctuating dipoles in the atoms of the tip and surface. On the atomic level, it is one of the weakest interactions, responsible, for example, for bonding in rare gas crystals. However, this force is nearly always attractive, and therefore small interactions between individual atoms of macroscopic tip and sample sum up into a resulting force on the order of several nanonewtons (nN). Although this force is small by macroscopic standards, it exceeds the chemical forces discussed below and in many cases dominates the tip-surface interaction. It is present regardless of the tip/surface setup used or the environmental conditions of the experiment [excepting SFM experiments in liquids (Israelachvili, 1991)].

The *image force* is the interaction due to the polarization of the conducting electrodes (i.e., of the conducting tip and the substrate) by the charged atoms of the sample. This is important for any tip-surface (or just surface) setup containing conducting materials, such as the interaction of a conducting tip with an insulating surface, or studying the properties of an insulating thin film on top of a metal substrate. As discussed by Kantorovich, Foster, *et al.* (2000) the image force can be strongly affected by the applied voltage (V) between tip and substrate. The image force is in principle a microscopic force [and is calculated as such (Kantorovich, Foster, *et al.*, 2000)], but it depends on the charge of the atoms in the surface rather than their chemical identity.

If there is a direct electrical connection between the tip and sample (in the case of an SFM, the tip and sample/substrate connected directly by a wire), then electrons are allowed to flow between two different conducting materials. This results in a *capacitance force* due to the potential difference between the tip and surface. The potential difference is due to two components: (i) the contact potential U between the tip and surface (the electrons must spend energy to travel from the material with the smaller work function to the material with the higher one); and (ii) the applied voltage V across the system. Kelvin probe microscopy allows one to measure the local contact potential difference across the surface by measuring the applied bias voltage required to compensate the capacitance force due to contact potential (Jacobs and Stemmer, 1999). The capacitance force can be easily calculated analytically as a function of the tip/sample geometry and U (Hudlet *et al.*, 1995; Jean *et al.*, 1999). Note that, although in principle electrons can transfer between the end of tip and the surface, at the scanning ranges used in NC-SFM this effect is negligible.

The discussion of the capacitance force above makes an assumption about surfaces that is not always valid. By calculating the capacitance force as a function of z alone, it is assumed that the work function is uniform across the surface. On real surfaces, inequivalencies in the work function across the surface can arise due to surface preparation, adsorbates, crystallographic orientation, and variations in local geometry (Burnham *et al.*, 1992, 1993). Real surfaces of any material are not perfectly smooth, as is suggested by the very-small-scale NC-SFM images usually seen. This is especially relevant for the electrostatic minimization procedure used in experiments (see Sec. V.C.1), which minimizes at a single point on the surface before scanning. Variations in the work function over the region scanned could render the minimization process invalid, or at least approximate. Other studies (Burnham *et al.*, 1993) have already suggested that work-function anisotropies are the most likely source of the long-range interactions observed in force microscopy of graphite with diamond tips. The contribution of work-function anisotropies to the tip-surface interaction cannot be calculated explicitly, but it can be represented by increased surface charge density or increased/decreased applied bias when calculating the image force contribution (Burnham *et al.*, 1993).

Many processes in NC-SFM imaging can introduce charge into the tip and surface. Surface preparation by cleavage is known to induce very large charges on insulating surfaces (Harris and Fiasson, 1985; Wintle, 1997; Luna *et al.*, 1998; Engelhardt *et al.*, 2000), although these can be reduced by annealing. These charges are usually localized on edges of cleavage tips and around dislocations. Tip and surface sputtering can also cause charging, as can ion exchange between the tip and surface during

scanning (tribocharging). On the microscopic scale, these charge defects can appear as strange artifacts in images or as unexpected interactions close to the surface. On the macroscopic scale, *tip and surface charging* can dominate the interactions, and in some cases even prevent stable imaging.

E. Chemical forces

Although the chemical forces are not the strongest between tip and surface, they are the most important interaction both in scanning tunneling microscopy and in NC-SFM. In scanning force microscopy they can really distinguish atomic identities and are therefore responsible for atomic resolution in images (see further discussion in Sec. IV.C). They also define the atomic structure of the tip and surface and are responsible for atomic displacements when the tip is close to the surface. Although other forces, such as the van der Waals and image forces, result from atomic interactions, in most cases they can be accurately approximated by a macroscopic interaction.

In the context of scanning tunneling microscopy, these issues are especially important and encourage the study of the formation of chemical bonds between tip and surface, as well as the range at which a chemical bond can be considered to exist. If a chemical bond forms, then the energetic level of the bond may end up below the energy level of the conductance band of the leads. In this case no tunneling current will be observed, even though the bond formation results in attractive forces between atoms of the surface and atoms of the STM tip. However, the relaxation of atoms due to these forces will reduce the distance between the two surfaces and thus, via a secondary effect, enhance the tunneling current. If the energy level of the combined electrons lies within the conductance band of the leads, then the electrons oscillating between the two atomic centers will freely propagate through the drain side of the junction: no chemical bond will form. From this qualitative model it is clear that chemical forces will only affect the observed tunneling currents from a certain onset. The main question, then, is where this onset actually lies in terms of tip-sample separation. This question has been discussed without conclusive results for more than 20 years (Pethica and Sutton, 1988; Sacks and Noguera, 1988; Cho and Joannopoulos, 1993; Clarke *et al.*, 1996; Ventra and Pantelides, 1999; Sacks, 2000).

Due to the advent of first-principles methods and powerful computers it could finally be resolved by a calculation of the combined tip-sample system (Hofer, Fisher, Wolkow, and Grütter, 2001). The point of onset for chemical bonding was found to be at a distance of 4.6–4.7 Å. As the tip approaches the surface, chemical forces rapidly become large enough to destroy the stability of a tip-sample system in an STM due to ions jumping to/from the tip from/to the surface. The point of destruction is about 4.0–4.1 Å. From the onset of chemical forces to the limit of mechanical stability, the two main effects are (i) an increase of the tunneling current beyond exponential growth; and (ii) an increase of surface corrugation by a factor of 2–3. Both effects are observed in experiments (Gimzewski and Moeller, 1987; Hallmark *et al.*, 1987). They show, unambiguously, that a high-resolution STM operates within the range of chemical forces and that the main effect, omitted in any straightforward perturbation model, is the relaxation of surface atoms due to chemical interactions. It is perhaps not surprising that theoretical modeling predicts the onset of contrast formation in NC-SFM imaging of semiconductors and insulators at approximately the same distance range (Livshits *et al.*, 1999; Lantz *et al.*, 2000; Barth *et al.*, 2001). Quantitative comparison between theory and experiment, discussed in Sec. V.C.1, demonstrates that the distance range of 3.5–4.5 Å is where the best contrast can be achieved in stable NC-SFM imaging of insulator surfaces.

F. Magnetic forces

Magnetic forces are really only important when both the tip and sample demonstrate magnetic behavior, e.g., both are ferromagnets. This situation is not encountered in normal NC-SFM studies, but modifications of the standard setup have been performed so that the magnetic properties of materials can be probed on the nanoscale. These magnetic force microscopes (Martin *et al.*, 1987) have proved successful in imaging magnetic domains at very small scales and offer a great deal of potential for nanoscale magnetic recording.

The force sensitivity of the NC-SFM technique on the atomic scale has encouraged studies of the atomic-scale magnetic properties of surfaces. In particular, interest in the possibility of directly measuring differences of the exchange interaction with different surface sites has been motivated by the early suggestions from spin-polarized scanning tunneling microscopy (Wiesendanger *et al.*, 1990), that the magnetic force between tip and sample at small distances (2–5 Å) could be measured. The recent introduction of low-temperature ($T<15$ K) NC-SFM's (Allers *et al.*, 1998) and the associated reduction in thermal noise has made this possibility even more feasible, and now several experimental NC-SFM groups are actively pursuing the measurement of atomic-scale spin structure with magnetized metallic tips. In spite of several attempts (see, for example, Hosoi *et al.*, 2000; Allers *et al.*, 2001), experimental measurement of exchange forces has proven extremely challenging and no conclusive results have been obtained so far. A theoretical analysis of the possibility of measuring exchange forces with an NC-SFM has been presented by Nakamura *et al.* (1999) and Foster and Shluger (2001) and is discussed later.

By contrast, magnetic surfaces are one of the main areas of STM research on metals. Reasons for this burgeoning interest include their technical importance, e.g., for storage, their potential for nanotechnology, e.g., magnetoelectronics or "spintronics," and the wealth of intricate effects that may be observed. The full potential of an STM to record and differentiate electrons of dif-

ferent spin orientation has only recently been exploited (Heinze *et al.*, 2000; Piezsch *et al.*, 2001; Wiesendanger and Bode, 2001). In these experiments the tip was coated with magnetic material. The main experimental applications today are in tunneling spectroscopy (Wiesendanger and Bode, 2001) and topography with magnetic contrast (Heinze *et al.*, 2000).

Theoretically, the influence of magnetism on the tunneling current comes from two origins: (i) the magnetic moment and electronic structure of different spins; and (ii) the orientation of the magnetic axes. Again, the electronic structure and the magnetic moment can be determined from density-functional theory (DFT) calculations. The orientation of the magnetic axis is in principle obtainable from DFT methods including spin-orbit coupling. In practice it is often constrained by experimental conditions for one or the other subsystem. The tunneling current then depends on the angle ϕ between the magnetization vector of the sample and the magnetization vector of the tip (Hofer and Fisher, 2003).

G. Summary

An SPM is a local atomic probe, which utilizes the fact that charge flow and forces between atoms are very sensitive to the physical environment. This makes it possible, with such an instrument, to probe the environment directly by carefully recording the local changes. Success depends not least on the ability to measure and to react to minute changes in the control parameters within very short intervals (less than one millisecond). The ability to control the tip-sample distance on the picometer scale via piezoelectric elements was really the technological breakthrough that moved scanning probe microscopy from the mesoscale to the nanoscale.

IV. MODEL DEVELOPMENT

Modeling the SPM involves several stages, which differ in detail for STM's and SFM's. The task can be broken down into five discrete steps:

(i) establishing a realistic model of the surface from experiment and theory;
(ii) establishing a realistic model of an SPM tip using properties known experimentally and inferred from theory;
(iii) explicitly modeling the interactions between the tip and surface;
(iv) calculating the current (STM) or the oscillations of the cantilever (NC-SFM) under the influence of these interactions, and constructing a theoretical image; and
(v) comparing the theoretical model with experimental images.

The main differences between scanning tunneling microscopy and scanning force microscopy concern steps (ii) and (iii). For a realistic model of an SFM tip, the macroscopic form of the tip plays an essential role, because this macroscopic form has a decisive influence on long-range interactions. For an STM tip, this is generally irrelevant, since the main effects observed in experimental conditions are due to the microscopic structure of the tip and the electronic states, as well as the atomic positions at the apex of such a tip. While the focus in SFM simulations is on a precise rendering of the macroscopic (long-range forces) as well as the microscopic (chemical and short-range forces) tip structure, the focus in STM simulations is only on the microscopic structure.

The difference between scanning tunneling microscopy and scanning force microscopy in step (iii) is due to the measured variable itself. In STM images, the current is *altered* by interactions, compared to the noninteracting cases; in NC-SFM the change of frequency is *determined* by the very same forces. It is therefore generally sufficient in STM simulations to estimate the influence of interactions in a given experimental situation, and this influence can be determined by model calculations of specific systems. The interactions themselves, in this case, need not be treated in every situation (see also Sec. III.A).

The additional complication in STM simulations is the requirement that the electronic states on the tip surface be precisely simulated, because these states determine the obtainable contrast and thus the simulated STM image. For this reason STM tip simulations generally have to rely on first-principles methods solely, although we shall see that first-principles methods are also used as a fundamental reference for simulations of scanning force microscopy.

The level of complexity needed to calculate the atomistic interactions in an NC-SFM depends on the properties of the system being studied. First, it is important to establish the criteria for choosing a method. For the interactions of ionic systems, where the electron charge density is localized on the atomic cores and there is no significant charge transfer, it is sufficient to use atomistic simulation methods (Catlow and Mackrodt, 1982) based on classical interatomic potential treatment and the shell model (Dick and Overhauser, 1958) for ionic polarization. Atomistic simulation techniques are computationally very effective, and systems of several hundred atoms can be calculated on a PC. However, the interactions in atomistic simulation calculations must be parametrized for each pair of atoms, and this leads to problems in overall accuracy—although very high accuracy can be achieved for specific physical properties. It should be noted that the parameters for the atomistic simulation interactions are always checked by comparison to experiment or quantum-mechanical calculations. Examples of this can be seen in Secs. V.C.1 and V.C.2.

For semiconducting and metallic systems, it is important to represent the delocalized electron density correctly and to consider covalent bonds between tip and surface. Therefore a more rigorous quantum-mechanical treatment, such as *ab initio* Hartree-Fock theory or density-functional theory (DFT) (Ohno *et al.*, 1999)

should be used throughout (see, for example, Pérez *et al.*, 1997; Shluger *et al.*, 1997; Ke *et al.*, 1999; Tóbik *et al.*, 1999).

A. The surface

The first stage of the modeling process is establishing a good representation of the surface being studied. The wealth of experimental methods of surface preparation is to a certain extent responsible for the wealth of surface effects that are studied by atomic probe instruments. In the simplest cases, and if a clear consensus on the surface structure has been established previously, then this can be used directly, as in the examples in Secs. V.A and V.C.2. If there is no clear consensus, then an accurate structure in some cases can be found from a combination of other experimental techniques and theoretical methods. The most difficult situation occurs when establishing the unknown surface structure is the sole purpose of SPM experiments. Notwithstanding the famous example of the Si(111) surface, in which scanning probe microscopy revealed the (7×7) reconstruction (Binnig *et al.*, 1983), this is not a trivial task. In view of the ambiguities of the experimental results, alternative surface models should be used and checked before an agreement is sought from a broad set of experimental data.

Preliminary models of the surface topography, for example, can be determined by atomic-probe methods, ion scattering, electron diffraction, or Auger spectroscopy. The chemical bonds of adsorbates can be estimated from infrared spectroscopy. The surface electronic structure is accessible by photoelectron emission techniques. Experimental techniques in surface science have developed in parallel with advances in surface preparation. Today, surfaces can nearly be tailored to individual needs by physical and chemical methods (Himpsel *et al.*, 1998; Wolkow, 1999; Shen and Kirschner, 2002).

When the surface structure is known, its electronic structure has to be computed with sophisticated methods, and existing codes more and more rely on first-principles density-functional theory (Wimmer *et al.*, 1985; Kresse and Hafner, 1993; Kresse and Furthmüller, 1996), or, in case of tight-binding models (Turchi *et al.*, 1998), they obtain their parameters from a fit to DFT data (Cerda and Soria, 2000). The fit is not without ambiguities, since it is unknown whether the density of states used for the fit is really unique.

B. The tip

It is well known that contact between the bottom of the tip and the sample surface will not be between two smooth, regular surfaces. In particular, the bottom of the tip may contain many asperities, and one of these asperities will serve as the probe. To accurately model an SPM tip, one should know its shape and a Hamaker constant of its van der Waals interaction with the surface (SFM), as well as the chemical nature and crystallographic orientation of its apex (SFM, STM). Unfortunately, there is very little information on the properties of SPM tips; effectively only the most basic qualities are known.

In STM experiments the most common tip is made from a tungsten polycrystalline wire; other tip materials are commonly transition metals (platinum, iridium, alloys; Chen, 1993). These tips are electrochemically etched in NaOH. The obtained curvature of the tip depends on the duration of etching; it ranges from 20 to 100 nm (Chen, 1993). This tip is further altered *in situ* by frequent voltage pulses of 10–20 V. It is generally agreed today that only a very sharp tip with a single atom at its pinnacle is suitable for obtaining atomic resolution on close-packed surfaces. But such a tip is highly unstable. Therefore the fabrication and characterization of defined tips, e.g., by field ion microscopy, has not been achieved, nor can it be expected for the near future. Other experimental preparations include tip sputtering with Ar^+ ions, or tip coating with additional layers (Wiesendanger and Bode, 2001). Only a limited number of experimental images obtained with these tips are actually recorded and made public. Among the nonrecorded images are usually the ones obtained with multiple tips, or tips that render images of poor quality. In case of scanning tunneling spectroscopy experiments, the reproducibility of spectral data requires fabrication of a very blunt tip (Feenstra *et al.*, 1987), which is unsuitable for high-resolution scans of metal surfaces.

SFM tips are microfabricated from silicon in much the same way as computer chips and, as produced, have a pyramidal shape. However, this only gives their structure on the micrometer scale, and there is no direct method for imaging the very end of the tip—the "nanotip." Therefore additional information is needed to reconstruct tip structures. In particular, it is known that the tips are oxidized due to exposure to the atmosphere and, although the oxide layer can be removed by argon ion sputtering, they can be contaminated by the residual water always present in a UHV chamber. Some recent atomically resolved images use untreated tips covered by an oxide layer (Fukui *et al.*, 1997a) and specially prepared silicon tips cut from silicon wafers (Giessibl *et al.*, 2000). Metallic (Erlandsson *et al.*, 1996) and silicon tips covered by metal (Hosoi *et al.*, 2000; Allers *et al.*, 2001) have also been used in NC-SFM experiments.

In many SPM experiments atomically resolved images are obtained after tips were in contact with the surface and are most likely covered by the surface material. Tip crashes often happen spontaneously due to strong tip-surface interaction, the presence of debris on the surface, and other artifacts. However, in many cases "gentle" contact is arranged intentionally, as it has been noted that this increases the chances of obtaining good atomic resolution. Tip contamination by the surface material has been explored by Livshits and Shluger (1997a, 1997b) using classical molecular dynamics. An MgO cube tip was indented into the LiF surface and then retracted back from the surface. In another set of calculations the surface scanning was simulated after indentation. In both cases stable clusters of the surface material were formed on the tip.

Still, this information gives only a very preliminary idea about the tip's possible chemical composition, and nothing about the geometric structure, stoichiometry, and charge of a nanotip. One solution to this difficult problem is to use idealized nanotips. This method has been used in recent *ab initio* studies of scanning force microscopy on semiconductor surfaces (Pérez *et al.*, 1998; Ke *et al.*, 1999) and in atomistic simulations on ionic systems (Shluger and Rohl, 1996; Shluger *et al.*, 1999). It is a good basis for beginning the tip-modeling process. Another approach would be to try and find the most realistic tip model for a particular set of experiments. This approach has been applied in some SPM simulations (Foster, Hofer, and Shluger, 2001). Below we briefly outline the main features of both these approaches.

1. Idealized tips

The approaches using idealized tips are based on two main considerations. First, they assume that the tip structure is too complex to be treated explicitly and is likely to change during experiments. Therefore one should try and reproduce only general qualitative features which can be responsible for image contrast in spite of all the complex issues discussed above. Second, to keep calculations practical, nanotips cannot be large and should include 20–30 atoms.

The prevailing perception of STM modeling has been, since the work of Tersoff and Hamann (Tersoff and Hamann, 1985a, 1985b), that a single tip orbital is responsible for the image contrast. In simulations, this orbital was thought to be an electron state of the tip metal. The question of whether the symmetry of this orbital is s-like (radial symmetry), or rather d-like (elongation in one or two directions; Chen, 1990a, 1990b) has led to heated discussions. It was only resolved by detailed simulations of the tip apex, which showed that the tip orbitals are d-like (electron states of transition-metal atoms), even though the convolution of all states near the Fermi level frequently shows radial symmetry (Hofer, Redinger, and Podloucky, 2001).

In STM simulations based on single-tip orbitals, this is due to the existence of free parameters in the evaluation (the decay κ and radius R in both the Tersoff-Hamann model and Chen's modification), which are fitted to experimental data. This procedure removes the possibility of comparing simulations to the experimental tunneling currents. In fact, it reduces the accuracy of the comparison quite substantially, because the only measure left for comparison is the protrusion of single atoms (this is called the *corrugation* or *corrugation height* of surface atoms). The corrugation height is in most cases not unique; whether a surface is corrugated (atoms stick out) or anticorrugated (atoms are seen as holes) cannot be determined from experimental images. Moreover, the simulated corrugations are usually fitted to the experimental data, which leads to an estimate for the tip-sample separation. Almost without exception, these estimates are too low when compared to detailed simulations (Hofer, Fisher, Wolkow, and Grütter, 2001).

In SFM simulations, the most common perception in modeling on Si and other semiconductor surfaces has been that the main component of the tip-surface interaction responsible for image contrast on these surfaces is the interaction of a dangling Si bond at the end of the tip with the surface atoms. This dangling bond can be well described using relatively small 4- or 10-atom Si clusters saturated by H atoms (Pérez *et al.*, 1998). Another approach has been used to model tips for simulating SFM images of ionic surfaces. Here it was assumed from the start that the electrostatic forces between the tip and surface would be most important, and mainly ionic tips were considered (Shluger and Rohl, 1996; Shluger *et al.*, 1999).

2. Modeling of real tips

The tip models described above have been successful in developing a qualitative understanding of the origins of image contrast in scanning probe microscopy on metals, semiconductors, and insulators. However, they fail in most cases to reproduce the quantitative results of experiments. The solution to these problems is to compare images to simulations with a number of different tip models.

The most suitable STM tip model for work on semiconductor surfaces is a tungsten pyramid, whereas on metal surfaces a tungsten film with either a tungsten apex atom or an atom of the sample surface works best. On metal alloy surfaces, for example, it is likely that the apex of the STM tip is composed either of atoms of the tip material (e.g., tungsten) or of single atoms of the scanned surface, because it frequently comes in very close contact with the surface. Since most metal surfaces of technical importance are transition metals, it suffices for model tips with transition-metal adsorbates to be able to study a large proportion of all STM experiments on metals. In principle, it would also be necessary to vary the surface orientation of the STM tip, but in practice it turns out that the chemical composition is the dominant influence for electronic structure.

The effect of single STM tips can be studied qualitatively by analyzing their surface electronic structure. If it is composed to a high degree of single-electron states (Kohn-Sham states), which protrude far into the vacuum within a small area, this causes the electron tunneling from the sample to the tip to be far more localized: the tip, in this case, resolves the surface electronic structure very well. The opposite is true if the wave functions are very delocalized: then the conductance for one state will cover a large area and sample the surface electronic structure in a statistical manner. In this case, detailed information about the surface is lost.

The curvature of the wave functions at the Fermi level, and thus the obtained corrugation on a surface, depend on the chemical (and magnetic) nature of the apex atom. To illustrate this point we show the local density of states of various magnetic and nonmagnetic

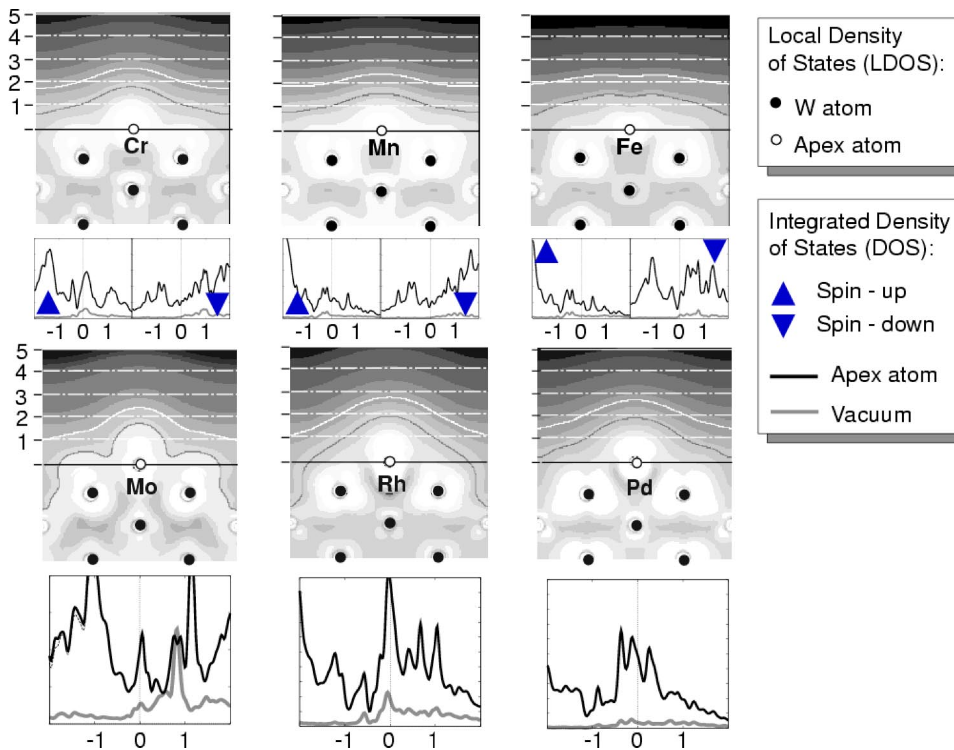

FIG. 4. (Color in online edition) Local density of states and integrated density of states of selected magnetic and nonmagnetic scanning tunneling microscope (STM) tip models. The tip is mimicked by a W(100) surface with single $3d$ and $4d$ impurities. Reprinted with permission (Hofer, Redinger, and Podloucky, 2001).

transition-metal atoms adsorbed on a W(100) surface (see Fig. 4). The two panels show the electronic structure of magnetic (Cr, Mn, Fe, Co) and nonmagnetic adsorbates (Mo, Rh, Pd, Ag) on tungsten films. The contour plots depict the local density of states in a plane perpendicular to the tip surface of all states near the Fermi level ($E_F \pm 0.1$ eV). Two single contours are emphasized, and the distance from the STM tip surface is marked. The graphs in the lower part of the figure show the density of states integrated over the volume of the apex atom (black) or the vacuum region (gray). We have differentiated between the spin-up and spin-down states of magnetic atoms.

These and similar STM tip models have been used in simulations of STM experiments on metal alloys. From a comparison of simulations and experiments on different metal surfaces in a statistical manner, it is evident that the best agreement is achieved if the apex atom of the STM tip is an atom of the sample surface (Hofer and Redinger, 2000). This, in turn, tallies nicely with the experimental practice of increasing surface contrast by controlled crashes of the tip into the surface.

To obtain realistic tip models, DFT calculations of the electronic structure of fully relaxed tungsten films with one or two surface layers of either tungsten atoms or adsorbates have proven to be the most suitable choice (Hofer *et al.*, 1999; Hofer, Redinger, and Podloucky, 2001). The adsorbates so far considered include most transition metals. In single cases where the STM tip was covered by 10–20 layers of Fe, the tip has been modeled by a Fe(100) film covered by one atom, or a layer plus one atom, of sample surface atoms (Hofer and Fisher, 2003).

Different possible nanotip models for the SFM have been compared to try and determine which most closely matched experimental behavior, for example, on NaCl surfaces (Bennewitz *et al.*, 2000). First, it was found that if the bottom of the tip was flat, i.e., no nanotip, then the interaction with the surface was averaged over several tip ions, and no contrast was produced. When a nanotip was included, it had to extend significantly beyond the main part of the tip to reproduce the interaction observed in experiment. Specifically a nanotip of only a few atoms would not atomically resolve lower terraces of stepped surfaces, which contradicts experiments on the NaCl surface [see Fig. 25(a)].

Silicon tips are likely to be contaminated by residual oxide, adsorbed hydrogen, and water (Zaibi *et al.*, 1997), or even the surface material. To investigate the electrostatic properties of clean and contaminated silicon tips, the electrostatic potentials of Si_{10} clusters with adsorbed contaminant species were calculated using DFT and the VASP code by Sushko *et al.* (1999). The results clearly showed that the adsorbed hydrogen had no effect on the potential from the uncontaminated silicon cluster. However, the adsorbed oxygen and hydroxyl group causes a significant change in the potential gradient from the Si adatom. Both potentials decayed over a much longer range than the uncontaminated cluster, and their stronger gradients suggested they would interact much more strongly with the surface.

Interestingly, the potential gradient from the MgO cube corner was very similar to that of the oxygen-contaminated silicon cluster, a strong negative potential. The cube could also be orientated with an Mg ion down, providing a strong positive potential. For many SFM experiments on insulators, the purely ionic MgO tip model proved to provide excellent qualitative and quantitative agreement for the reproducible contrast patterns observed. However, recent increases in experimental sensi-

tivity have reduced the possibility of large-scale tip contamination by ionic material, and it has also become important to use conducting tip models when studying insulating surfaces. Now simulations calculate the relative influence of pure Coulomb interactions, polarization, and charge transfer by using different tips on the same surface. This builds a more complete picture of the tip-surface interaction and allows a much wider spectrum of SFM experiments to be understood. An example of this approach to simulations can be seen in the study of CaF_2 in Sec. V.C.1.

3. Combining microscopic and macroscopic tip models

So far we have considered the nanotip models. However, the tip-surface interaction is determined by the properties of the whole tip. The fact that the whole tip model is separated into microscopic and macroscopic components means that the properties of a silicon tip which are missing from an MgO microscopic model can be introduced in the macroscopic model of the tip. This can be done via the Hamaker constant and also by including the image and capacitance forces pertaining to conductive tips. Whether these forces are important and should be included at all is impossible to know *a priori*. Nevertheless, some information regarding the possible tip shape, conductivity, and charging can be found from analyzing the experimental dependence of the NC-SFM cantilever frequency change versus the tip-surface separation measured before and just after imaging (Foster, Kantorovich, and Shluger, 2000; Guggisberg *et al.*, 2000). Success in extracting the main components of the tip-surface interaction on different substrates (Sounilhac *et al.*, 1999; Guggisberg *et al.*, 2000; Loppacher *et al.*, 2000) suggests two main approaches to tip characterization. Both of them exploit different behavior of van der Waals and electrostatic forces as a function of tip-surface separation. One approach is based on using a well-characterized surface (e.g., metallic) as a reference before or after scanning the surface of interest. A more direct method is to analyze frequency change versus tip-surface separation curves measured on the same surface just after imaging. An example of this latter approach will be given in Sec. V.C.1.

C. Tip-surface interaction

The force can be split into two general components: (i) the *microscopic chemical force* between atoms in the tip and surface, and (ii) the *macroscopic force* between the tip and surface, which always includes the van der Waals and various other (electrostatic) interactions depending on the specific tip/surface combination studied. Extensive SPM modeling suggests that only the short-range chemical forces are responsible for atomic resolution (Livshits and Shluger, 1997b; Foster, Barth, *et al.*, 2001; Hofer, Fisher, Wolkow, and Grütter, 2001), whereas the macroscopic forces can be treated as a *background attractive force*. This background force is important in reproducing experimentally observed frequency changes in an SFM, but is independent of the identity of the atom under the tip and does not play a role in atomic displacements. Therefore it is generally irrelevant for STM experiments.

In terms of STM modeling, this means that only microscopic forces have to be considered in a specific situation (high-resolution scans); in general (low-resolution, semiconductors) even these forces can be neglected and the theoretical model can be reduced to perturbation theory. In SFM simulations the chemical and macroscopic components of the interaction can be calculated separately and just combined for the final stages of modeling to give the total force.

Certainly not all known types of interactions can be included in the theoretical modeling on an equal footing. Thus a strategy focusing on the most important determinants of the actual characteristics measured must be implemented. In discussing the forces relevant to NC-SFM, we shall focus on experiments performed in UHV. Certain forces, for example, capillary forces, which are relevant for the SFM in air, will not be discussed. Two excellent reviews of the forces that are relevant to the SFM in general are those of Burnham *et al.* (1993) and Capella and Dietler (1999).

1. van der Waals forces

The van der Waals interaction is nonadditive, as atoms polarize each other. Nevertheless, an additive approximation is used in many practical applications, including atomistic simulation calculations of scanning force microscopy. In particular, the van der Waals interaction between the atoms at the end of the tip and in the surface is taken into account explicitly by summing the interaction of all pairs of atoms. However, the full tip contains billions of atoms, and it is impossible to sum all the interactions; therefore an approximation must be made based on the material and structure of the tip. The van der Waals interaction potential is

$$V(r) = -\frac{C_6}{r^6}, \tag{2}$$

where C_6 is the interaction constant as defined by London (1937) and is specific to the identity of the interacting atoms. Hamaker (1937) performed the integration of the interaction potential to calculate the total interaction between two macroscopic bodies using the following approximations:

- additivity—the total interaction can be obtained by the pairwise summation of the individual contributions.
- continuous medium—the summation can be replaced by an integration over the volumes of the interacting bodies assuming that each atom occupies a volume dV with a number density ρ.
- uniform material properties—ρ and C_6 are uniform over the volume of the bodies.

This then allows the total force between two arbitrarily shaped bodies to be given by

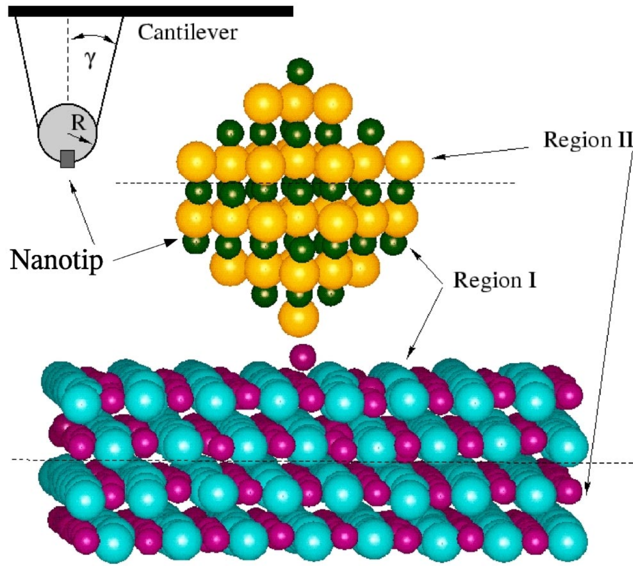

FIG. 5. (Color in online edition) Schematic of integration of macroscopic and microscopic tips. The nanotip has a conical angle γ and radius R. The nanotip and the upper surface layers are divided into two regions, I and II. The region-I ions are relaxed explicitly, while the region-II ions are kept fixed to reproduce the potential of the bulk lattice and the remaining tip ions on the relaxed atoms.

$$F_{vdw}=\rho_1\rho_2\int_{v_2}\int_{v_1} f(r)dV_1dV_2, \quad (3)$$

where ρ_1 and ρ_2 are the number densities, $f(r)$ is equal to $-\nabla V(r)$, and V_1 and V_2 are the volumes of bodies 1 and 2, respectively. The Hamaker constant for the interaction is then

$$H=\pi^2 C_6\rho_1\rho_2. \quad (4)$$

Useful expressions for the van der Waals interaction between bodies of different shape are discussed by Israelachvili (1991). Argento and French (1996) derived expressions for the total van der Waals force between a conical tip of angle γ with a sphere of radius R at the end (see Fig. 5) and a plane:

$$F_{\mathrm{vdw}}=\frac{HR^2(1-\sin\gamma)(R\sin\gamma-z_0\sin\gamma-R-z_0)}{6z_0^2(R+z_0-R\sin\gamma)^2} \quad (5)$$

$$-\frac{H\tan\gamma[z_0\sin\gamma+R\sin\gamma+R\cos(2\gamma)]}{6\cos\gamma(z_0+R-R\sin\gamma)^2}, \quad (6)$$

where z_0 is the tip-surface separation. The expressions for pyramidal and more complex tips are given by Suresh and Walz (1996), Touhari *et al.* (1998), and Zanette *et al.* (2000). Calculation of the van der Waals contribution to the total tip-surface force requires only knowledge of γ, R, and H. γ and R depend only on the tip shape, and this can be estimated from experimental studies of NC-SFM tip properties (see Sec. V.C.1). The Hamaker constant H depends on the geometry and materials of the tip and surface. However, if the NC-SFM system is well represented by a conical or pyramidal tip and a planar surface, then H effectively depends only on the material of the tip and surface. The experimentally determined values for Hamaker constants for different pairs of materials are given by French *et al.* (1995) and Argento and French (1996).

2. Calculating microscopic forces

The STM simulations presented here rely on a two-step procedure. First, the electronic structure of the relaxed system is calculated. The coupled sample-tip system is represented by a 3D repeat unit comprising the surface [e.g., a five-layer Au(111) film], the tip [a five-layer Au(111) film with a tungsten tetrahedron mounted on the reverse], and a variable vacuum range between surface and tip. For a given distance, induced from the outset by a variation of the vertical dimension of the repeat unit, the electronic structure is calculated via a pseudopotential DFT method [the VASP code (Kresse and Hafner, 1993; Kresse and Furthmüller, 1996)]. This code uses a residual minimization technique for faster convergence to the ground-state solution. From the electronic ground-state solution the Hellman-Feynman forces on ions are calculated analytically. A Newton algorithm is used to find the most likely ionic positions, and the system is again converged to its electronic ground state in the new configuration. Such a self-consistency cycle, involving the ionic positions and the electronic ground state, is repeated until the forces on single ions are less than a preset threshold value, usually around 0.01 eV/Å. Separating the system into two components, the surface and the tip, and calculating the electronic ground state of the frozen component, one can directly determine the forces on surface and tip ions (since the attractive force due to the presence of the other half of the system is now missing, the calculation yields a force on the surface ions of exactly the same magnitude, but opposite direction). The setup of the calculation is shown in Fig. 6.

Nearly all the SFM simulations presented in this review were performed using atomistic simulation techniques as implemented in the MARVIN computer code (Shluger *et al.*, 1994; Gay and Rohl, 1995; Shluger and Ruhl, 1996). MARVIN treats surfaces in a 2D periodic model by repeating a unit cell of atoms in two dimensions by specified lattice vectors. For tip-surface calculations, this unit cell includes the whole tip and a large block of the surface (see Fig. 5), but for surface-only calculations the unit cell may contain only a few atoms. Only the full interactions for this unit cell are calculated explicitly, and an Ewald summation is used to calculate the long-range electrostatic contribution of the infinite system to the total energy. MARVIN uses the conjugate gradient algorithm and a hybrid Newton algorithm to minimize the total energy with respect to the geometry of the unit cell.

Figure 5 shows how the tip and surface are represented within the atomistic simulation. The nanotip and the upper surface layers are divided into two regions, I and II. The region-I ions are relaxed explicitly, while the region-II ions are kept fixed to reproduce the potential

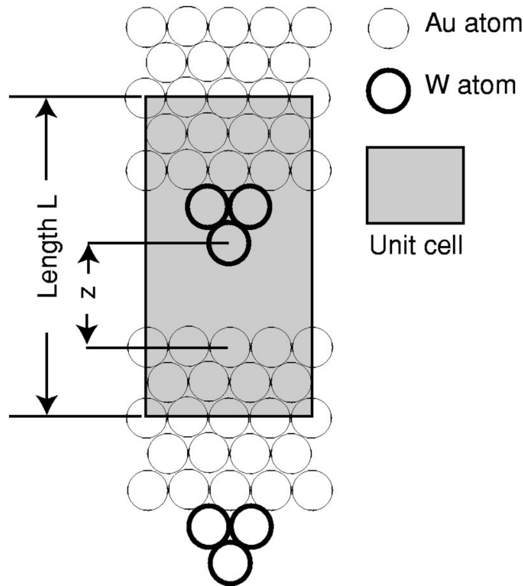

FIG. 6. Setup for the calculation of forces between an Au(111) surface and a W(111) tip. The tip is mounted on the reverse of a five-layer Au(111) film. By varying the vertical length L of the unit cell, an approach of the STM tip is simulated. The distance z between the surface and the tip (which is called the *piezoscale* distance if all atoms are in their groundstate positions) is changed due to relaxations of sample and tip atoms.

of the bulk lattice and the remaining tip ions on the relaxed ions. The calculation is periodic so that the infinite surface is represented; however, this means large surface unit cells must be used to avoid interactions between tip images in different cells. This is not a problem as atomistic simulation calculations are very cheap, and large systems do not represent a significant problem. It should be noted that the accuracy of this type of simulation depends critically on the quality of the parameters used to represent the interactions. The parameters for the interactions of the tip ions are well tested and are fully described in Grimes *et al.* (1989) and Shluger *et al.* (1994). The parameters for the surfaces studied will be discussed in the appropriate sections.

The total force acting on the tip takes into account the relaxation of the tip and surface atoms induced by the tip-surface interaction. It is calculated at a range of tip-surface separations, producing curves as a function of tip-surface separation for both energy and force. The shell-model contribution to the force is completely converged with respect to the size of the periodically translated simulation cell. By calculating these curves over many surface positions, one can generate a map of the microscopic tip-surface interaction. This can then be combined with the surface-position-independent macroscopic force to give the total tip-surface force as a function of tip-surface relative position $F(x,y,z)$. Note here that a slight "double counting" occurs when the microscopic and macroscopic forces are combined. The frozen atoms of the nanotip are in effect already part of the macroscopic tip and their van der Waals contribution to the force is effectively counted twice. However, this effect is very small, and it is more important to include a large enough tip that a significant number of atoms at the apex can be relaxed and also that the nanotip is kept neutral.

D. Modeling currents

A complete survey of all methods to calculate the tunneling current, developed over the last few decades, is given by Briggs and Fisher (1999). In increasing order of theoretical difficulty, the four main approaches are (i) the Tersoff-Hamann approach (Tersoff and Hamann, 1985a, 1985b), in which constant current contours are modeled from the electronic structure of the surface alone; (ii) the transfer Hamiltonian or Bardeen approach (Bardeen, 1961), in which the tip electronic structure is explicitly included in the calculation; (iii) the scattering or Landauer-Bütticker approach (Bütticker *et al.*, 1985), which includes multiple pathways of tunneling electrons from their initial to their final crystal states; and (iv) the Keldysh or nonequilibrium Green's-function approach (Meir and Wingreen, 1992), which also considers inelastic effects like electron-electron or electron-phonon scattering.

1. Tersoff-Hamann approach

This method is today incorporated into nearly every state-of-the-art DFT code. Despite an extension of existing simulation methods, especially with respect to quantitative comparisons between experiments and theory, it continues to be the "workhorse" (Lucas, 1990) of STM theory. In this method the tunneling current is proportional to the local density of states at the position of the STM tip (Tersoff and Hamann, 1985a, 1985b):

$$I(\mathbf{R}) \propto \sum_{E_n > E_F - eV_{bias}}^{E_n < E_F} |\psi(\mathbf{R},E_n)|^2 =: n(\mathbf{R},V_{bias}). \tag{7}$$

Here, I is the tunneling current, E_n the eigenstates of the crystal electrons, E_F the Fermi level, V_{bias} the bias voltage, and n the electron density. In many standard situations, e.g., in research on molecular adsorption or surface reconstructions, the model provides a reliable qualitative picture of the surface topography, even though it does not generally reproduce the observed corrugation values.

2. Perturbation approach

Within a transfer Hamiltonian approach, the two subsystems of sample and tip are treated as separate entities. This approach is also known as the Bardeen approach (Bardeen, 1961). The tunneling current is then described by the equation

$$I = \frac{4\pi e}{\hbar} \sum_{\mu,\nu} \left| \int_S (\chi_\nu^* \nabla \psi_\mu - \psi_\mu \nabla \chi_\nu^*) \right|^2 \delta(E_\nu - E_\mu - eV_{bias}). \tag{8}$$

Here, χ_ν are the eigenstates with energy E_ν of the STM tip, ψ_μ the eigenstates of the surface with energy E_μ. The integral extends over the separation surface S

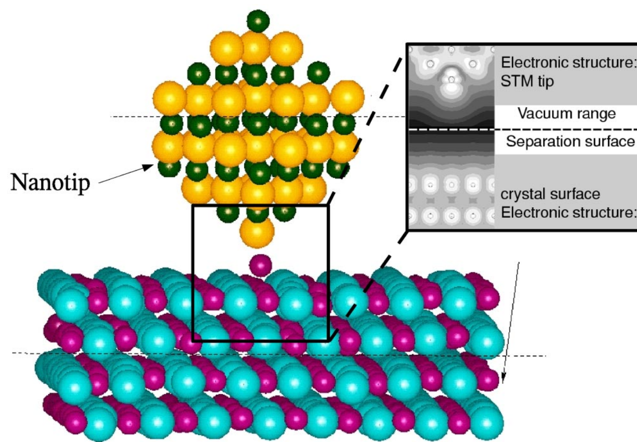

FIG. 7. (Color in online edition) Theoretical modeling of the STM current within a perturbation approach. The surface and the tip are treated as separate systems, and their electronic structure is determined by first-principles density-functional theory (DFT) calculations. The current through the separation surface is then determined by numerical integration at the plane of then surface.

between sample and tip, and the summation includes all eigenstates within a given interval from the Fermi level. This interval is determined by experimental conditions, e.g., the temperature within the STM. The scheme of the method is shown in Fig. 7.

It is clear from this expression that the quality of the wave functions in the vacuum range above the surfaces is decisive for good agreement between experiments and simulations. In fact, the most suitable expansion is a two-dimensional Fourier expansion in the lateral direction. Linear combinations of atomic orbitals in this respect have the disadvantage that they decay too rapidly into the vacuum, which in turn renders the currents and corrugations at a given distance unreliable.

3. Easy modeling: applying the Tersoff-Hamann model

Numerical methods for computing the tunneling currents from first principles by the Bardeen method, used to elucidate even subtle features of experimental images, are already well advanced (see the following sections). However, from a practical point of view it is frequently desirable to gain an understanding of experiments without highly demanding and thus very time-consuming model calculations. In principle, the Tersoff-Hamann model, which is based on the electronic structure of the analyzed surface alone, provides just such an easy method, especially since advanced codes in DFT generally come with an interface to compute constant-density contours in a straightforward manner. In this spirit, one seeks to determine the limits within which the method is reliable and to estimate the density contour value which roughly corresponds to a given tunneling current. Both of these objectives are attainable if the Bardeen method of calculating the currents is simplified by suitable approximations, which we shall demonstrate presently. Concerning the reliability of the Tersoff-Hamann model, the following criteria seem sufficient:

- No substantial chemical interactions between surface and tip.

This condition is not trivial to quantify, since the experimental measure of tip-sample separation, the tunneling resistance R, which is given by the ratio of applied bias voltage and tunneling current, $R=V_{bias}/I$, differs strongly for different systems and experimental conditions. On metal surfaces, the distance has to be larger than 5–6 Å. This corresponds, for an ambient environment and very-low-bias voltages (less than 80 meV) to a tunneling resistance R of 10–100 MΩ. Temperature enters this estimate because a thermal environment of transiting electrons allows them to reach a substantial higher number of final states, even under the condition of elastic tunneling. Under ambient conditions the energy difference between initial and final state can differ by about 80 meV. For this reason the experimental tunneling resistance (e.g., for a bias voltage of -1 mV and a current of 1 nA), and thus the estimate of the distance, can be quite misleading. Compared with the actual values obtained from explicit calculations of all possible transitions, the estimate under these conditions is too low by one or two orders of magnitude. Thermal excitations, in short, have an effect similar to that of increased bias voltages.

On semiconductors, the corresponding problem is the exact location of the Fermi level with respect to the upper band edge of the valence band. In this case the same condition (100 MΩ tunneling resistance) can lead to very small distances if the chosen bias voltage includes only very few states of the semiconductor surface. However, if the bias voltage is high enough (above 2 V, say), then this condition is usually sufficient.

- A feature size of surface structures which is well above the typical length scale of electron states of the STM tip.

This condition is far easier to quantify: since the typical length scale of a tip state is about half the interatomic distance of the tip metal, it is therefore between 1 and 2 Å. For feature sizes well above this value, the exact geometry of tip states will not enter the shape of the current contour in a decisive way. It is evident that this condition is in general not fulfilled in high-resolution scans, i.e., scans with atomic resolution. In all other cases it is quite safe to omit the explicit structure of the STM tip in a simulation.

Under these conditions the constant current contour can be related to the charge-density contour of the surface in a unique way. This can be done in the following way.

Most DFT codes contain a feature to sum up the charge density within a given energy interval. For a bias voltage of $-V_{bias}$, one starts by computing the density for the interval $E_F - V_{bias}$ to E_F. The appropriate con-

tour for a given current value can then be estimated with the following approximations:

(1) The bulk of the tunneling current passes through a small cross section of about 2 Å radius.

(2) The decay length of surface states (and tip states) is equal to the decay length of an electron state at the Fermi level of a metal surface with a work function $\Phi \approx 4$ eV. The wave function of the state is thus (in atomic units)

$$\psi(z)=\psi_0 e^{-kz}, \quad k=\sqrt{2\Phi}. \tag{9}$$

(3) The convolution of surface and tip states in the Bardeen integral is simplified by setting $\psi_{\text{sample}} \approx \chi_{\text{tip}}$ and by assuming that the first term in the integral is of the same order of magnitude as the difference:

$$I=C\cdot\left|\int_S dS\left(\chi_{\text{tip}}^* \frac{\partial \psi_{\text{tip}}}{\partial z}-\psi_{\text{sample}}\frac{\partial \chi_{\text{tip}}^*}{\partial z}\right)\right|^2 \approx C\cdot \Delta S^2 k^2 n^2(\text{sample}). \tag{10}$$

Here, C denotes a constant, ΔS the area of wave-function overlap, and n the electron density (see also Fig. 7). Since all the constants are known (Hofer and Redinger, 2000), the estimate is straightforward and yields

$$n(I)\ [\text{Å}^{-3}] \approx 2\times 10^{-4}\sqrt{I}\ [\text{nA}]. \tag{11}$$

For a current value of 1 nA, e.g., on a metal surface, the appropriate charge-density contour will thus be at 2×10^{-4} Å^{-3}.

4. Magnetic tunneling junctions

In a magnetic tunneling junction the rotational symmetry of electron spins of sample and tip surfaces is broken due to magnetic anisotropy. The spin states in this case are projected onto the crystal's magnetic axis. Depending on the orientation of the magnetic axes, two limiting cases have to be distinguished. The magnetic axis of sample and tip are either parallel (ferromagnetic ordering) or antiparallel (antiferromagnetic ordering). Ferromagnetic ordering is described by the following diagram:

$$\mathbf{M}_S\uparrow \quad \begin{Bmatrix} n_S^{\uparrow} & \rightarrow & n_T^{\uparrow} \\ n_S^{\downarrow} & \rightarrow & n_T^{\downarrow} \end{Bmatrix} \quad \uparrow\mathbf{M}_T. \tag{12}$$

In this diagram $\mathbf{M}_S$ and $\mathbf{M}_T$ describe the magnetic axes of sample and tip, n_S and n_T the spin density, and the arrows ↑ and ↓ spin-up and spin-down states, respectively. We denote the tunneling current due to ferromagnetic ordering by I_F. Antiferromagnetic ordering is described by

$$\mathbf{M}_S\uparrow \quad \begin{Bmatrix} n_S^{\uparrow} & \rightarrow & n_T^{\downarrow} \\ n_S^{\downarrow} & \rightarrow & n_T^{\uparrow} \end{Bmatrix} \quad \downarrow\mathbf{M}_T. \tag{13}$$

Within DFT the tunneling current is commonly described in terms of ϕ_M, the angle between the two magnetic axes, and $P_{S(T)}$, the polarization of the sample (tip) surface:

$$I(\phi_M)=I_0(1+P_S P_T\cos\phi_M), \tag{14}$$

$$\cos\phi_M=\frac{\mathbf{M}_S\cdot\mathbf{M}_T}{|\mathbf{M}_S||\mathbf{M}_T|}. \tag{15}$$

For constant tunneling matrix elements and within a perturbation approach the current I_0 and polarizations $P_{S(T)}$ are given by

$$I_0 \propto \frac{1}{2}(n_S^{\uparrow}+n_S^{\downarrow})(n_T^{\uparrow}+n_T^{\downarrow}), \tag{16}$$

$$P_{S(T)}=\frac{n_{S(T)}^{\uparrow}-n_{S(T)}^{\downarrow}}{n_{S(T)}^{\uparrow}+n_{S(T)}^{\downarrow}}. \tag{17}$$

I_0 and $P_S P_T$ can be written in terms of the ferromagnetic and antiferromagnetic currents:

$$I_0=\frac{1}{2}(I_F+I_A), \quad P_S P_T=\frac{I_F-I_A}{I_F+I_A}. \tag{18}$$

If the tunneling matrix element is not constant, the current has to be calculated numerically from the Bardeen integral over the separation surface (Bardeen, 1961; Hofer and Redinger, 2000). In this case the current contributions have to account for the spin orientation of a given eigenstate. In DFT the energetic minimum for magnetic crystals is reached by optimizing the distribution of spin-up density $n^{\uparrow}$ and spin-down density $n^{\downarrow}$. The currents for ferromagnetic and antiferromagnetic coupling are computed by calculating the transition matrix elements for the spin-polarized Kohn-Sham states of sample and tip:

$$I_F=I(n_S^{\uparrow}\rightarrow n_T^{\uparrow})+I(n_S^{\downarrow}\rightarrow n_T^{\downarrow}), \tag{19}$$

$$I_A=I(n_S^{\uparrow}\rightarrow n_T^{\downarrow})+I(n_S^{\downarrow}\rightarrow n_T^{\uparrow}). \tag{20}$$

The main advantage of the approach is its flexibility and robustness, while including the main physical effects under tunneling conditions. More involved approaches usually require the development of a program, which delivers DFT calculations and tunneling current simulations in a combined step. This usually leads to maintenance difficulties, as DFT codes become faster and more sophisticated. By contrast, the perturbation approach can be tailored to every DFT program, which provides the single Kohn-Sham orbitals of a surface. It can thus be used in combination with the DFT method most suitable for a precise description of the electronic surface properties.

The main disadvantage of this approach, from the viewpoint of scattering theory, is its unclear limit of application. Since it is based on perturbation theory, it relies on electronically decoupled surface and tip systems. The exact limits of the approach are difficult to estimate; in fact, these limits were determined by model calculations under conditions where the perturbation approach breaks down.

5. Landauer-Büttiker approach

Within a scattering approach the transition matrix is usually calculated based on the Landauer-Büttiker formula (Büttiker *et al.*, 1985). In this formulation the conductance G across a tunneling junction is given by the ratio of transmission probability to reflection probability. And since reflection probability R is close to unity, one obtains

$$G=\frac{I}{V_{bias}}=\frac{e^2}{\pi\hbar}\frac{T}{R}\approx\frac{2e^2}{h}\cdot T. \tag{21}$$

The tunneling current in this approach is usually written

$$I(V_{bias})=\frac{2e}{h}\int_0^{eV_{bias}}T(E)dE. \tag{22}$$

The transition probability matrix T, for multiple channels of the tunneling current, could in principle be evaluated in any basis set. However, the actual implementation of the formula is uniquely done within a tight-binding approach and based on atomic orbitals (Cerda *et al.*, 1997). The reason for this limitation is that the lateral position of the STM tip needs to be varied to obtain individual scan lines and thus the constant current contours, which can be compared to experiments. Within a DFT treatment of the problem, such a lateral variation is difficult for a reasonable system size because of periodic boundary conditions in the z direction.

The main advantage of the approach is its mathematical rigor and its inclusion of the different boundary conditions of the STM leads. In principle it should thus yield a more accurate description of the tunneling condition. In addition, the treatment includes interference effects between separate conductance channels. The main disadvantage today is its limitation to tight-binding models of surface and tip electronic structures, even if the parameters in these models are taken from first-principles simulations. Within a tight-binding model the localized basis set usually disagrees with the decay characteristics of current and corrugation found in the experiments.

6. Keldysh-Green's-function approach

During recent years theoretical treatments of the tunneling process on the basis of a nonequilibrium Green's-function formalism (Keldysh, 1965) have become increasingly popular (Reuter *et al.*, 2001; Taylor *et al.*, 2001). The most complete treatment of the problem considers the Hamiltonian of a system comprising two leads and a barrier region (Feuchtwang, 1974, 1975, 1976; Meir and Wingreen, 1992):

$$H=\sum_{k,\alpha\in L,R}\epsilon_{k\alpha}c_{k\alpha}^{+}+H_{int}(\{d_n^{+}\},\{d_n\}) + \sum_{k,\alpha\in L,R}(V_{k\alpha,n}c_{k\alpha}^{+}d_n+\text{H.c.}). \tag{23}$$

Here, the first term comprises the electron energy in the leads (L,R), the second term the orthogonal system of eigenstates in the barrier, and the third term the interactions between electrons in the leads and in the barrier. The tunneling current in this case is given by the following expression:

$$J=-\frac{2e}{\hbar}\int dE[f_L(E)-f_R(E)] \times \text{Im}\left[\text{Tr}\left(\frac{\Gamma^L\Gamma^R}{\Gamma^L+\Gamma^R}G^R\right)\right]. \tag{24}$$

In this formulation it is assumed that the coupling to the leads, given by Γ_L and Γ_R, differs only by a constant factor. The full Green's-function G_R of the Keldysh approach includes all inelastic processes, spin flips, and multiple scattering events. If we analyze the time scales involved in tunneling processes, then we get for normal tunneling conditions $(I\approx 1\,\text{nA})$ an interval between single-electron processes of about 10^{-10} s. Considering that this interval is 100–1000 times longer than the typical time scale of lattice excitations, it seems safe to neglect interactions of electrons in the barrier. In this case Eq. (24) reduces essentially to the Landauer-Büttiker formula:

$$I=\frac{e}{\hbar}\int dE[f_L(E)-f_R(E)]\text{Tr}[t^{+}(E)t(E)]. \tag{25}$$

In principle this approach could also be used to compute the tunneling current. However, since the interaction of electrons within the vacuum barrier is negligible, tunneling currents are not usually calculated within this theoretical framework. Due to the wide range of interactions included in the formalism, Keldysh's method is the most accurate today. Its main problem is the computational cost, which either has to be made up for by approximations in the description of the solid-state systems, or by limiting the number of atoms in the interaction range.

E. Modeling oscillations

Although for scanning force microscopy in general, the controlling interaction is the force between tip and surface, for an NC-SFM we must also contend with the fact that the real experiment uses an oscillating cantilever. The link between the tip-surface interaction and an NC-SFM simulated image is a model of the oscillations of the cantilever under the influence of the tip-surface interaction. Detailed analyses of the tip oscillations and ways to model them are given by Giessibl (1995, 1997); Aimé *et al.* (1999); Giessibl *et al.* (1999); Sasaki and Tsukada (1999); Dürig (2000); Schwarz, Hölscher, and Wiesendanger (2000); García and Pérez (2002); Morita *et al.* (2002). However, a simple model can be derived under some basic assumptions. For a tip oscillating with large constant amplitude above the surface, and the tip deflection measured at constant frequency change, the oscillations of a cantilever over a surface point (x,y) driven by an external force F_{ext} in a force field $F(z)$ can be described by the equation of motion

$$\ddot{z}+\frac{\omega_0^2}{k}\alpha\dot{z}+\omega_0^2 z-\frac{\omega_0^2}{k}F(z+h)=\frac{\omega_0^2}{k}F_{ext}, \qquad (26)$$

where ω_0 is the oscillating frequency of the cantilever in the absence of any interaction with the surface, k is the spring constant of the cantilever, α is the damping coefficient, and h is the equilibrium height of the cantilever above the surface in the absence of interaction. At constant amplitude and frequency change we can assume that any damping is completely canceled by the external force and that $F(z)$ does not depend on time. This simplifies Eq. (26) to

$$\ddot{z}+\omega_0^2 z-\frac{\omega_0^2}{k}F(z+h)=0. \qquad (27)$$

Following the derivation of Livshits *et al.* (1999) we finally obtain the frequency of cantilever oscillations in the presence of the interaction ω as

$$\left(\frac{\omega}{\omega_0}\right)^2=1-\frac{1}{\pi k A_1}\int_0^{2\pi}F(z+h)\cos(\tau)\,d\tau. \qquad (28)$$

Note that there are some subtle differences in the oscillation behavior between the externally driven cantilever discussed here and a self-driven cantilever (Hölscher *et al.*, 2001) used in some experiments. However, these differences do not significantly affect the following discussion.

F. Generating a theoretical surface image

Shifting the position of the SPM tip laterally and vertically produces, by the above procedure, a map of tunneling currents in scanning tunneling microscopy or changes in frequency of the oscillations of the cantilever due to the influence of the tip-surface interaction in scanning force microscopy.

The current maps are used to extract the contours of constant current microscopy, or the change of current with a change of the applied bias voltage spectroscopy. In a further step the maxima and minima of the current contours for a specific current value are determined. This corrugation amplitude is then directly compared to images. It is clear from the procedure that specific tunneling conditions (bias voltage and tunneling current) uniquely determine a constant current contour and a corrugation amplitude. In this sense the calculation does not involve any parameter or fit to experimental data. Therefore it can be said to be fully *ab initio*.

In SFM simulations the map is interpolated to find the cantilever deflections to keep the cantilever oscillating at a constant frequency change (or constant modified frequency). The deflections can then be plotted as a function of surface position (x,y) to give the theoretical image. At this point, the theoretical image and data can be compared with the experimental equivalents. It should be noted that the theoretical image is generated using experimental values for all known parameters such as frequency ω_0, amplitude A_1, elastic constant k, and frequency change $(\omega-\omega_0)$. All parameters that are not known from experiment, such as tip radius, are taken from the best experimental or theoretical estimate, as appropriate. The specific parameters used for each system studied will be discussed in later sections.

G. Summary

Although we have outlined consistent methods for simulating the fundamental aspects of SPM experiments, no model can reproduce all features of a physical environment. In this sense every model depends crucially on basic assumptions, and for the applications we discuss here, these are, for scanning probe microscopy in general, as follows:

- The ground-state properties of a system are equal to the properties at finite temperatures (e.g., in an ambient environment).
- There is a hierarchy of interactions that allows separation of different effects in the theoretical models (no inclusion of, for example, cumulative or time-dependent interactions).

For scanning tunneling microscopy specifically,

- Macroscopic interactions do not affect the tunneling current.
- The resistance in the STM circuit is only due to the tunnel barrier.
- The current cross section is centered at the apex atom of the tip.
- Current flow does not change the properties of a system.

The last point has recently been analyzed by Todorov *et al.* (2000), and it was found that the current flow slightly changes the position of the surface atoms. The assumptions for scanning force microscopy specifically are as follows:

- Charge transfer between tip and surface is not a significant component of the interactions for an insulating surface.
- The effects of the system electronics, such as apparent dissipation (Gauthier and Tsukada, 1999; García and Pérez, 2002; Morita *et al.*, 2002), do not affect the physics of the tip-surface interaction.

Note that the effect of charge transfer on the interactions of a pure silicon tip are discussed to some extent in Sec. V.C.1.

V. STUDYING THE SURFACE

In this section we review the applications of SPM methods to some characteristic classes of materials and the extra information that theory provides over experiment alone.

For scanning tunneling microscopy, we mainly study applications of the transfer Hamiltonian method (Bardeen, 1961) to plain and contaminated metal/

semiconducting surfaces. The emphasis in this section will be on demonstrating how simulations extend the experimental method. Only when STM scans are simulated do the physical origins of measured effects become accessible. In particular, we shall focus our demonstration on model calculations aimed at solving the widely discussed problem of the relaxation of tip/surface atoms and their effect on the tunneling current on a gold surface. Simulations also demonstrate the exact limitations of the perturbation approach.

For scanning force microscopy, we focus on studies of several classes of insulating surfaces, each demonstrating specific features important to understanding imaging: (i) clear image interpretation from the complex CaF_2 (111) surface, and (ii) imaging of covalent structures in an insulating surface from the molecular solid surface, calcite $(10\bar{1}4)$.

Finally, we look at thin insulating films, where both scanning tunneling microscopy and scanning force microscopy can contribute. Here we see the influence of low-coordination sites in imaging, especially the increased contrast at kink and corner sites for SFM imaging of NaCl thin films.

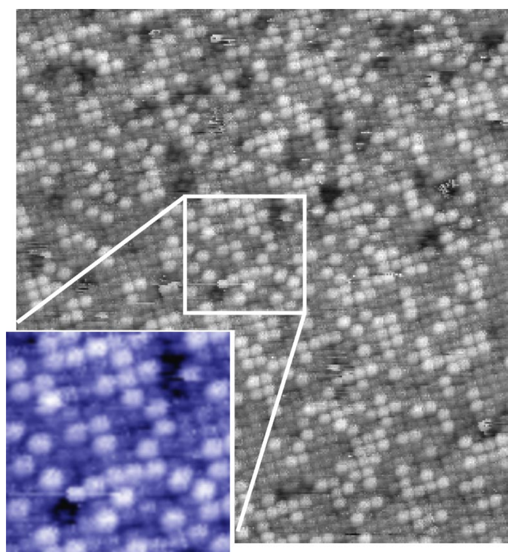

FIG. 8. (Color in online edition) Scanning tunneling microscope scan of a binary PtRh(100) surface. Rh atoms possess a different electronic structure due to alloying with adjacent Pt atoms, they are therefore clearly discriminated by their greater apparent height (see detail). Measurements of this type are the first real-space visualizations of chemical atoms. Reprinted with permission (Wouda *et al.*, 1996).

A. Metal surfaces

Metal surfaces have been widely studied by scanning tunneling microscopy and other methods. There have been only a very few NC-SFM studies of these surfaces (see, for example, Loppacher *et al.*, 2000) as most of the SFM effort is focused on semiconductor and insulating surfaces. The main results include (i) *reconstructions*, or surfaces with a different arrangement of surface atoms than in the bulk; (ii) *relaxations*, or the trend for surface layers to possess a different interlayer spacing than bulk crystals; and (iii) *surface states*, or electron states trapped in the surface region due to the potential boundary (Inglesfield, 1982; Wille and Durham, 1985).

The surface chemical composition plays an important role in STM imaging of metal surfaces. It is a well-known fact in STM experiments that oxygen or carbon atoms on a surface change the image locally in a decisive way (Bischoff *et al.*, 2001; Hofer, Fisher, Wolkow, and Grütter, 2001). Both atoms usually appear in STM images as distinct depressions, even though their actual position is sometimes well above the surface plane. Hence one of the main problems in STM experiments on metals is the contamination of the bulk with carbon. On the other hand, oxygen on a surface can lead to a stable reconstruction of the entire surface, and this effect may be used to render imaging actually easier than on a clean metal surface. These are very drastic examples of chemical effects changing the tunneling current on surfaces. Similar effects, even though not as drastic, change the apparent image of single atoms on a surface depending on the chemistry of their neighbors (Hofer *et al.*, 1998).

It took about ten years, from the invention of the STM (Binnig and Rohrer, 1982; Binnig *et al.*, 1982a, 1982b), until the instruments were precise enough to be able to discriminate not only between substrate atoms and adsorbates, or different adsorbates, but even between different substrates, e.g., metal atoms (Schmid *et al.*, 1993). The experiments marked an important point, because they made the concept of a chemical atom visible for the first time. An atom, henceforth, could be seen as a small sphere in some shade of gray (see Fig. 8).

But if the chemical nature of a substrate atom can change the observed STM image, the chemical nature of the tip apex can also have a decisive role. This effect changed the focus in STM theory somewhat from a discussion about single tip orbitals (most theoretical work previously assumed that the representation of a tip by one orbital would be sufficient), to the chemistry of the STM tip. This is still a very lively topic today, not least because subtle effects are more and more predominant in experimental practice. All these effects can be substantially influenced by the chemical composition of the STM tip (Hofer and Redinger, 2000).

Another issue acknowledged in STM research nearly from the beginning is that chemical forces must play an important role in the imaging process (Pethica and Sutton, 1988; Sacks and Noguera, 1988; Cho and Joannopoulos, 1993; Clarke *et al.*, 1996; Ventra and Pantelides, 1999; Sacks, 2000) on metal surfaces. The strong adhesion interaction between an atomically defined W(111) tip and an Au(111) sample has been studied recently using an NC-SFM (Cross *et al.*, 1998). However, the exact mechanism, and, more importantly, the quantitative effect of the tip-surface chemical interaction in STM images, could not be conclusively determined. It was, for example, unclear whether these forces would lead to a contrast reduction, an enhancement only in the low-distance regime, or no effect at all for scanning on close-

packed metal surfaces. Especially the so-called "giant corrugation" on Au(111) or Al(111) remained a puzzle for over 15 years.

To study the problem of chemical forces on a model surface, a combined tip-sample system consisting of an Au(111) surface and a W(111) tip was simulated (Hofer, Fisher, Wolkow, and Grütter, 2001). By reducing the unit cell in the z direction, the approach of an STM tip to a sample surface can be described. To obtain the real corrugation height on the surface a simulation of the coupled system was performed for two separate tip positions, the on-top position and the threefold hollow between Au atoms (see Fig. 6). The main problem in such a simulation is the scale of numerical calculations. To be sufficiently precise, the unit cell has to be reduced in steps of about 0.01 nm in the range where chemical forces are noticeable. Given two separate configurations and a vertical distance scale of about 0.2 nm, this amounts to several weeks of computation time on a massively parallel computing unit. From an initial tip-sample separation of 1 nm the distance was gradually reduced, initially in steps of 0.05 nm. At every step the system was fully relaxed. The onset of significant mechanical interactions between tip and sample occurs at about 0.5 nm. Surface wave functions were computed for the fully relaxed sample and tip systems at every distance and for two tip positions. In this part of the calculation the initial system was separated into two subsystems, a surface system and a tip system. The wave functions of the separate systems provided the input for the current calculation within the Bardeen approach (see previous sections). The procedure leads to separate constant current contours of the surface, depending on the position of the tip.

The calculations establish an early onset of relaxations, which depend strongly on the position of the tip. For the on-top position of the STM tip we observe an onset of forces and relaxations at about 0.47 nm. The surface atom reaches its furthest distance from the surface at a tip-sample separation of 0.45 nm; it is then 0.13 nm above its position on the isolated surface. This point marks the beginning of atomic instability, which in the case of atomic transfers is observed as a hysteresis of forces in single approach/retraction cycles (Cross *et al.*, 1998). If the tip is in the threefold hollow, the onset of forces and relaxations is substantially retarded and occurs at 0.43 nm. The maximum outward relaxation of the three gold atoms is somewhat lower at about 0.1 nm (reached when the tip-sample separation is 0.41 nm). The tungsten tetrahedron of the STM tip relaxes about the same amount in both positions: the apex atom approaches the sample up to about 0.05 nm at the point of closest approach. The change is due to an increase of the interlayer distance of the tungsten atoms by about 0.01–0.02 nm, and a buckling of the layers underneath, which extends about two layers into the lead. The forces on the tungsten tip are shown in Fig. 9. The values for tip-sample relaxations are given in Fig. 10(a). Owing to the strong interactions between tip and sample at close range, the core-core distance between tip and sample is decreased. The net effect of relaxations is a decrease of the distance between tip and sample. A deviation of about 0.2 nm between the distance inferred from simulations, and the distance inferred from measurements of the current decay in the long-distance range, has actually been observed (Hofer, Redinger, *et al.*, 2000). In the critical range of 0.46 to 0.41 nm, the actual distance changes by about 0.2 nm. This points to an effect frequently observed in experiments with atomic resolution: it is difficult to obtain atomically resolved images because sizable corrugations in most cases require a distance below 0.5 nm, but in this mechanically highly unstable situation the tip easily jumps into contact with the surface. This, in turn, destroys the microstructure of the atomic arrangement at the tip apex and leads to a sudden change of the observed image.

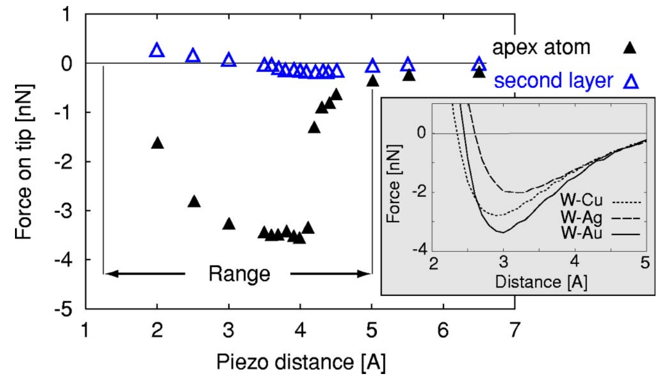

FIG. 9. (Color in online edition) Distant-dependent forces on (full triangles) the apex atom, and (empty triangles) the subsurface atoms of the tungsten tip above the hollow position of the surface. The forces show a steep onset at about 4.6 Å, and the range of forces is approximately 4 Å. Forces are generally limited to the apex atom. For comparison we show the forces between diatomic dimers. In this case it is seen that the force characteristics above 4 Å do not depend on the chemical nature of the surface atom. Reprinted with permission (Hofer, Fisher, Wolkow, and Grütter, 2001).

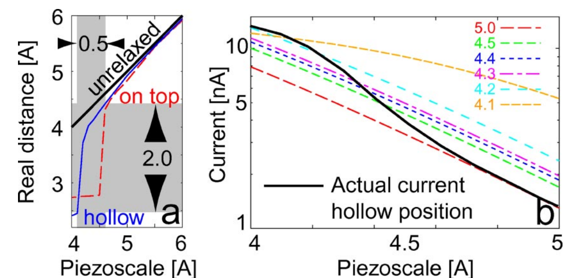

FIG. 10. (Color in online edition) Tip-sample relaxations and current: (a) distance-dependent tip-sample separation versus the theoretical distance, and (b) current curves for frozen atomic positions during an approach. The tip-sample separation changes by about 2 Å within 0.5 Å of the theoretical (piezo) scale. Due to atomic relaxations the actual current does not follow an exponential characteristic, but shows an excess of about 100% over 1 Å distance. Reprinted with permission (Hofer, Fisher, Wolkow, and Grütter, 2001).

The curves in Fig. 10 show the current for the hollow position. We obtained the change due to surface and tip relaxations by calculating the current in frozen atomic configurations of sample and tip. These configurations are different for every piezoscale distance, as are the logarithmic graphs of the tunneling current. The z labels on individual graphs give the tip-sample separation before relaxation (=piezoscale). It is interesting to note that the logarithmic current curves are more or less straight lines down to 4.1-Å tip-sample separation. At this point the atom at the apex of the tungsten tip is so far apart from the adjacent atoms that the wave functions in the vacuum above the tip change from crystal wave functions to atomic orbitals. This feature accounts for the highly nonlinear behavior of the tunneling current, since it is now composed of components that comply with the exponential decay of the crystal wave funtions above the tungsten subsurface atoms as well as components that result from the overlap with the atomic wave functions of the separated apex atom.

The true increase in the current is determined by taking only a single point of each graph. In practice we interpolated between the computed points to obtain the smooth black curve shown in the figure, giving an enhanced increase in the current. For an experimentalist who estimates the potential barrier between tip and sample from the exponential decay of the current, the apparent barrier height increases in this range. Note that the current was calculated for a sample bias of -0.1 V.

To determine the true surface corrugation, the tunnel currents in the simulations were assumed to be 5.1 nA in both configurations (tip on top of an Au atom and tip in the hollow between Au atoms), but owing to the site-dependent relaxation of the systems the two constant current contours differ. The piezoscale would give a distance of 0.47 nm on top of a gold atom and 0.45 nm in the fcc hollow site. These distances are at the lowest limit of stability for the tip-sample system. The difference of 0.02 nm describes the experimental corrugation of the Au(111) surface when measured with a tungsten-terminated tip (Hallmark *et al.*, 1987). The simulated scans with the tips and surfaces frozen in the two configurations are shown in Figs. 11(a) and (b). Figure 11(c) shows two simulated line scans across a single atom. The two separate curves describe the line scan for the two setups used (on top and hollow). It can be seen that the relaxation leads in effect to an enhancement of the corrugation by about 0.13 nm. Only with this relaxation included is agreement between experiment and simulation obtained (Hallmark *et al.*, 1987). The problem of "giant corrugations" on close-packed metal surfaces can therefore be assigned to chemical forces between tip and surface.

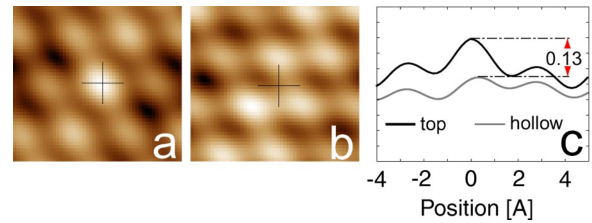

FIG. 11. (Color in online edition) Current contour plots using the relaxed configurations of sample and tip for a distance of 4.7 Å [frame (a) tip on top of an Au atom], and 4.5 Å [frame (b) tip in the threefold hollow position]. (c) Simulated line scan from left to right across a single atom, black line for the setup in the on-top position, and gray line for the setup in the hollow position. All scans correspond to a current of 5.1 nA. An actual scan would have enhanced corrugation due to relaxation effects [see dash-dotted lines in frame (c)]. Reprinted with permission (Hofer, Fisher, Wolkow, and Grütter, 2001).

B. Semiconductor surfaces

Semiconductor surfaces have an enormous range of technical applications and have therefore generated an impressive body of experimental and theoretical research. The principal surfaces under investigation are Si(100) and GaAs(100). The Si(111) surface, even though widely imaged by SPM's, is substantially less important technologically. In fact, it is today mostly imaged to calibrate the instrument and to study adsorption of various species.

1. Silicon surfaces

The surface of Si(100) reconstructs in dimer rows along the (011) direction, where the Si-Si dimer bond is 2.2 Å long and adjacent dimers are 3.8 Å apart (Hofer, Fisher, Lopinski, and Wolkow, 2001). The dimer reconstruction was the subject of intense dispute around 1990, since photoemission spectra suggested a buckled dimer (Bringans *et al.*, 1986), while STM images clearly revealed a flat dimer structure (Hamers *et al.*, 1986). The riddle has been solved by a combination of experimental and theoretical techniques. Experimentally, it was realized that a tilted dimer in fast flip-flop motion would appear flat in STM images due to the low time resolution of the STM. At temperatures below 90 K the motion of dimers is frozen. Individual dimers under these conditions appear tilted, as Wolkow showed in 1992 (Wolkow, 1992). The same feature is observed if the buckling is pinned down by surface defects.

Comprehensive electronic structure calculations based on DFT established that the ground-state surface structure is a (2×1) reconstruction, where adjacent dimers are tilted in opposite directions (Payne *et al.*, 1989; Dabrowski and Scheffler, 1992). The energy difference of 80 meV between a flat and a tilted dimer agrees well with the thermal conditions at room temperature, where this activation barrier is easily overcome by thermal fluctuations. It is currently established opinion that this dynamic buckling is the reason that the dimers appear flat in STM images (Hata *et al.*, 1999). Dynamic buckling was modeled by calculations of the electronic surface structure in various positions of the dimer and by averaging the ensuing STM images over full cycles of dimer motion (Hofer, Fisher, Lopinski, and Wolkow, 2001). As the simulations reveal, this statistical average is virtually indistinguishable from the image based on

flat Si dimers. Given the large distance between the STM tip and the sample surface of 6 Å under typical conditions (-2 V, 50 pA), the assumptions of current-induced buckling (Badziag *et al.*, 1991), or buckling due to tip-surface interactions (Clarke *et al.*, 1996) seem to lack experimental and theoretical confirmation.

Recent tight-binding simulations of NC-SFM imaging of the Si(001) surface with a silicon tip (Tagami and Tsukada, 2000) demonstrated a very strong effect of the tip-surface interaction on the image contrast. In particular, it was found that as the tip approached the down dimer atom to about 3.5 Å this atom suddenly adhered to the tip. This in turn resulted in the discontinuous increase of the attractive force on the tip. In a similar way, when the tip was retracted from the surface, the buckling angle of the dimer changed drastically at a certain tip height where the force again showed a discontinuous jump. The buckling orientation was reversed after one cycle of cantilever dynamics. If the tip did not get that close to the surface, the described atomic instability did not occur. However, simulations with a Si tip predict that only the upper dimer atom will be visible. By their thermal average, the images at room temperature are predicted to have (2×1) periodicity, as observed experimentally both in NC-SFM's (Uchihashi *et al.*, 1999) and STM's (Wolkow, 1992). The described tip-induced instability of the surface (or tip) atoms is characteristic for any surface and was first observed in SFM modeling of tip interaction with a metallic surface (Pethica and Sutton, 1988). A qualitatively similar behavior involving an up dimer atom has been observed in simulations of the interaction of a Si(001) surface with a carbon nanotube tip modeled by C_{60} (Tagami *et al.*, 2000).

In SFM studies of semiconductors, the Si(111) 7×7 surface has attracted much more theoretical simulation. Greatest success was achieved in a full *ab initio* theoretical study (Pérez *et al.*, 1997) of the forces and contrast mechanism for that system. This study demonstrated that the force between a model silicon tip and surface would be dominated by the onset of covalent bonding between a localized dangling bond at the apex of the tip and dangling bonds on the surface adatoms. More importantly, the tip-surface force over the adatoms was calculated directly, giving a direct measure for comparison with experiment. In an extended study (Pérez *et al.*, 1998), force calculations were also performed over the rest atoms in the silicon surface, demonstrating the possibility of imaging both sites in an experiment. This "force spectroscopy" over the surface unit cell is the most quantitative tool for comparison between experiment and theory, yet it remains a significant challenge experimentally. Only low-temperature NC-SFM experiments on the silicon (111) 7×7 surface (Lantz *et al.*, 2000) obtained the sensitivity to really measure the forces over specific atomic sites. A direct comparison of the magnitude of these forces with the theoretical results gave good agreement, supporting the theoretical assumption that the tip apex is basically silicon, and that the silicon surface adatoms would be imaged as bright. However, theory seemed to underestimate the softness of the tip, and a much wider force minimum was observed in experimental force curves. Increasing the size of the tip and allowing more tip ions to relax reduced the discrepancy between theory and experiment, but could not eliminate it. Nevertheless, the agreement in magnitude of forces between experiment and theory gives strong support to the dangling-bond interaction as the mechanism of contrast for high-quality images of the silicon (111) 7×7 surface.

2. Binary semiconductor surfaces

In SFM studies of more complex semiconductor systems, theoretical modeling has not been so successful in resolving image interpretation problems. Experiments have been performed on complex binary semiconductors such as InP (Sugawara *et al.*, 1995) and InAs (Schwarz, Allers, *et al.*, 2000), but interpretation of images is difficult. On the InAs(110) 1×1 surface with low temperature NC-SFM, Schwarz *et al.* (Schwarz, Allers, *et al.*, 2000) observed direct experimental evidence for tip-induced relaxation of the two neighboring As atoms around an individual In vacancy. *Ab initio* calculations of InP (Tóbik *et al.*, 1999, 2001) and GaAs (Ke *et al.*, 1999, 2001) demonstrated that in general for III-V semiconductors the anion is imaged as bright with a silicon tip, agreeing with experimental results on InAs. However, both simulation and theory saw a strong dependence of contrast on the tip atomic structure and it was not possible to make a universal unique interpretation of images. Tips with adsorbed surface species produced very different interactions compared to pure silicon tips.

C. Insulating surfaces

In this section we briefly review some of the simulation methods discussed above as applied to insulators. Due to the requirement of a conducting surface for STM imaging, this section focuses almost exclusively on scanning force microscopy.

Difficulties in preparing clean, flat, insulating and semi-insulating surfaces has so far limited successful atomic resolution to only a few surfaces, such as NaCl (Bammerlin *et al.*, 1997) and several other alkali halides (Bammerlin *et al.*, 1998), TiO_2 (Fukui *et al.*, 1997a), CaF_2 (Reichling and Barth, 1999), NiO (001) (Hosoi *et al.*, 2000), KBr (001) (Hoffmann *et al.*, 2002), and Al_2O_3 (0001) (Barth and Reichling, 2001). However, only in the case of TiO_2 experimental studies (Fukui *et al.*, 1997b) of the adsorption of formate ions on the (110) 1×1 surface has chemical identification been established fairly conclusively: the bridging oxygen ions on the surface were imaged as protrusions in an NC-SFM. This result was achieved by combining scanning tunneling microscopy and NC-SFM and using the theoretical interpretation of the STM images as an aid in interpreting NC-SFM images of the same surface. Recent combined STM and NC-SFM theoretical modeling (Ke *et al.*, 2002) has confirmed the original experimental interpretation. Although this double technique is very use-

ful for extracting more information than is available from only one type of experiment, it is, by the nature of the STM, limited to surfaces that can be made to conduct. Although the stoichiometric TiO_2 surface is insulating, real surfaces are always nonstoichiometric, and the oxygen vacancies introduce surface states that significantly reduce the band gap.

Although not strictly within the insulating surface class (at least not for graphite), success in interpreting atomically resolved NC-SFM images was achieved on the van der Waals surfaces of graphite (0001) (Hölscher *et al.*, 2000) and xenon (111) (Allers *et al.*, 1999). For xenon, theory and experiment gave excellent agreement on Xe atoms as the bright contrast centers. However, for graphite the interpretation was more complex, with the hollow sites in between six carbon atoms responsible for the strongest interaction, and bright contrast in images.

In spite of extensive theoretical modeling (Shluger and Rohl, 1996; Shluger *et al.*, 1999; Foster, Hofer, and Shluger, 2001), interpretation of NC-SFM images of wide-gap insulators, such as alkali halides, has proven to be much less conclusive. This is mainly due to the structural equivalence of anion and cation sites and ambiguity in the nanotip structure discussed below. Nevertheless modeling of NC-SFM on these materials have allowed us to establish some general features of the tip-surface interaction responsible for image contrast.

In particular, for realistic macroscopic tip parameters, the interaction of ionic nanotips (such as the MgO cube nanotip) with these ionic surfaces predicts image contrast in broad agreement with experiment (Livshits *et al.*, 1999). This is an indication that all relevant forces are accounted for in the simulation. The image contrast (the variations in the frequency change over different surface sites) has been shown to be determined primarily by the electrostatic interaction between the nanotip and the surface. We should stress that this interaction is caused by the whole surface and whole nanotip rather than individual surface and tip ions. The balance of forces acting, for example, on the tip ion closest to the surface is determined by the full surface electrostatic potential, which decreases exponentially with the distance from a neutral, ideal, and rigid surface, and the full tip electrostatic potential. Any surface or tip defects, such as surface steps, vacancies, adsorbed ions and even strong displacements of regular ions from their sites cause much more long-range Coulomb and dipole contributions to the interaction. This has two main consequences. First, displacements of the surface and tip ions from their regular sites caused by the tip-surface interaction strongly enhance the image contrast with respect to a rigid tip and surface (Livshits *et al.*, 1999). Second, charged surface defects, such as impurities, vacancies and adsorbed ions, should give strong image contrast (Livshits *et al.*, 1999; Kantorovich, Foster, *et al.*, 2000). As we shall show later, even neutral step edges enhance image contrast with respect to regular surface sites (Bennewitz *et al.*, 2000).

Yet another important consequence of the electrostatic interaction is that the sign of the surface electrostatic potential alternates and is opposite, for example, above Na^+ and Cl^- surface sites. For an atomically sharp tip, like the one shown in Fig. 5, the repulsion and attraction above different surface sites will depend on the sign of the electrostatic potential at the end of the tip. For example, the O-terminated MgO cube nanotip shown in Fig. 5 has a negative electrostatic potential and will be attracted to Na^+ sites in the NaCl (001) surface and repelled from Cl^- sites. The Mg-terminated MgO cube nanotip, on the other hand, will be attracted to the Cl^- sites. Of course, this interaction will be much less clear-cut for more complex tip and surface structures. However, this simple model illustrates the main problem of interpretation of NC-SFM images of high symmetry surfaces, such as NaCl: unless the sign of the tip potential is known, alternative interpretations of the chemical identity of the surface ions are equally possible. The same is true even for less symmetric surfaces of TiO_2. On this surface identification of the chemical surface species was achieved by marking certain surface sites by adsorbing some atoms or molecules which will stick only to these sites (Fukui *et al.*, 1997b).

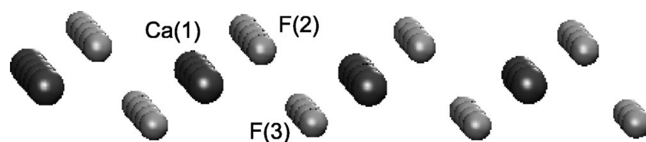

FIG. 12. Fluorine terminated CaF_2 (111) surface. Ca(1) the calcium layer; F(2) the outermost fluorine layer; and F(3) the lower fluorine layer. The layers are separated by 0.08 nm.

Another possible method for reliable interpretation of images is to exploit the dependence of contrast on the tip structure and properties, for example, when imaging a lower-symmetry surface, where tips with different sign of electrostatic potential give qualitatively different contrast patterns. This was done for the bulk wide-gap insulator CaF_2, for which the collaboration between theory and experiment played a crucial role in establishing the chemical identity of image features. We shall use this system as an example for illustration and critical analysis of the theoretical method discussed above.

1. The calcium fluoride (111) surface

The CaF_2 (111) surface has been demonstrated to be fluorine terminated (Reichling and Barth, 1999) and, as can be seen from Fig. 12, the outermost fluorine layer protrudes from the surface. For convenience, in further discussion we shall call the fluorine ions in the upper surface layer [labeled F(2) in Fig. 12] "high" F^- ions, and these in the third surface layer [labeled F(3) in Fig. 12] "low" F^- ions. It is interesting to note that high F^- ions stick out of the surface in a similar manner to the bridging oxygens seen on the TiO_2 surface or As atoms in the InAs surface. A common assumption in dynamic SFM imaging has been that protruding atomic layers are imaged as bright, and it is important to establish whether this "intuition" holds theoretically.

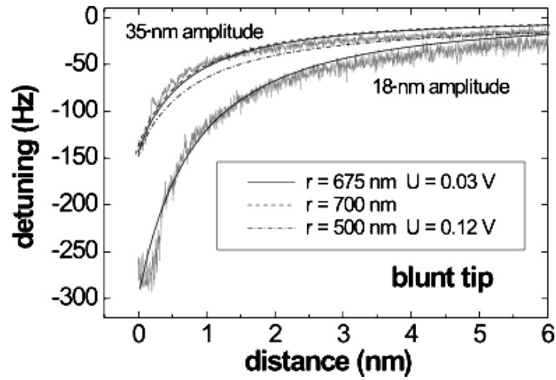

FIG. 13. Comparison of experimental and theoretical force-distance curves for three different tip radii r.

a. Tip characterization with force curves

For reliable modeling of atomic contrast, one needs knowledge about the atomic configuration at the tip end as well as information on the material, shape, and curvature of the tip. These latter parameters can be estimated by an analysis of experimental frequency detuning curves as a function of the tip-surface distance. As has been shown in Foster, Kantorovich, and Shluger (2000) and Guggisberg *et al.* (2000), such analysis can help to determine interrelations between the main mesoscopic forces (such as van der Waals, capacitance, and electrostatic force due to tip and/or surface charging), which contribute to the background force. The background force determines the average frequency detuning during scanning, whereas the relation between different constituent forces contains information about tip shape, composition, and charge (Foster, Kantorovich, and Shluger, 2000). This information can then be used as input for theoretical simulations of SFM images.

The experimental procedure employed to measure frequency detuning vs distance curves and characterize the tips used in CaF_2 surface imaging is thoroughly described by Barth *et al.* (2001). The main idea is to make this measurement *in situ* immediately after taking the last image. We should note that lateral thermal drift of the sample, which is unavoidable at room temperature, does not allow precise tip positioning over a specific ionic site. Therefore these data represent an average over a spread of lateral positions. However, as the force curves are analyzed only with respect to long-range forces, this uncertainty does not affect the conclusions presented below.

In NC-SFM imaging it is common practice to minimize long-range electrostatic interactions by applying a bias voltage, a procedure similar to that described by Bennewitz *et al.* (1997), and this was also done for the measurements shown in Fig. 13. The measured frequency detuning curves strongly depend on tip preparation. The curve in Fig. 13 was prepared by bringing the tip into contact with the surface to blunt it.

Using the SFM model described above, the theoretical curves were fitted to experimental data obtained at both oscillation amplitudes. The macroscopic van der Waals force between the tip and surface is proportional to the tip radius and the Hamaker constant. The value of the Hamaker constant was fixed at 1 eV, corresponding to a characteristic value for the interaction between silicon and a wide-gap insulator (French *et al.*, 1995). Therefore the only free parameters of the fit were the tip radius and the bias voltage. The bias voltage applied in the theoretical model affects long-range electrostatic forces due to uncompensated tip and surface charge and to image interaction (Foster, Kantorovich, and Shluger, 2000).

The best fit results are shown as dashed lines in the graphs of Fig. 13. The tip parameters for the fit are the same at both amplitudes, confirming that theory gives a consistent agreement. Distances given in the graphs of Fig. 13 have been obtained by shifting experimental data to align with theoretical curves, assuming that closest approach of the tip to the surface occurs at 0.4 nm. We should stress that this is clearly a crude estimate. It is based on previous intuitions regarding closest approaches in experiments, and we shall show later that modeling predicts much closer approaches. However, errors of the order of 0.1 nm in background force distances does not strongly influence the results, since contrast is determined by the microscopic forces where distance is clearly defined.

The theoretical best fit was found for a tip radius of 675 nm and 0.03-V bias voltage. It should be noted that, within the assumptions discussed above, these parameters are unique, and a similar fit could not be found with an increased bias and reduced radius. This is due to the very different behavior of van der Waals and electrostatic forces as a function of distance (Foster, Rohl, and Shluger, 2000). In both cases, the macroscopic van der Waals force dominates the interaction, and the long-range electrostatic force due to bias is insignificant. The latter is consistent with the fact that fitting was made to curves obtained under conditions in which electrostatic forces had been minimized by the applied bias voltage. In real experiments, it is very unlikely that an originally sharp tip (about 10 nm) could be blunted so severely that the radius increased by a factor of 50. This probably indicates that the macroscopic model is not sophisticated enough, but insofar as it incorporates the experimental force vs distance behavior it is satisfactory for the simulation.

b. Simulating scanning

A large number of high-quality atomically resolved experimental images have been produced with a blunt tip, and some of them are reported by Barth *et al.* (2001) and Foster, Barth, *et al.* (2001). Therefore theoretical images, as well, have been calculated using a macroscopic tip of radius 675 nm and an applied bias of 0.03 V. Real tips were unsputtered, covered by oxide, and likely to be contaminated by surface material. Since the force curves do not exhibit long-range electrostatic interaction, the tip and the surface in the image area are most probably neutral. Therefore the MgO cube could be a good model to represent the tip electrostatic potential. Another advantage of using this nanotip is that its inter-

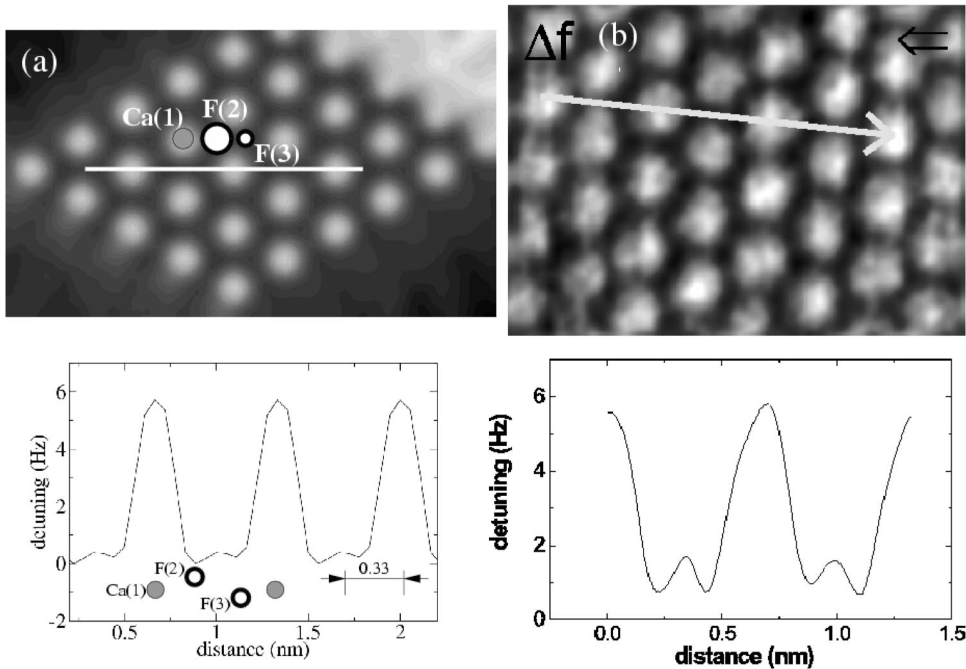

FIG. 14. Simulated images and scan lines: (a) produced using a tip with a negative electrostatic potential scanning at 0.35 nm; Ca(1), the calcium layer; F(2) the outermost fluorine layer; F(3) the lower fluorine layer; (b) example experimental image and scan line demonstrating "disklike" contrast. The white lines in the images are along the $[\bar{2}11]$ direction and indicate the position of the scan lines. Reprinted with permission (Foster *et al.*, 2002).

action with the ionic CaF_2 (111) surface can be well described within the atomistic simulation model.

The setup of the calculations is the same as in Fig. 5, with the cubic surface replaced by the CaF_2 (111) surface unit cell (shown in Fig. 12). The microscopic force is calculated using a periodic static atomistic simulation technique and the MARVIN2 code. The parameters for the surface interactions were generated to match experimental bulk structural, elastic, and dielectric constants, and gave good agreement with *ab initio* surface relaxations (Barth *et al.*, 2001). Parameters for the interactions between the MgO tip and the CaF_2 surface are taken from Binks (1994) and Bush *et al.* (1994). MgO tip parameters are as discussed in Sec. IV.C.2. The bottom 2/3 of the nanotip and the top of the CaF_2 surface are relaxed explicitly. In terms of notations shown in Fig. 5, region I consists of the bottom of the MgO nanotip and the top three layers of the CaF_2 surface, and region II the remaining layers.

Since we do not know in advance the nature of the electrostatic potential of the tip in a given experiment, scanning is simulated using the MgO tip orientated with an oxygen and a magnesium at the lower apex, producing electrostatic potentials that are net negative and net positive, respectively. In both cases, a full surface map of the force field over the CaF_2 surface unit cell is calculated, beginning at a tip-surface height of 2 nm and approaching to almost 0 nm with respect to the position of the Ca sublattice. In the final stage, the oscillations of the cantilever are modeled, as described in Sec. IV.E, after introducing the macroscopic background forces to the total force. Note that, to match the experimental method, simulated images are calculated in "constant-height" mode so that an image is a plot of the change in frequency across the surface at a constant height. Experimental parameters are used in the simulation where possible: a cantilever amplitude of 23 nm, an eigenfrequency of 84 kHz, a spring constant of 6 N/m, and a mean frequency change of -155 Hz.

c. Standard images

Many of the experimentally observed images of the CaF_2 (111) surface exhibit disklike and triangular contrast patterns. The interpretation of these two characteristic patterns is discussed in this section. They have been seen in several separate experiments using different tips and thus can be considered as "standard" images. The other contrast patterns seen on this surface are associated with more short-range scanning and tip changes; these are discussed and explained in the next section. This distance will be referred to as tip height in further discussion. We shall first discuss the properties of simulated images at a single constant height and compare them directly with experiment. Note, however, that the interaction ranges strongly depend on the true microscopic tip in an experiment, and any references to distance can only be considered as rough estimates. The images discussed in this section were produced for a setup where the shortest distance between the oscillating tip and the surface was 0.35 nm. At this height the average simulated contrast matches the experimental average contrast, which is a good measure of comparable interaction strength.

Figure 14(a) shows a simulated image and scan line produced with a negative-electrostatic-potential tip at 0.35 nm. The image demonstrates a clear circular or "disklike" contrast with strongest brightness centered on the position of the Ca ions in the surface. The scan line shows that contrast is dominated by a large peak over the Ca ion, with a much smaller peak in between the high and low fluorine ions. The smaller peak is due to a minimum in repulsion between the tip and F^- ions; how-

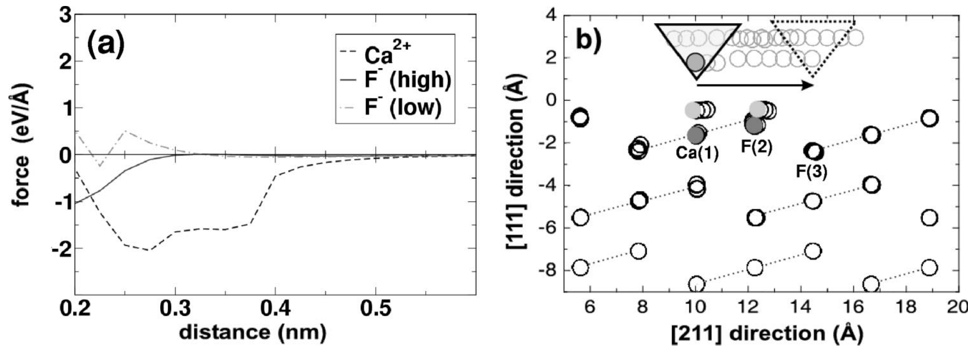

FIG. 15. Theoretical data from simulations with a negative electrostatic potential tip: (a) chemical force curves over the Ca, high and low F atomic sites; (b) full trajectories of atoms in a plane as the tip follows the $[\bar{2}11]$ scan line at a height of 0.350 nm. Ca(1), the calcium layer; F(2), the outermost fluorine layer; and F(3), the lower fluorine layer. The atoms shaded light gray in the surface indicate initial positions of the most relevant atoms when the tip is over Ca(1) (leftmost tip position in figure), whereas atoms shaded dark gray are final positions when the tip is over F(3) (rightmost position). Note that trajectories of only the bottom four atoms (one O^{2-} and three Mg^{2+} ions) of the tip have been included. Reprinted with permission (Foster *et al.*, 2002).

ever, this peak is so small in comparison to the main peak over Ca that it has no affect on the contrast pattern.

The predominance of Ca in the negative-potential tip contrast pattern has two components:

(i) The positive surface potential over the Ca^{2+} sites has a strong attractive interaction with the negative potential from the tip. Figure 15(a) shows clearly the domination of the attractive interaction over the Ca^{2+} ions.

(ii) As the tip approaches the surface, the Ca^{2+} ions displace towards it and the F^- ions are pushed into the surface. Figure 15(b) shows that, at 0.350 nm over the Ca(1) site, the Ca^{2+} ion displaces by 0.118 nm outwards, also forcing the high F^- ion outwards. However, as the tip moves towards the the F(2) site, the Ca^{2+} ion drops back to the surface and the high F^- ion is actually pushed in by 0.027 nm. The low F^- ions [F(3)] are not displaced significantly from their equilibrium positions at this scanning height. Displacement of ions from the surface greatly increases the range of the local surface electrostatic potential (Livshits *et al.*, 1999) and increases tip-surface interaction.

If we now compare simulated results with experimental results in Fig. 14(b), we immediately see a clear qualitative agreement. The experimental image shows disklike contrast, and the scan line has a very similar form to that in the simulation. However, we can extend the comparison to a quantitative level—the simulation predicts (based on surface geometry) that the smaller peak should appear at 0.33 nm from the main peak over the Ca sublattice. If we take over 70 experimental scan lines from images that show disklike contrast, we find that the average position of the small peak is 0.32 ± 0.05 nm, in excellent agreement with theory.

Figure 16(a) gives a simulated image and scan line when using a tip with a net positive electrostatic potential from the apex. The contrast pattern is now clearly triangular, with the center of brightness over the high F^- ions, but also with an extension of the contrast towards the position of the low F ions in three equivalent directions forming the triangle. The simulated scan line shows a large peak over the high F^- position dominating the contrast, but we also see a shoulder to this main peak over the position of the low F^- ion. Since this shoulder is a significant fraction of the height of the main peak, it can be seen in images and is responsible for the triangular contrast pattern. The triangular contrast pattern has three components:

(i) The negative surface potential over F^- sites gives a strong attractive interaction with the positive-potential tip [see Fig. 17(a)]. This interaction is comparable to the interaction of the negative tip over the Ca^{2+} ions, since although the F^- ions have half the charge of the Ca^{2+}, the high fluorine protrudes 0.08 nm further from the surface [see Fig. 17(b)].

(ii) The ions in both the F^- layers displace towards the tip as it approaches, and the Ca^{2+} ion is pushed inwards.

(iii) When the tip is over the low F^- ion, there is also some interaction of the tip with the next row of high F^- ions [see Fig. 17(d)]. Hence the shoulder has some component from this interaction, as well as the direct interaction with the low F^- sublattice. The role of displacements is discussed in detail in the next section.

Comparing these simulated patterns with the experimental results in Fig. 16(b), once more we see that there is a good qualitative agreement between experiment and theory. The experimental image shows triangular contrast, and the scan line shows large peaks with shoulders. Quantitatively we find that the average position of the shoulder with respect to the main peak in over 75 scan lines is 0.24 ± 0.04 nm, which compares very well with the theoretical prediction of 0.22 nm.

The described semiquantitative agreement of the experimental images with the theoretical images obtained with model tips supports the model of the ionic tip,

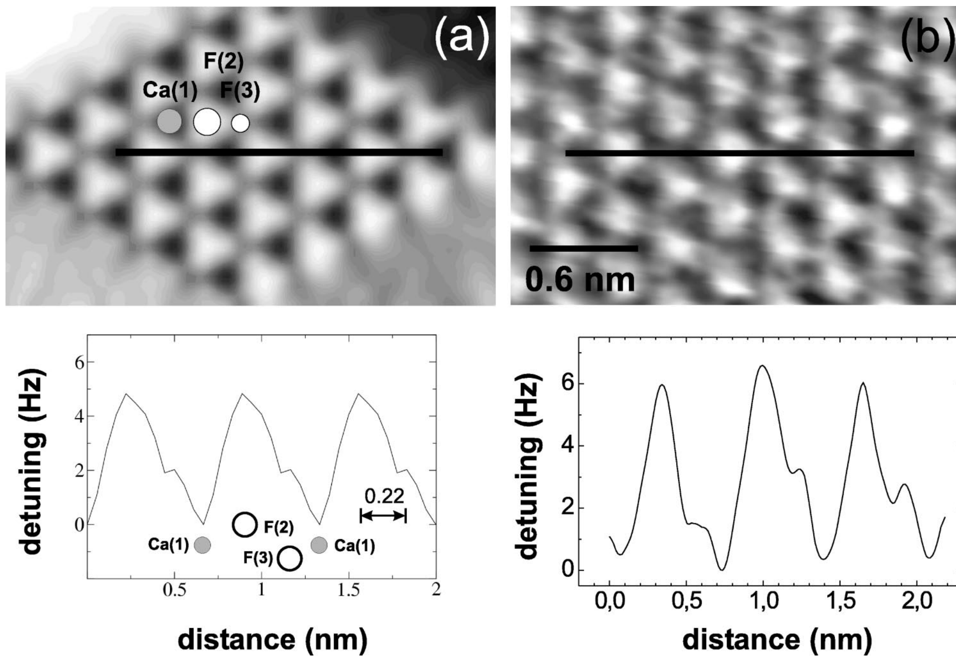

FIG. 16. Simulated and experimental images and scanlines. (a) Simulated image and scan line produced using a tip with a positive electrostatic potential scanning at 0.35 nm. Ca(1), the calcium layer; F(2), the outermost fluorine layer; F(3), the lower fluorine layer. (b) Example experimental image and scan line demonstrating triangular contrast. The white lines in the images are along the $[\bar{2}11]$ direction and indicate the position of the scan lines. Reprinted with permission (Foster *et al.*, 2002).

which may have two signs of the electrostatic potential probing the surface. Although the MgO tip is clearly an idealized model, it seems to capture correctly both the possibility of different types of tip contamination by the surface and ambient ions and the strength of the short-range chemical interaction.

d. Distance dependence of images

Since we have demonstrated both qualitative and quantitative agreement between experiment and theory at a certain height, it is interesting to see whether the comparison is still favorable when a range of heights is considered. Figures 18(a)–(c) show experimental images

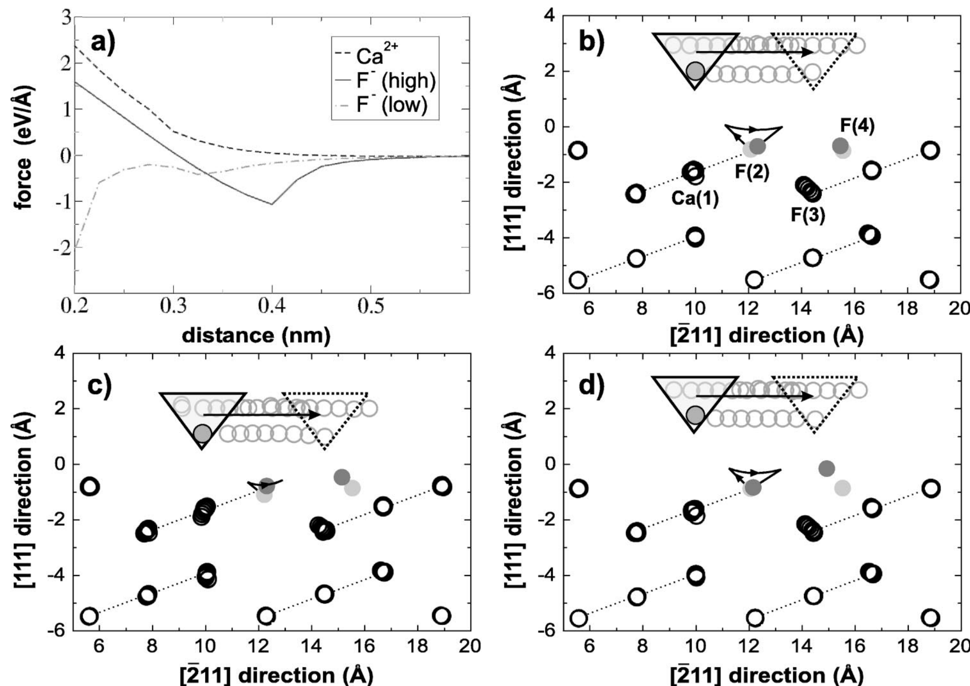

FIG. 17. Theoretical data from simulations with a positive electrostatic potential tip: (a) chemical force curves over the Ca, high and low F atomic sites; full trajectories of atoms in a plane as the tip follows the $[\bar{2}11]$ scan line. Tip-surface distance is (b) 0.350 nm; (c) 0.250 nm; (d) 0.325 nm. Ca(1), the calcium layer; F(2), the outermost fluorine layer; and F(3), the lower fluorine layer. The atoms shaded light gray indicate initial positions of the most relevant atoms when the tip is over Ca(1) (leftmost tip position in figure), whereas atoms shaded dark gray are final positions when the tip is over F(3) (rightmost position). F(4) is a high fluorine atom out of the plane, but its trajectory has been projected on to the same plane as the other atoms for clarity. Note that trajectories of only the bottom four atoms (one Mg^{2+} and three O^{2-} ions) of the tip have been included. Reprinted with permission (Foster *et al.*, 2002).

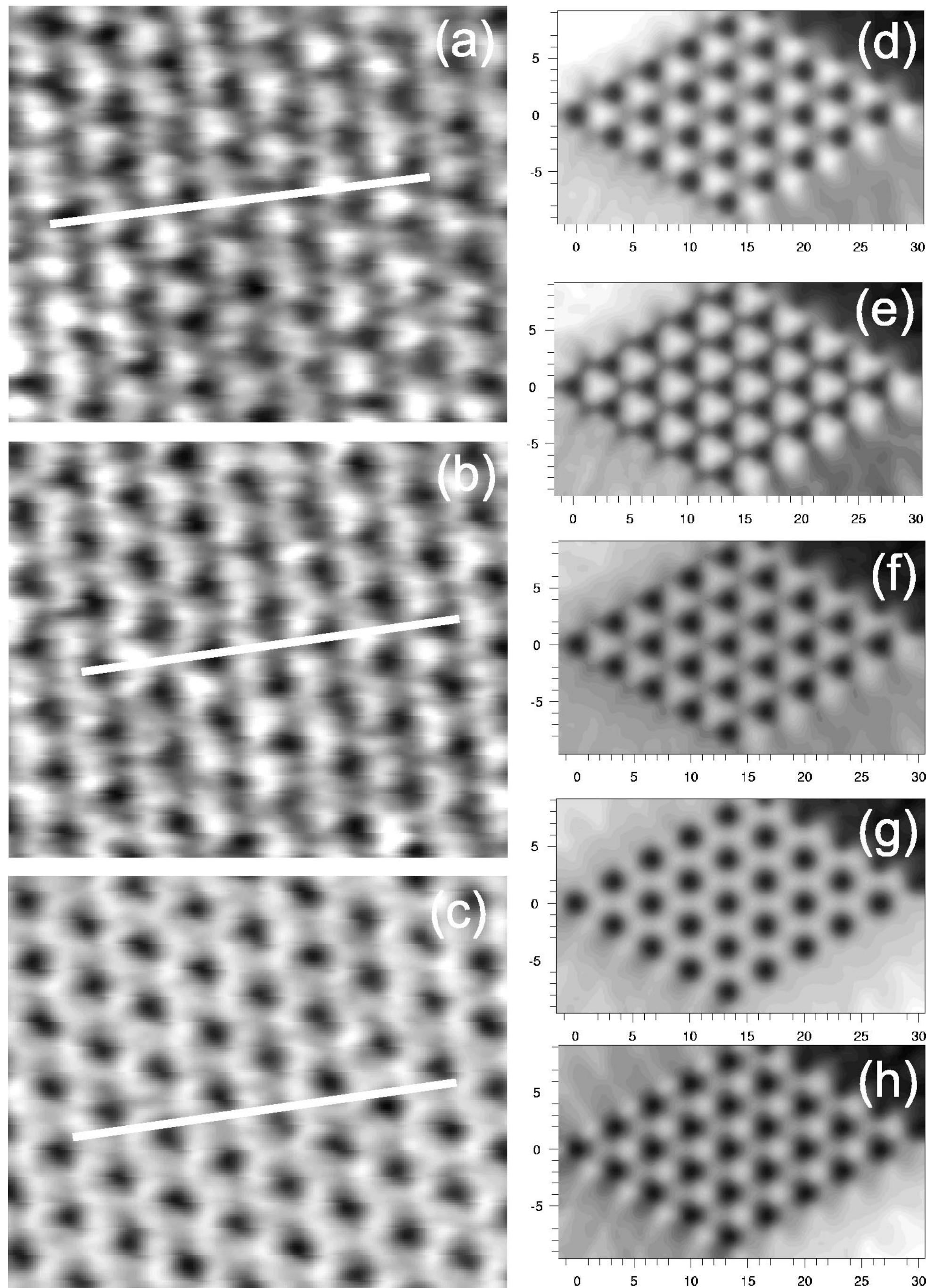

FIG. 18. Comparison of experimental and simulated images for a range of heights. (a)–(c) Experimental images taken as the tip approaches the surface (Barth *et al.*, 2001). (d)–(g) Simulated images at 0.500, 0.375, 0.325, 0.275, and 0.250 nm using a positive potential tip. Reprinted with permission (Foster *et al.*, 2002).

at increasing average frequency change, i.e., reduced tip-surface separation. Figures 18(a) and (b) clearly show the triangular contrast discussed above. Persistence of this pattern in experimental images obtained under different conditions shows that the triangular contrast pattern is not a unique feature seen only at a specific height, but is rather a distinct pattern related to the potential of the tip. However, in the image at closest approach we see that the contrast pattern has changed considerably. Figure 18(c) shows a honeycomb pattern, with the F sites now completely linked in bright contrast.

To understand whether this very distinct change in contrast could be explained within the same model as discussed in the previous section, further extensive modeling was performed. Figures 18(d)–(g) show the development of contrast in simulated images as the scanning height (i.e., the closest distance between the turning point of tip oscillations and the surface) is reduced. Figure 18(d) demonstrates that even at very large distances the triangular contrast pattern is consistent, though it is unlikely that experiments could measure such small chemical forces. As the tip approaches [Figs. 18(e) and

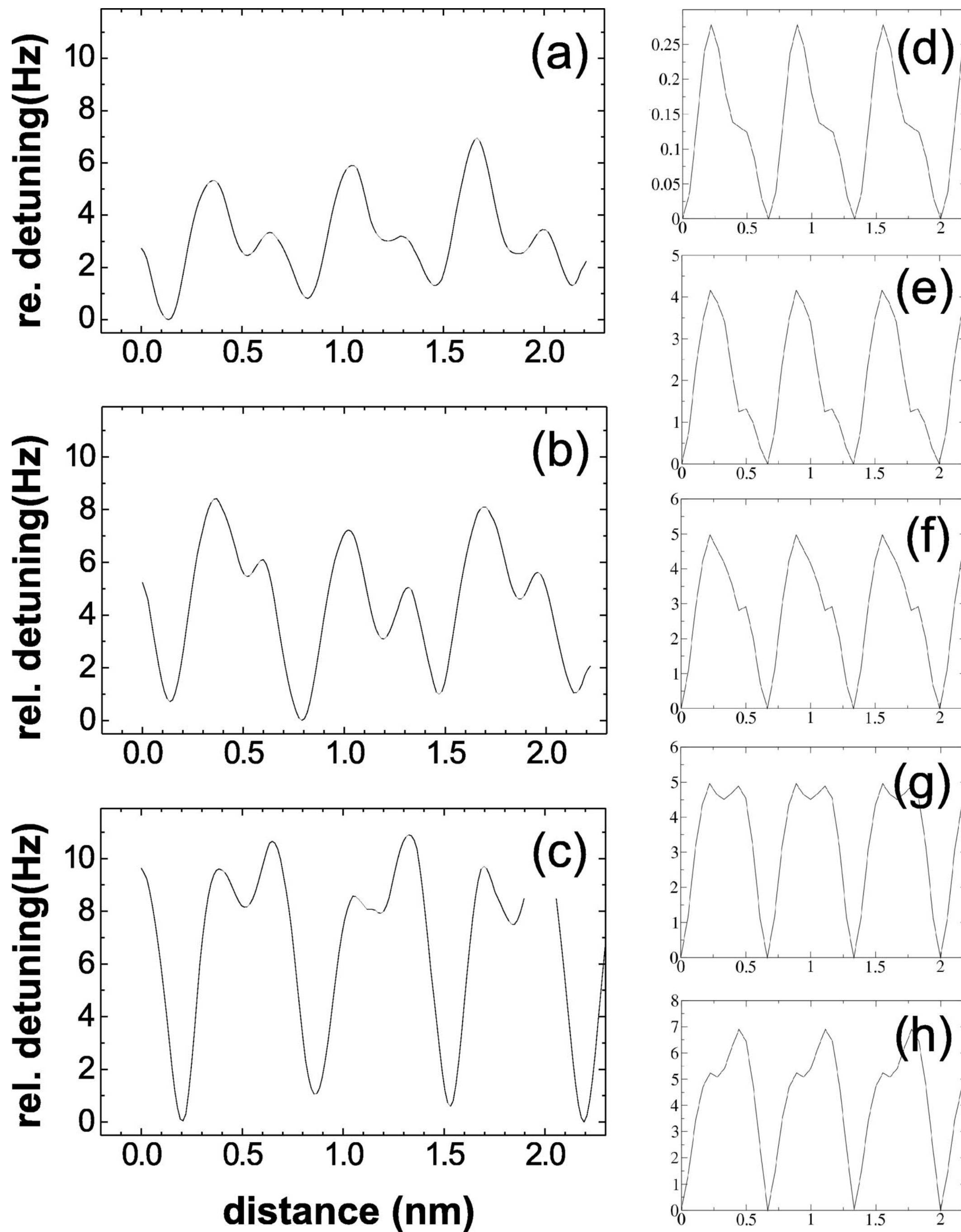

FIG. 19. Comparison of experimental and simulated scan lines for a range of heights. Comparison of (a)–(c) characteristic experimental and (d)–(h) simulated scan lines taken from the images in Fig. 18 as the tip approaches the surface. Reprinted with permission (Foster *et al.*, 2002).

(f)], theory predicts that the triangular pattern will become even more vivid, as seen in the experimental images. Finally, at 0.275- and 0.25-nm separations in Figs. 18(g) and (h), the simulated images develop the honeycomb contrast pattern seen clearly in the experimental image Fig. 18(c).

Further agreement can be seen by comparing the change in experimental and theoretical scan lines. Figures 19(a) and (b) show that at long range both experiment and theory demonstrate the large peak/small shoulder scan lines characteristic for the triangular contrast pattern. However, as the tip approaches closer, the magnitude of the shoulder increases, until for scan lines from the honeycomb images it is clear that the shoulder is at least equal to the original main peak.

A more thorough understanding of this agreement in contrast development requires studying in detail the changes in forces and atomic displacements as the tip approaches the surface. Figure 17(a) gives the chemical force over the relevant sites in the CaF_2 surface as a function of distance for a tip with positive termination. For distances larger than 0.400 nm, the curves are as one

would expect them to be, i.e., we find repulsion over the positive Ca^{2+} ion and attraction above the F^- ions. From the ionic interaction, we find some attraction over the low F^- ion and stronger attraction over the high F^- ion. Moving closer than 0.400 nm, we observe that the attraction over the high F^- ions reduces, while it increases over the low F^- site, until around 0.320 nm the greatest attraction is now over the low F^- site. This behavior can be understood by looking at atomic displacements as the tip approaches. At 0.350 nm there is strong displacement of the high F^- ion [F(2)] towards the tip [see Fig. 17(b)], producing a very strong attractive interaction. However, as the tip moves closer, this F^- ion is driven back into the surface and the force is reduced. Frame (c) shows that the high F^- ion has been pushed effectively back into its original lattice position at a tip-surface separation of 0.250 nm. However, when the tip is over the low F(3) site, we see very little movement of the closest high F^- ion, but in fact, aided by the proximity of the Ca^{2+} ion, there is a much smaller barrier for displacement of the high F^- ion from the next-nearest row [F(4)]. Frame (d) shows how the next-nearest high F^- ion very strongly displaces to the tip at 0.325 nm when it is over the F(3) site.

In summary, at a distance of 0.5 nm the interaction with the high F^- atom dominates, and we see only relatively small shoulders in scan lines over the low F^- sites. As the tip approaches, the nearest high F^- ion is pushed into the surface, reducing its dominance, and the interaction with low F^- and the next-nearest high F^- ion increases the relative size of the shoulder. This corresponds to increasing vividness of the triangular contrast pattern in images. Finally, the contribution from the high F^- is balanced by the contribution from the low F^-/next high F^- ion, and the main peaks and shoulders are equivalent in scan lines. It is this equivalence which produces the characteristic honeycomb contrast pattern.

These results alter the earlier perception (Livshits *et al.*, 1999; Barth *et al.*, 2001) that, due to adhesion of the surface ions to the tip, SFM tips should be prone to rapid changes during short-range scanning. It was expected that large displacements of the surface and tip ions might lead to instabilities of the SFM operation and to tip crashes. Although this effect certainly has been observed in many experiments (as discussed in more detail in the following section), it does not necessarily always result from large displacements and instabilities of the surface ions. As these results demonstrate, such effects can be reversible and may not disrupt imaging. The remarkable agreement between theory and experiment serves as an indirect but powerful indication that the displacements of the tip and surface ions (which cannot be imaged directly) play an extremely important role in contrast formation.

e. Ideal silicon tip

In this section, we extend the discussion to a nonionic tip, which is modeled by a pure silicon tip. On more reactive, semiconducting surfaces, it has been shown that for a pure silicon tip, contrast is dominated by the onset of bonding between dangling bonds in the tip and surface (Pérez *et al.*, 1997; Lantz *et al.*, 2000), and these forces have recently been explored in detail experimentally (Lantz *et al.*, 2001). However, for insulating surfaces, clean silicon tips have normally not been used in experiments published so far, although several attempts have been made (Allers *et al.*, 1999, 2001; Ashino *et al.*, 2001). Nevertheless, it is useful to calculate explicitly the interactions of a clean silicon tip with the CaF_2 surface.

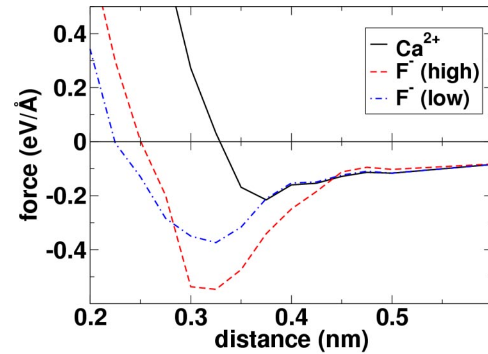

FIG. 20. (Color in online edition) Simulated force curves taken over the Ca, high and low F sites in the CaF_2 (111) surface with a pure silicon tip. Reprinted with permission (Foster *et al.*, 2002).

To represent a pure silicon tip, we use a ten-atom silicon cluster, with its base terminated by hydrogen. This was shown previously (Pérez *et al.*, 1998; Lantz *et al.*, 2000) to provide a good model of a clean silicon tip with a single dangling bond at the apex. The smaller size of the silicon cluster compared to the MgO cube allows us to use a correspondingly smaller surface size, and the crystal is here simulated by a cluster of $(4\times4\times3)$ CaF_2 units. The bottom two layers of the tip and the top two layers of the surface are allowed to relax with respect to atomic forces, as in the previous simulations.

Figure 20 shows calculated tip-surface forces as the silicon tip approaches the Ca^{2+}, high F^-, and low F^- sublattices in the CaF_2 surface. It is clear that contrast in images with a silicon tip should be dominated by interaction with the high F^- sublattice, and to a lesser extent the low F^- sublattice. The interaction with Ca^{2+} is much weaker and enters repulsion at larger tip height (about 0.33 nm) than over the F^- sites (about 0.25 nm). The interaction between the tip and the F^- ions is due to the onset of covalent bonding between Si and F^-, involving charge transfer from the F^- ions into bonding states. At 0.3-nm tip height, charge transfer is 0.18e for the high F^-, but only 0.02e for the low F^- [based on Mulliken population analysis (Mulliken, 1949)]. Over Ca, there is no charge transfer until small heights (about 0.3 nm), where charge is actually transferred from the neighboring high F^- site to the tip. However, at this point the tip has already entered the repulsive interaction region and the effect is negligible.

If we now compare the silicon tip force curves with those in Fig. 17(a) we see qualitatively the same behavior in the range between 0.300 and 0.500 nm: very weak

interaction beyond 0.450 nm; largest interaction over high F^-; weakest interaction over Ca^{2+}; and low F^- somewhere between. Note that the onset of repulsion over the Ca^{2+} site even occurs at qualitatively the same position as in Fig. 17(a), at the maximum in attraction over the high F^- site. This agreement implies that a pure silicon tip could only produce a triangular contrast pattern, as for the positive potential ionic tip, at medium to long range. At smaller ranges, the differences in force for the ionic tip are due to the strong displacements induced by tip approach, in agreement with experiment (see previous section). Note that, for the silicon tip, interaction forces are considerably smaller than for the ionic tip and, therefore, displacements for a pure silicon tip are much smaller. Over the Ca^{2+} ions, there is almost no surface ion displacement until very small tip-surface separations when the Ca^{2+} directly underneath the tip is pushed in. Over the high F^-, at 0.350 nm the F^- ion under the tip is at a maximum displacement of 0.040 nm towards the tip, before being pushed back in. There is no significant displacement of the low F^- or any atoms not directly underneath the tip. Due to the softness of the silicon tip in comparison to the ionic MgO tip, tip atom relaxations play a more significant role in the interaction. Over the high F^- there is no significant displacement of the apex Si atom towards the surface, but at 0.300-nm tip height it is displaced by 0.025 nm into the tip due to strong repulsion from the proximity of the F^-. Over the Ca^{2+} ion a similar process occurs, but the tip apex displacement at the same height is only 0.010 nm. These tip atom relaxations slightly reduce the overall tip-surface interaction, but would have no significant influence on images due to their short range and small magnitude. However, it is possible that for other, even softer, tips, this contribution could be significant in contrast patterns.

Comparing the magnitude of force curves for the two different tips, we see immediately that the force between a pure silicon tip and the CaF_2 surface is much less than for a positive-potential ionic tip. On first sight, one might expect a strong interaction between Si and F, as F is known as a very reactive species. However, in this case we are effectively dealing with F^- ions with a full outer shell, not atoms, and there is no possibility of the large charge transfer characteristic of Si and F interacting in atomic form. If we calculate the maximum possible contrast for a pure silicon tip imaging CaF_2, it is about 2 Hz—several times smaller than that seen for simulations with an ionic tip, and, more significantly, in experiments. This is a consequence of both the weaker attraction to the F^- ions and the lack of medium-range repulsion over Ca^{2+} ions, reducing the overall contrast.

2. $CaCO_3(10\bar{1}4)$ surface

Calcite ($CaCO_3$) is an ionic compound with relevance in nature and technology. It is well known for its strong birefringence, which has been exploited in a variety of optical applications, but it is also a mineral found in nature in great abundance, and a most interesting substrate for biomimetic materials chemistry (Heywood, 1996). The $CaCO_3(10\bar{4}1)$ surface is the most stable cleavage face (de Leeuw and Parker, 1997) and has been the subject of a variety of theoretical (Skinner *et al.*, 1994) and experimental (Stipp and Hochella, 1991; Stipp, 1999) studies, including contact force microscopy (Hillner *et al.*, 1992; Ohnesorge and Binnig, 1993; Stipp *et al.*, 1994; Liang *et al.*, 1996). In these studies it has been claimed that atomic resolution can be obtained by performing the measurement in an aqueous environment where a snap into contact is avoided by compensating attractive van der Waals forces by capillary forces acting on the tip apex. However, interpretation of images under such conditions is difficult, and to date there is no theory that could confirm this in detail. In the context of understanding contrast formation in dynamic force microscopy, this surface is most interesting, since it is a very-low-symmetry ionic system, in which one ionic species is a covalently bound group, namely, $CO_3{}^{2-}$. The main features of the $(10\bar{4}1)$ surface are depicted in Fig. 21. The surface unit cell is composed of two Ca^{2+} ions and two $CO_3{}^{2-}$ groups in which the calcium ions define a surface parallel plane that also contains carbon atoms. Only one oxygen atom of each $CO_3{}^{2-}$ group shares this plane, while the others are located about 0.06 nm above and below. The $CO_3{}^{2-}$ groups appear in two different orientations with respect to a rotation around an axis perpendicular to the surface plane; therefore neighboring rows of groups along the [010] direction are not equivalent, while the most protruding oxygen atoms form a zigzag structure oriented along the $[\bar{4}\bar{2}1]$ direction.

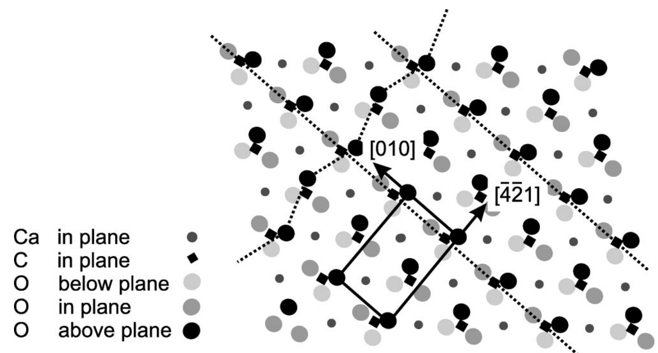

FIG. 21. Schematic representation of the CaCO3$(10\bar{4}1)$ surface.

Intuitively, one would expect that all these surface features should be represented in atomically resolved force images. In fact, a major issue of this study was establishing which sublattice would dominate image contrast and hence whether force microscopy would be able to resolve individual oxygen atoms within the covalent group or whether this group would appear as a single feature. Previous attempts to image this and similar minerals did not resolve all chemical species (Shindo and Nozoye, 1992; Ohnesorge and Binnig, 1993; Stipp, 1999).

Simulations on calcite were performed in the same way as described in Sec. V.C.1 for CaF_2. The setup is the

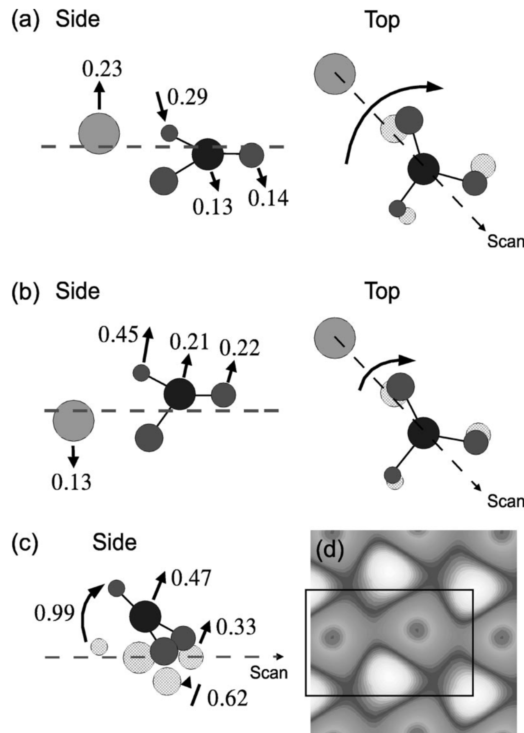

FIG. 22. Schematic diagrams of atomic displacements of the calcite $(10\bar{1}4)$ surface as the tip scans across at 0.425 nm [(a) and (b)]. The numbers are in Å, and show the displacements when the tip is directly over that atom. Dark gray, C atoms; light gray, Ca atoms; and medium gray, O atoms. The size of the oxygen atoms in the carbonate group is in perspective, i.e., the larger the atom the further "out" of the page it lies. The cross-hatched atoms in some drawings show the undisplaced position of the atoms when the tip is not in proximity, and the arrows give an indication of the displacement direction as the tip approaches. (a) Scanning with a negative potential tip. (b) Scanning with a positive potential tip. (c) Scanning at 0.4 nm from the surface with a positive potential tip causes the whole carbonate group to flip up from the surface. (d) Density-functional theory (DFT) calculated electrostatic potential at 0.250 nm above the calcite surface in a plane parallel to C, Ca, and middle O atoms in the surface. The black rectangle is the unit cell of the $(10\bar{1}4)$ calcite surface.

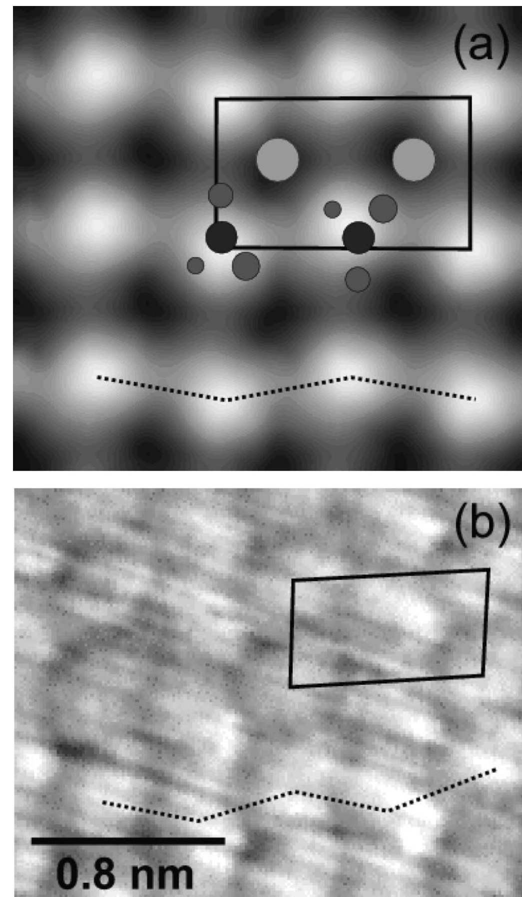

FIG. 23. Images of a calcite surface: (a) simulated image of calcite produced using a tip with a positive net electrostatic potential, dark gray, C atoms; light gray, Ca atoms; medium gray, O atoms; (b) experimental image of calcite.

same as in Fig. 5, but now the surface is a 4×4×3 extension of the side section shown in Fig. 22(a). The top two layers of the surface and the bottom of the nanotip are allowed to relax in the simulations. Interaction parameters for the tip are the same as previously, and calcite parameters are taken from Pavese *et al.* (1996). The oscillations of the cantilever are simulated with an amplitude of 67 nm and a frequency of 77 kHz, as in experiments. The tip radius of 30 nm is fitted to experimental force vs distance curves over calcite.

The complex displacements of atoms in the calcite surface play an important role in contrast formation and strongly affect tip-surface interaction. Scanning with a negative potential tip at 0.425 nm produces a combination of rotation/displacement of the carbonate group and displacement of the Ca^{2+} ion as shown in Fig. 22(a). The Ca^{2+} has a simple displacement out of the surface as the tip passes, but the carbonate group also rotates as it is pushed into the surface. This combination reduces the influence of the orientation of the carbonate group on images, and the position of the Ca^{2+} ion dominates contrast in images produced with a negative-potential tip. For a positive tip [see Fig. 22(b)] the Ca^{2+} ion is pushed into the surface, and the whole carbonate group is strongly displaced out with a slight rotation. The very large displacement of the highest oxygen of the carbonate (0.045 nm) causes a very strong interaction with the tip, and its position dominates contrast in images with a positive-potential tip. Figure 23(a) shows a simulated image produced using a tip with a net positive potential, with the protruding oxygen sites connected by lines. The clear zigzag contrast pattern can be characterized by an angle of 13° from the vertical and possibly used as a basis for interpretation of experimental images. Figure 22(c) shows the displacements of the calcite surface when scanning with a positive-potential tip at 0.4 nm. At this closer separation, the whole carbonate group at first displaces out from the surface considerably, and then actually flips up, pivoting on the middle oxygen atom. This kind of displacement causes extreme changes in the force and is likely to strongly influence the contrast pattern.

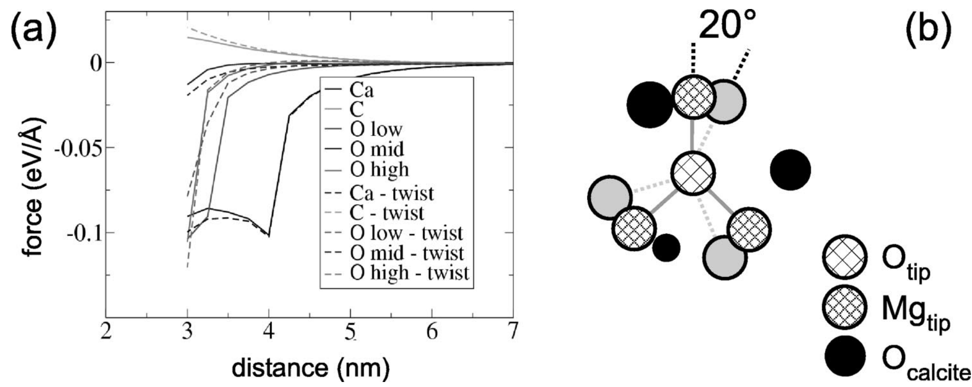

FIG. 24. Effects of tip rotation. (a) Comparison of the force as a function of tip-surface separation between a normal tip and a tip rotated by 20° around the z axis. The curves are taken over the various sublattices in the calcite surface, curves labeled "twist" in the legend are produced with a rotated tip. (b) Schematic showing how the orientation of the projection of the end of the MgO tip on the carbonate group changes when rotated.

Thus modeling of the image contrast with the atomically sharp MgO cube tip clearly suggests that, although the image contrast is caused predominantly by electrostatic forces, the carbonate groups should be imaged as a whole in an NC-SFM. To illustrate further the nature of contrast on calcite, Fig. 22(d) shows the electrostatic potential calculated in a plane parallel to a plane through C, Ca, and middle O atoms of the surface, and at a height of 0.250 nm from the surface. This corresponds to an effectively infinitely sharp tip. One can see that, even from this very close view, the individual oxygen ions of the CO_3^{2-} group cannot be clearly distinguished in the electrostatic potential probed. This suggests that the nature of chemical bonding rather than the tip size plays the decisive role in determining whether individual atoms can be resolved inside a molecular group such as carbonate.

Figure 23(b) shows one of the experimental images of the $CaCO_3(10\bar{4}1)$ surface. All ionic rows are present and one can see the expected zigzag pattern, which we regard as a piece of evidence that the surface features imaged are CO_3^{2-} groups and not calcium ions. The carbon and oxygen atoms are not resolved, as predicted by the theory. It is intuitively clear that, on the low-symmetry $CaCO_3(10\bar{1}4)$ surface, the details of nuclear movement depend on the orientation of the nanotip with respect to carbonate groups in a nontrivial way. This is illustrated in Fig. 24(b) showing the projection of the last oxygen and three magnesium ions of the tip on the carbonate group of the surface. The MgO cube is orientated by its (111) axis perpendicular to the surface (see Fig. 5) as in all previous calculations. Rotation of the tip by 20° degrees with respect to this axis changes the projection as shown in Fig. 24(b). This relatively small rotation of the tip leads to a distinct difference of the interaction with the surface, as evident in Fig. 24(a) where the corresponding interaction curves are labeled as twisted. These considerations suggest that the effect can be much stronger for more complex tip structures. It is most pronounced at relatively short distances of 0.3 nm and closer to the surface. We did not attempt to simulate the surface scanning with the rotated tip, but it is clear from the previous discussion that the surface deformation will also be different for different tip orientations. The image should be most significantly influenced at closest tip-surface separation. This demonstrates the complexity of processes involved in dynamic mode force scanning in the presence of strong surface relaxation.

D. Thin insulating films

1. NaCl trilayer on Al(111) surface

Only a very few facets of the ionic NaCl crystal are stable, in particular the (001) face. This is due to the arrangement of Na^+ and Cl^- ions, which makes such a facet electrically neutral. A (111) facet of the same crystal consists of only one sort of ion. Such a polar surface is unstable due to its high surface energy: this facet does not occur in nature. It came therefore as a surprise when NaCl(111) trilayers on Al(111) were detected in STM images. The atomically resolved images left no doubt that the triangular-shaped islands exhibit a lattice with sixfold symmetry, and a lattice constant corresponding to bulk NaCl (Hebenstreit *et al.*, 1999). The puzzle was resolved by first-principles calculation of the electronic structure, which revealed that the Fermi level of the NaCl trilayer is situated in the middle of the Na 3*s* band. Therefore both Na-atoms of the Na-Cl-Na compound possess 0.5*e* effective charge. In this case the NaCl(111) trilayer is neutral and therefore stable.

2. MgO thin films on Ag(001) surface

It is technologically important to know the thickness limit for insulating films to remain as insulators. This property is essentially given by the band gap of the insulator's electronic structure. A system of 1–3 monolayers of MgO on Ag(001) was studied by scanning tunneling microscopy and scanning tunneling spectroscopy. The images of MgO islands of a single monolayer revealed the underlying atomic structure of the Ag surface (at 30 mV and 2 pA; Schintke *et al.*, 2001). This feature indicates that one monolayer of MgO is not sufficient to

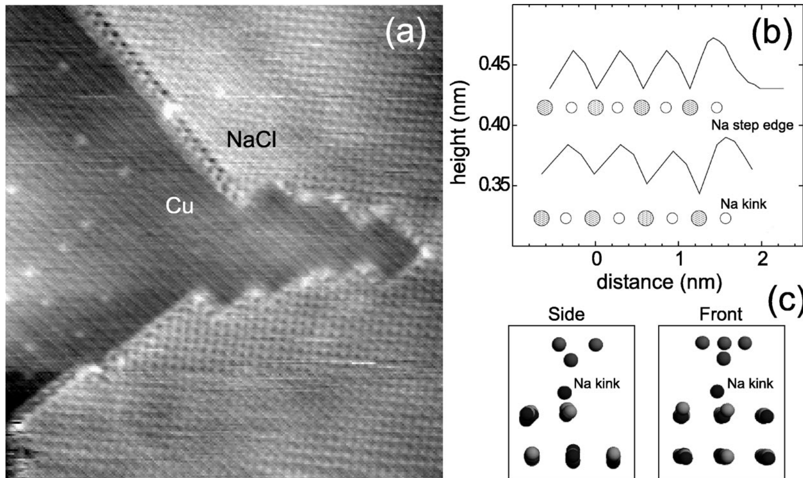

FIG. 25. Effects of kink sites. (a) Experimental image of NaCl thin film on Cu demonstrating increased contrast at step-edge and kink sites. (b) Simulated scan lines over Na and Cl kink sites in a NaCl thin film. (c) Atomic snapshots from the simulation as the tip passes the kink site. Reprinted with permission (Bennewitz *et al.*, 2000).

sustain the insulating properties of the crystal. However, the very low current indicates that the transport of electrons from the tip into the sample is already substantially impeded by the MgO layer.

The transition from a single monolayer to a bilayer and a trilayer cannot be analyzed by scanning tunneling microscopy, because the conductance in the low-voltage regime becomes too low for images with atomic resolution. Therefore it was analyzed by a combination of scanning tunneling spectroscopy and electronic structure calculations, in particular, study of the local density of states with increasing surface coverage. As it turned out, three layers of MgO on the Ag surface are sufficient to completely screen the electronic structure of the metal. The electronic structure at the surface of the trilayer in this case is already equal to the electronic structure at the surface of an MgO crystal.

3. NaCl thin films on Cu(111) surface

Recent scanning tunneling microscopy studies of thin insulating films grown on conducting substrates (Glöckler *et al.*, 1996; Hebenstreit *et al.*, 1999; Fölsch *et al.*, 2000) have motivated NC-SFM studies of similar surfaces. Specifically, high-quality atomic resolution was achieved on NaCl (001) films on copper substrates (Bennewitz *et al.*, 1999a, 2000). Growth modes, orientation, and lattice constants of ultrathin films were revealed (Bennewitz *et al.*, 1999b), and atomic resolution at step edges was demonstrated (Bennewitz *et al.*, 1999a). Also, the prevalence of low-coordinated sites, such as steps, corners, and kinks on these thin films makes them of special interest for catalytic studies, and NC-SFM offers the possibility of imaging these features in atomic resolution.

Figure 25(a) clearly demonstrates atomic resolution on the terrace and increased contrast at edges and kink sites of the NaCl island grown on the copper (111) surface (Bennewitz *et al.*, 1999a, 2000). The nature of the enhanced contrast at edges and kink sites has been explained using an atomistic simulation (see Bennewitz *et al.*, 2000). For the edge, the enhanced contrast is much more localized directly over the edge ion, whereas a change from standard terrace contrast can be seen several rows from the kink site. This effect is due to the low coordination of the edge and kink ions, which has two effects: (i) the electrostatic potential over the low-coordination sites extends much farther than over the ideal terrace (Livshits *et al.*, 1999); and (ii) the low coordination of the ions increases their displacements due to the interaction with the tip. For a tip scanning the surface at 0.45 nm over the terrace, Na ions are displaced by 0.014 nm, but this increases to 0.024 nm for Na ions at the step edge and 0.025 nm at the kink. However, the extremely low coordination at the kink site means that even the nearest Na neighbor to the kink ion is also displaced by 0.018 nm, producing a stronger and more extended increase in contrast.

These results directly confirm the importance of the electrostatic interaction and ionic displacements for contrast formation on ionic surfaces. They suggest that even stronger contrast could be observed for charged defects, such as impurities, adsorbed ions, and vacancies. However, the low concentration and high mobility of vacancies and some adsorbed species prevent their observation by an NC-SFM. Stable aggregates of several divacancies have recently been observed on the KBr surface (Bennewitz *et al.*, 2001). Atom-size impurities have been observed on the CaF_2 (111) surface after surface chemical reactions (Reichling and Barth, 1999). However, to image and establish the identity of individual surface defects and study their properties has proved extremely challenging.

VI. STUDYING SURFACE PROPERTIES

Some of the most captivating research emerging in recent years deals with fundamental physical processes and how they can be influenced by the tip-surface interaction. This concerns, for example, phonon excitations of substrates and adsorbates by injection of electrons, surface magnetism, targeted excitations of spin rotations, or electron interactions during ballistic transport in solids.

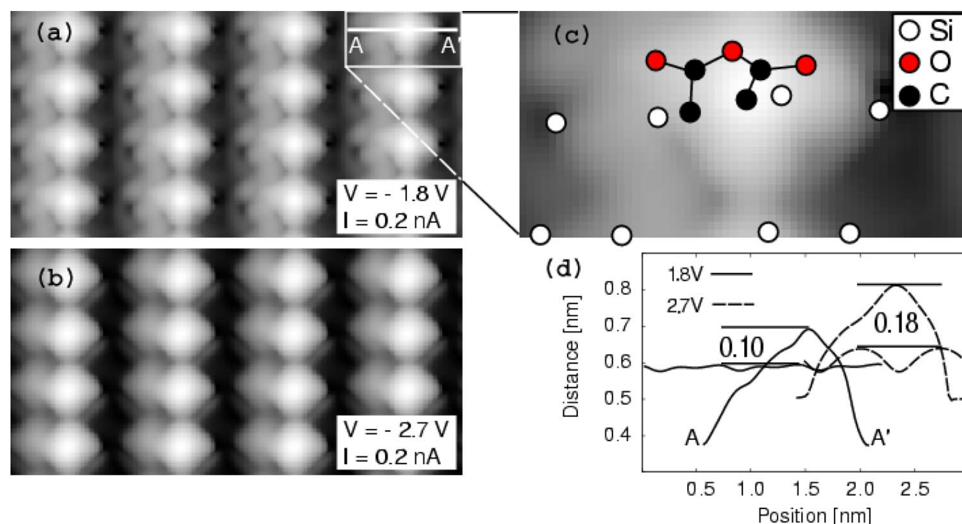

FIG. 26. (Color in online edition) Simulated STM images and line scans of maleic anhydride on Si(100) for two different bias voltages, −1.8 and −2.7 V, respectively. (a) Simulation of the current contour for 1.8 V and 0.2 nA; the molecule is seen as a distinct protrusion. Due to the size of the molecule simulated current contours on adjacent cells overlap. (b) Simulation of the current contour for 2.7 V and 0.2 nA, the qualitative features of the image remain unchanged. (c) Enlarged unit cell with the position of the molecule. (d) Simulated line scan across the molecule. The apparent height changes by 0.8 Å if the bias voltage is increased from −1.8 to −2.7 V. Reprinted with permission (Hofer *et al.*, 2002).

A. Adsorbates on surfaces

Adsorption on surfaces has been studied with different methods since well before the invention of SPM's (Zangwill, 1988). However, due to the real-space image of SPM's and their potential for studying the processes in real time, analytical methods become more and more focused on this instrument. In this context it is interesting to determine what an SPM can tell us about the changes electron orbitals undergo during adsorption processes.

1. $C_4O_3H_2$ on Si(100) (2×1) surface

The question as to whether the STM can in fact resolve single-electron states or even the lateral extension of single-electron wave functions is an intriguing puzzle and, until very recently, the answer seemed to be no. Experimentally, the resolution of electron wave functions by scanning tunneling microscopy has already been demonstrated (Lemsay *et al.*, 2001). Here, we review a case in which only the conjunction of experiment and theory leads to the same conclusion.

The model system consists of maleic anhydride ($C_4O_3H_2$) molecules on a Si(100) surface (Hofer *et al.*, 2002). The Si(100) surface reconstructs in a characteristic (2×1) row of silicon dimers (Hofer, Fisher, Wolkow, and Grütter, 2001), which is very well researched due to its relevance for the fabrication of microchips (Wolkow, 1999). Therefore the STM images of the adsorbed molecules (Bitzer *et al.*, 2001), depicting the adsorption site between adjacent dimer rows, contain no ambiguity. Experimentally, the main results were (i) a ground-state adsorption between dimer rows; and (ii) an apparent height of the molecule 0.7 Å (bias voltage −1.8 V), and 1.2 Å (bias voltage −2.7 V).

The surface was initially mimicked by a Si(100) (2×2) eight-layer film. During the surface simulations it became clear that the size of the system was too small—adjacent molecules on the surface exert a very high strain on the lattice, which leads to the rupture of a Si-dimer bond. Energetically, this process is very unfavorable. Consequently, simulations were repeated with a (4×2) unit cell. In this case the molecule occupied only every second interdimer position and the strain on the lattice and the Si-dimer bonds was substantially reduced. It was found that for a coverage of 1/8 (molecule per dimer) the interdimer site was energetically favored, contrary to a chemist's intuition and many examples, where molecules on this surface react via a $[2+2]$ cycloaddition (Hofer *et al.*, 2002). In other words, they adsorb on top of a silicon dimer. The STM images, recorded with a tunneling current of 0.5 nA, were simulated by assuming that the structure of the microtip in the apex was akin to a tungsten pyramid in (100) orientation. The simulated STM images and line scans are displayed in Fig. 26. Clearly, if the bias potential is increased by 0.9 V, the apparent height of the molecule on the surface changes by about 0.8 Å. The simulated results agree well with the experimental ones, since the difference in experiments is 0.5 Å. To understand the difference, it was necessary to analyze the electronic structure of the molecule and the silicon surface. The density of states of the surface-adsorbate system shows three distinct peaks at −0.6 (1), −1.8 (2), and −2.4 eV (3). Plotting the charge density of these states, it was found that only two of them, (1) and (3), protrude into the vacuum above the molecule. Since the tunneling probability depends on the overlap of wave functions between sample and tip, a high local density of states in the vacuum above the molecular position indicates a

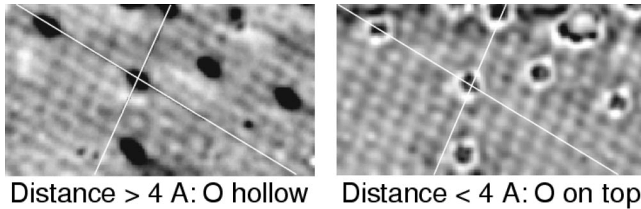

FIG. 27. STM images of Fe(100) with an adsorbed oxygen atom. Oxygen appears to be adsorbed at the hollow site of the surface for distances above 4 Å (correct), but it appears to be at the on-top site for distances below 4 Å (incorrect). The conclusion from the experiments is a reversal of surface corrugation in the low distance regime. Reprinted with permission (Hofer, Redinger, *et al.*, 2000).

high contribution to the tunneling current from this state. It turned out that the most significant contribution to the increase of the apparent height due to the increased bias potential is due to only one state (3) of the molecule. The increase of the bias potential from 1.8 to 2.7 V is therefore in effect a tuning in on the energy range of a single molecular orbital.

2. O on Fe(100) surface

The question of how the electric field of the STM tip affects the vacuum barrier of the surface electronic structure, and thus the decay length of the tunneling current, has been widely discussed since the invention of the STM (see previous sections). In particular, the role of image forces, which should lead to a lowering of the potential barrier, remained unclear (Binnig *et al.*, 1984; Lang, 1988). Related to this problem is the question of when a perturbation approach to tunneling becomes insufficient. In general, the regime of field interactions is not accessible to STM experiments, as will be seen. However, by measuring a three-dimensional map of currents on an Fe(100) surface in such a way that the tip position is adjusted manually by a change of the piezovoltage, the transition from the tunneling regime to point contact can be studied experimentally (Hofer, Redinger, *et al.*, 2000). From the 3D current map the corrugations can be extracted in a straightforward manner. In addition, the apparent height of atoms can be determined by, for example, adsorbing oxygen onto a surface. Since the position of the adsorbant is known [e.g., for oxygen on Fe(100) the preferred site is the fourfold hollow site], its position with respect to the maxima and minima of the constant current contour can be determined. The measurements revealed the following behavior:

(i) the positions of the Fe atoms on the surface are imaged as protrusions for $z \geqslant 0.4$ nm;
(ii) these positions are imaged as depressions if $z \leqslant 0.4$ nm (see Fig. 27);
(iii) the corrugation height is in all cases very small and below 0.002 nm; and
(iv) the 3D current maps were generally obtained with a stable tip and in one single sweep.

The absolute distance in the experiments was determined by extrapolating the currents from two separate point measurements to the point of contact, defined by a conductance of $2e^2/h$, the conductance quantum.

The measurement with a stable tip suggested that the tip was not contaminated. For this reason the STM tip chosen in the simulations was a clean tungsten tip. Since the surface orientation at the apex of the polycrystal is *a priori* unknown, simulations were performed with all three low-index surfaces, (100), (110), and (111). The surface electronic structure of sample and tip were calculated with a full-potential DFT code (Hofer, Redinger, *et al.*, 2000), with the surfaces represented by freestanding films in a vacuum. The results were also checked with an Fe-terminated tungsten tip, but in this case agreement was not obtained between experiments and simulations. Therefore this tip model was ultimately excluded.

The current was calculated for nine positions of the STM tip on the Fe(100) surface: the top site, the bridge sites, and the hollow sites. From the distance-dependent current curves the corrugation amplitudes were extracted. The results of the calculations are shown in Fig. 28(a). The first conclusion to be drawn from the simulations is therefore that the tip most likely used in the experiments was a clean tungsten tip. The positive cor-

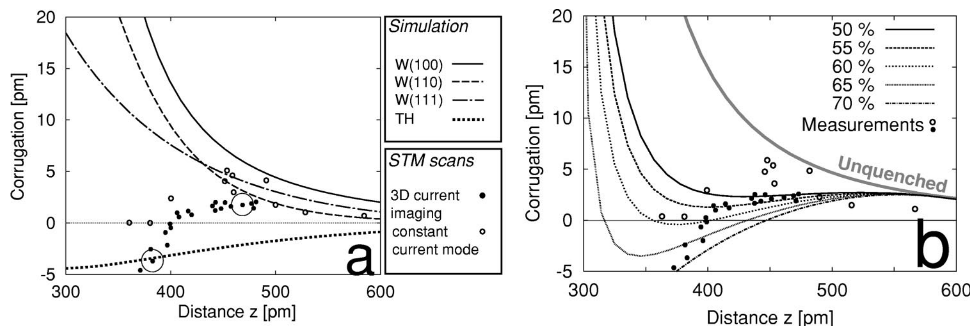

FIG. 28. Simulated corrugation of Fe(100) surface: (a) with three different tungsten tips, as well as a model tip of radial symmetry (Tersoff-Hamann model), and (b) simulation of scans of the same surface if the surface states are quenched due to the STM tip potentials. The quenching of surface states due to the tip in the very close distance regime leads to a corrugation reversal, which is actually observed in the experiments. Reprinted with permission (Hofer, Redinger, *et al.*, 2000).

rugation on an anticorrugated surface in this case arises from the high contribution of d_{xz} and d_{yz} states in the electronic structure of the tip. This, in itself, is one more confirmation that the electronic structure of tungsten tips is not accurately described by a single orbital of d_{z^2} symmetry (Chen, 1990a, 1990b).

While the simulation agrees well with the experimental results in the distance range above 0.4 nm, it does not agree at all in the distance regime below 0.4 nm. Experimentally, the positions of the Fe atoms are imaged as depressions, whereas in simulations they appear as protrusions. The reason for this obvious disagreement can only be that the tip interacts with the surface. Neglecting the effects of chemical forces, since they generally lead to a corrugation enhancement and thus would further increase positive corrugation, the only possibility is that the field of the tip influences the surface electronic structure. This effect can be simulated by an applied bias potential on the Fe(100) surface. On Fe(100) a substantial contribution to the tunneling current originates in a surface state near the $\bar{\Gamma}$ point of the Brillouin zone (Stroscio *et al.*, 1995). Surface states are generally an expression of the boundary conditions at the vacuum boundary of a crystal. Their existence thus depends on the existence of this boundary. If a tip approaches the surface then the tip potential will gradually lower the vacuum potential barrier. The surface layer gradually loses its surface characteristics; this leads to the loss of surface states. In principle, such a behavior can be simulated by a distance-dependent quenching of the surface-state density. Since surface states on Fe(100) are states in the minority spin band, we have simulated the quenching by reducing the contributions from the minority band during an approach. Numerically, this was done by a polynomial of second order. The results are shown in Fig. 28(b). The percentage describes what part of the minority-states density was quenched in the simulation for a distance of 0.3 nm. Comparing experiments with simulations we see that a quenching of about 50–70 % is sufficient to reproduce the measurements.

B. Point defects

As discussed previously, identifying surface defects is a difficult, but very desirable, objective. Topographic SFM images help if there is a reliable theoretical "portrait" of each defect for comparison. For example, a theoretical image of an Mg^{2+} ion-cation vacancy pair on the surface of LiF has been calculated by Livshits *et al.* (1999). However, unambiguous identification requires more information. Moreover, for typical concentrations and typical scanning areas (50×50 Å^2), one is unlikely to encounter more than one defect of each kind. Measuring optical absorption usually only confirms the presence of some defect within the sample. To identify a particular defect, one must correlate topographic and spectroscopic signals, for example, by perturbing defect excited states by the SFM tip. Specifically, the SFM probe can alter the balance between radiative and nonradiative defect processes. Scanning near-field optical microscopy aperture probes fabricated using conventional optically transparent SFM tips allows one to obtain topographic images and simultaneously excite surface nanoscale species and collect luminescence in the near field (Nishikawa and Isu, 1999). Very small specially shaped apertures already in use (20 nm across, which is several times smaller than a typical distance for most impurities) should allow one to get an optical signal from isolated defects.

The first theoretical calculations that correlate topographic and luminescence images of the same impurity defect have been performed (Kantorovich, Shluger, and Stoneman, 2000, 2001). They predict a characteristic topographic image of the Cr^{3+} impurity center at the MgO surface in an NC-SFM and a pronounced effect of the SFM tip on its optical properties. The two effects can be correlated, for example, through observation of an enhanced luminescence signal and energy shift when the tip is probing the defect center. The predicted effect would be even stronger for excited defect states that are less localized than those of the Cr ion considered by Kantorovich, Shluger, and Stoneman (2000, 2001). In systems with excited-state lifetimes exceeding the tip oscillation period, changes in the topographic image with electronic state could be observed.

C. Surface magnetism

It is quite fashionable to explain the interest in magnetism, especially on the atomic scale, with the giant investments made in the computer industry to produce reliable and small-scale storage devices (Shen and Kirschner, 2002). Quite apart from this application viewpoint, there is also a scientific interest in the way magnetic properties change with a change of the physical environment. So far, experimental research in this area has been hampered by the low resolution of existing methods [in the range of about 50 nm (Stöhr *et al.*, 1999)]. The combination of experiments with a spin-polarized STM or SFM and refined theoretical models greatly enhances the possibility and quality of data at this extreme limit of resolution.

1. Mn surface

The manganese surface represents a good example of magnetic surface studies in scanning tunneling microscopy where both experiment and theoretical analysis have been performed. The tip in the experiments consisted of a tungsten polycrystal (paramagnetic tip) coated with 10–20 layers of iron (ferromagnetic tip). Contamination of the tip by atoms of the sample surface (manganese) could not be excluded, especially in view of the high tunneling currents of about 40 nA at very-low-bias voltages of 3 mV (Heinze *et al.*, 2000). For this reason a number of separate tips were included in the theoretical analysis (Hofer and Fisher, 2002). The most important ones were as follows: a clean Fe tip, mimicking the polycrystal W wire coated with Fe; an Fe tip contaminated by a single Mn atom (low contamination of the tip); and an Fe tip contaminated with a surface

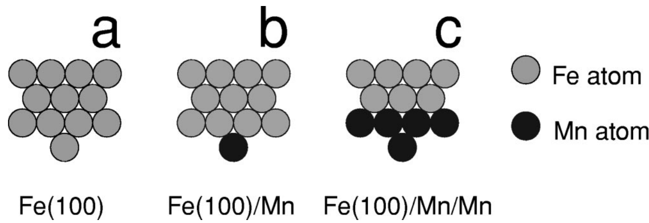

FIG. 29. Scanning tunneling microscope tip models for spin-resolved measurements. The tip model consists of a five-layer Fe(100) film with (a) a single Fe apex atom, (b) a single Mn apex atom, or (c) a Mn layer and a single Mn apex atom. These models mimic a clean ferromagnetic tip or a tip contaminated by surface atoms.

layer and a single Mn atom (high contamination of the tip). On the technical side we note that the free-standing film consisted of five layers with (100) ordering and two additional layers for the apex. The STM tip models are displayed in Fig. 29.

The angle ϕ_M between magnetic axes (see Fig. 30) in the experiments is in general unknown. Therefore images for all possible angles were simulated for a comparison with experimental images. But this also meant that a unique map from angles ϕ_M to corrugation amplitudes could be used to determine the actual angle from the apparent height of the atoms on the surface. We omit displaying the simulated image for the paramagnetic tip model. It is published in Hofer and Fisher (2003).

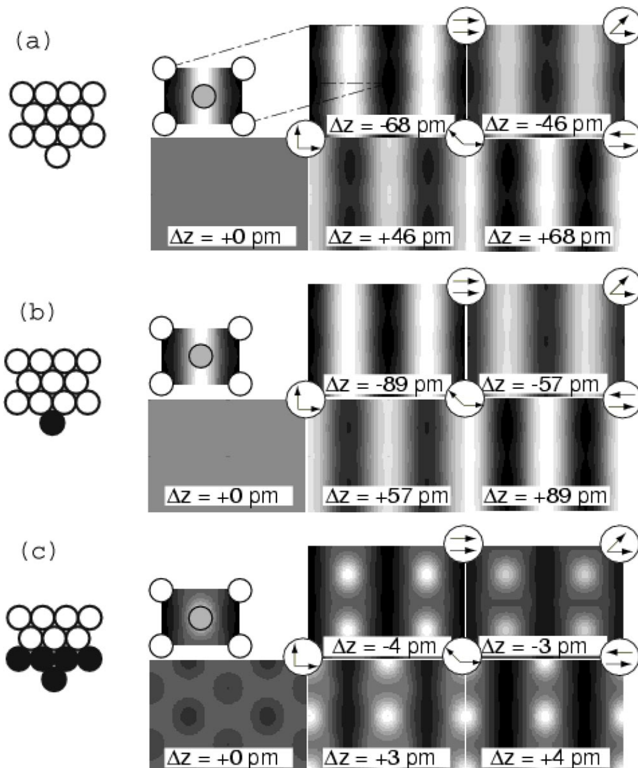

FIG. 30. Simulated STM images of W(110)Mn for three different STM tip models and a range of angles ϕ_M between the magnetic axis of sample and tip. The simulations with (a) a clean tip, and (b) a slightly contaminated tip reveal a surface corrugation well in excess of experimental values, (c) while the highly contaminated tip provides the best agreement with experiments. Reprinted with permission (Hofer and Fisher, 2003).

In practice two separate simulations were performed for every single-tip model and the antiferromagnetic Mn overlayer: one simulation for ferromagnetic ordering in the tunneling transitions $[I_F(x,y,z)]$ and one for antiferromagnetic ordering $[I_A(x,y,z)]$. The two separate current maps were then compiled into a single image by defining an angle ϕ_M from the outset. In Fig. 30 we show the images with three different tips at a median distance of 0.45 nm (the lower limit of stability).

The most remarkable result is the strong dependence of the apparent height of single atoms on the contamination of the STM tip. This is most obvious for the transition from a tip with low contamination [one Mn atom on a Fe(100) surface] to a tip with high contamination (one Mn atom and a surface layer on the surface). The position of individual atoms is only resolved in the simulated images with a highly contaminated surface. The decrease in the apparent height between the atoms was also observed in the experiments. This is not the case for the clean Fe tip or the tip with low Mn contamination. In those cases the relative variation of the constant current contour is too low to be observable. The results prove once again that tip contamination plays a crucial role in the quantitative results obtained in STM experiments. The second point of interest, especially for experimentalists, is the high magnetic contrast of the surface. Considering that close-packed metal surfaces like Mn or Fe are notoriously difficult to image, a coating of the tip by magnetic layers may improve the contrast by more than one order of magnitude. It is also evident that the magnetic contrast vanishes if the magnetic axes of the two surfaces are perpendicular. This entails a strong dependency of the magnetic contrast on ϕ_M, which in turn can be used to study the effect of impurities on the atomic scale and in real space.

2. NiO surface

Due to the well-defined magnetic surface structure and the ease of preparation of an atomically clean surface (Henrich and Cox, 1996), most atomic-scale magnetic studies in scanning force microscopy have focused on the antiferromagnetic nickel oxide (001). The magnetic properties of NiO are well known and various techniques have established the antiferromagnetic AF_2 structure as the most stable, with each Ni ion having two unpaired electrons (Terakura *et al.*, 1984).

As yet, no difference in contrast over opposite-spin Ni ions has been observed with an NC-SFM (Hosoi *et al.*, 2000) with magnetic tips. This directly motivates a theoretical study to investigate the feasibility of measuring the difference in the exchange force over NiO in an experiment and also to establish the criteria for success. Several previous theoretical studies have focused on calculating the magnitude of the exchange force over sim-

pler, metallic magnetic surfaces, such as Fe (Nakamura *et al.*, 1997), Cr, and Ni (Ness and Gautier, 1995), and it is therefore difficult to compare them directly with imaging of NiO.

The most spectacular way to demonstrate experimentally the effect with an NC-SFM would be to measure a difference in contrast along parallel rows of Ni ions with antiparallel spins. However, since the surface sublattice seen as bright in images is unknown *a priori*, this cannot be the only way. A possibly more promising approach might be to measure force vs distance curves above different surface sites. This is within the reach of a low-temperature NC-SFM (Lantz *et al.*, 2000), but requires very high sensitivity, low signal-to-noise ratio, and good statistics. The latter implies repeating these measurements many times over different sites with the same tip. The short range of the exchange interaction means that to reliably measure the difference one may need to advance a tip very close to the surface. This could lead to instability in SFM operation, caused by a too strong tip-surface interaction and by large displacements of the surface/tip atoms and their adhesion to the tip/surface (Livshits *et al.*, 1999). This in turn could lead to tip crashes and prevent reproducible measurements with the same tip.

Combined atomistic simulations and *ab initio* unrestricted Hartree-Fock calculations (Foster and Shluger, 2001) of the interaction of various model magnetic tips with the NiO surface have demonstrated that it should be feasible to measure the difference in exchange force over opposite-spin Ni ions. The calculations predicted a maximum range of 0.375 nm for detecting the difference, with resolution appropriate to a modern low-temperature NC-SFM. However, they also suggested that much greater success would be achieved with tips that weakly chemically interact with the surface, thereby greatly reducing scanning disruption due to ion jumps. Current experiments favor iron-coated silicon tips, but iron is well known to strongly interact with oxide surfaces (Henrich and Cox, 1996).

The study also highlighted the fact that the extreme sensitivity of the low-temperature NC-SFM means that it can atomically resolve the surface via microscopic forces at distances much farther than can a normal NC-SFM. The atomic contrast in frequency change predicted by modeling of the CaF_2 surface (Foster, Barth, *et al.*, 2001) was still about 0.2 Hz at 5.0 Å, so a low-temperature NC-SFM could potentially measure atomic contrast at tip-surface separations in this range. This is too far for the difference in exchange force over spin-up and spin-down Ni ions to be measured, and in real low-temperature NC-SFM experiments atomic resolution of the difference in microscopic force over O and Ni ions will be achieved before it is possible to measure the difference in exchange force over Ni ions. Successful imaging of the exchange force will first require achieving atomic resolution on the surface of NiO at distances where opposite-spin Ni ions appear identical in images. Then the frequency change should be gradually increased to further reduce the shortest tip-surface separation until the exchange force can be measured. This procedure is extremely difficult, but has already been achieved with room-temperature NC-SFM techniques on the CaF_2 surface (Barth *et al.*, 2001) and most recently on the NiO (001) surface itself (Schwarz *et al.*, 2002). However, the absence of exchange contrast suggests that either surface ion instabilities are occurring too early in the tip's approach or the magnetic properties of the tip are not yet fully controlled.

D. Spin manipulation

The most frequently employed STM tips consist of paramagnetic metals (tungsten, platinum, or iridium), in which the tunneling current possesses no spin selectivity. This can be changed in two separate ways: (i) either the signal from a specific spin state is periodically modified by external magnetic fields or (ii) the tip is coated by ferromagnetic or antiferromagnetic metal layers. In case (i), the periodic component of the tunnel current is filtered out by lock-in amplifiers, and the spin signal is directly detected with atomic-scale resolution. A demonstration of this method has recently been given by Durkan and Welland (2002). In these experiments, the spin states of free radicals in an organic molecule were made to precess around the axis of a low-intensity magnetic field with the Larmor frequency. This signal was subsequently isolated in the periodic tunneling current. As the images show, the spin states of the molecule could be resolved with about 1-nm resolution.

Coated tips are used in either spectroscopic or topographic images of magnetic surfaces, in particular, ultrathin magnetic films of one or two layers thickness. The potential of the method has been demonstrated for single and double layers of 3*d* ferromagnetic metals (Fe, Mn) on flat or vicinal W(110) surfaces (Pratzer *et al.*, 2001; Wiesendanger and Bode, 2001). Theoretically, these experiments cannot yet be described by fully quantitative models. Given the importance of magnetoelectronics for industrial applications, this situation is not expected to prevail for very long.

E. Phonon excitations

One aim of surface chemistry is to determine how adsorbates bond to a surface. This can be done by comparing STM topographies and simulations, and by studying the shape of a molecule in both images (Sautet, 1997). But quite frequently this method is not precise enough to identify an adsorption site unambiguously. As surfaces are more and more tailored for particular purposes, this ambiguity needs to be overcome. One method to this end is vibrational spectroscopy, which more and more STM groups are routinely employing. Here, the bias-voltage modulation at the resonance energy of a rotational or vibrational mode of either the molecule or the chemical bond between molecule and surface produces a distinct current spectrum, which can be directly related to the position and the bonding geometry of a molecule (Lauhon and Ho, 1999; Stipe *et al.*,

1999). The theoretical simulations of the method so far have been based on the electronic structure of the surface and molecule alone, and no first-principles simulation of the current and spectrum exists to date (Lorente and Persson, 2000a, 2000b).

F. Electron dynamics

The dynamics of electrons at surfaces and interfaces is studied within many-body theory. Of particular interest are studies of interference effects on surfaces due to scattering at step edges or atoms of a "quantum corral" (Heller *et al.*, 1994; Bürgi *et al.*, 2000; Braun and Rieder, 2002; Fiete and Heller, 2003). The decay of the interference pattern, for example, with increasing distance from a step edge, is an indication of electron-electron and electron-phonon interactions, which reduce the phase memory of the electron. In the context of Fermi-liquid theory this measure is related to the lifetime of a quasiparticle (Bürgi *et al.*, 2000).

Electronic and transport properties of interfaces, buried beneath the surface of a crystal, are often studied by a modified STM based on the principle of ballistic transport (Bell and Kaiser, 1996; de Andres *et al.*, 2001). Initially invented to study the Schottky barrier (Zangwill, 1988) of a metal-semiconductor interface (Bell and Kaiser, 1988), it is currently employed to gain a systematic understanding of electron-electron interactions in solids. The most advanced theoretical models in this field are based on the nonequilibrium Green's-function formalism of Keldysh (Keldysh, 1965; de Andres *et al.*, 2001).

VII. CONCLUSION AND OUTLOOK

Quantitative methods developed for analysis of SPM images reflect the changes in the field from the earliest experiments on Si(111) surfaces until today. The cutting edge in theory is now an exact description of currents, forces, and inelastic effects. The most striking results are achieved where experiment and theory can combine to reveal the atomic processes being imaged. However, this requires immense sophistication from both sides and has so far rarely been achieved. Further progress in this field should eventually allow us to study not only surface topography, but also surface dynamics, excitations, and chemical processes. An essential ingredient for the successful characterization of any surface process remains the development of methods for a quantitative comparison between theory and experiment.

Although the theoretical methods used to simulate scanning probe microscopy can vary widely, they share certain traits and challenges. These include the inability to treat satisfactorily the real structure of the tip. Even though theoretical analysis has proved to be very useful in determining the tip-sample separation in STM and SFM experiments, it still remains problematic in both techniques. As yet, no reliable error estimate of simulation methods exists. Tip and surface atomic relaxation have proved to be so crucial to imaging that they are increasingly included. Only in this way can the distance-dependent contrast observed in both STM and SFM be accounted for.

Finally, we note that parallel analysis of the STM and SFM work presented here clearly demonstrates many similar features. With the development of combined STM/SFM machines both techniques will come even closer together and, with a little cross-fertilization by theoretical insight, will serve as increasingly powerful tools in surface and nanoscience.

ACKNOWLEDGMENTS

A.S.F. and A.L.S. would like to thank C. Barth and M. Reichling for their extensive collaboration and advice. We would like to thank W. Allers, T. Arai, A. Baratoff, R. Bennewitz, A. Biedermann, T. Bitzer, M. Bode, J. Cerda, A. Fisher, J. D. Gale, F. Giessibl, H. Guo, R. Hoffmann, H. Hölscher, H. Hug, L. N. Kantorovich, G. Kresse, E. Meyer, H. Ness, C. Pang, R. Perez, J. Pethica, R. Podloucky, J. Polanyi, R. Raval, J. Redinger, N. Richardson, A. L. Rohl, N. Sasaki, M. Schmid, U. D. Schwarz, R. Stadler, G. Thornton, M. Tsukada, P. Varga, R. Wiesendanger, and R. Wolkow for useful discussions during the course of this work. We are grateful to S. Fain, P. Gruetter, A. Schwarz, K. Stokbro, and A. M. Stoneham for helpful comments on the manuscript. A.S.F. has been supported by the Academy of Finland through its Centres of Excellence Program (2000–2005). We are grateful to EPSRC and the British Council for financial support.

REFERENCES

Aimé, J. P., R. Boisgard, L. Nony, and G. Couturier, 1999, Phys. Rev. Lett. **82**, 3388.
Allers, W., S. Langkat, and R. Wiesendanger, 2001, Appl. Phys. A: Mater. Sci. Process. **72**, S27.
Allers, W., A. Schwarz, U. D. Schwarz, and R. Wiesendanger, 1998, Rev. Sci. Instrum. **69**, 221.
Allers, W., A. Schwarz, U. D. Schwarz, and R. Wiesendanger, 1999, Europhys. Lett. **48**, 276.
Aoki, T., Y. Sowa, H. Yokota, M. Hiroshima, M. Tokunaga, Y. Ishii, and T. Yanagida, 2001, Single Mol. **2**, 183.
Argento, C., and R. H. French, 1996, J. Appl. Phys. **80**, 6081.
Ashino, M., Y. Sugawara, S. Morita, and M. Ishikawa, 2001, Phys. Rev. Lett. **86**, 4334.
Badziag, P., W. S. Verwoed, and M. A. van Hove, 1991, Phys. Rev. B **43**, 2058.
Bammerlin, M., R. Lüthi, E. Meyer, A. Baratoff, M. Guggisberg, C. Gerber, L. Howald, and H.-J. Güntherodt, 1997, Probe Microsc. **1**, 3.
Bammerlin, M., R. Lüthi, E. Meyer, J. Lü, M. Guggisberg, C. Loppacher, C. Gerber, and H. J. Güntherodt, 1998, Appl. Phys. A: Mater. Sci. Process. **66**, S293.
Bardeen, J., 1961, Phys. Rev. Lett. **6**, 57.
Barth, C., A. S. Foster, M. Reichling, and A. L. Shluger, 2001, J. Phys.: Condens. Matter **13**, 2061.
Barth, C., and M. Reichling, 2001, Nature (London) **414**, 54.
Behm, R. J., N. Garcia, and H. Rohrer, 1990, *Scanning Tunneling Microscopy and Related Methods* (Kluwer, Dordrecht).

Bell, L. D., and W. J. Kaiser, 1988, Phys. Rev. Lett. **61**, 2368.
Bell, L. D., and W. J. Kaiser, 1996, Annu. Rev. Mater. Sci. **26**, 189.
Bennewitz, R., M. Bammerlin, M. Guggisberg, C. Loppacher, A. Baratoff, E. Meyer, and H.-J. Güntherodt, 1999a, Surf. Interface Anal. **27**, 462.
Bennewitz, R., M. Bammerlin, M. Guggisberg, C. Loppacher, A. Baratoff, E. Meyer, and H.-J. Güntherodt, 1999b, Surf. Sci. **438**, 289.
Bennewitz, R., A. S. Foster, L. N. Kantorovich, M. Bammerlin, C. Loppacher, S. Schär, M. Guggisberg, E. Meyer, and A. L. Shluger, 2000, Phys. Rev. B **62**, 2074.
Bennewitz, R., M. Reichling, and E. Matthias, 1997, Surf. Sci. **387**, 69.
Bennewitz, R., S. Schaar, V. Barvich, O. Pfeiffer, E. Meyer, B. Such, F. Krok, J. Kolodziej, and M. Szymonski, 2001, Surf. Sci. **474**, L197.
Biedermann, A., 1991, *Instrumentelle Optimierung eines Ultrahochvakuum- Rastertunnelmikroskops und Messungen an Graphit- and Silizium- und Platin-Nickel-Einkristalloberflächen* (Diplomarbeit and Technische Universität, Wien).
Biedermann, A., O. Genser, W. Hebenstreit, M. Schmid, R. P. J. Redinger, and P. Varga, 1996, Phys. Rev. Lett. **76**, 4179.
Binks, D. J., 1994, Ph.D. thesis (University of Surrey).
Binnig, G., N. Garcia, H. Rohrer, J. M. Soler, and F. Flores, 1984, Phys. Rev. B **30**, 4816.
Binnig, G., C. Quate, and C. Gerber, 1986, Phys. Rev. Lett. **56**, 930.
Binnig, G., and H. Rohrer, 1982, Helv. Phys. Acta **55**, 726.
Binnig, G., H. Rohrer, C. Gerber, and E. Weibel, 1982a, Appl. Phys. Lett. **40**, 178.
Binnig, G., H. Rohrer, C. Gerber, and E. Weibel, 1982b, Phys. Rev. Lett. **49**, 57.
Binnig, G., H. Rohrer, C. Gerber, and E. Weibel, 1983, Phys. Rev. Lett. **50**, 120.
Bischoff, M. M. J., C. Konvicka, A. J. Quinn, M. Schmid, J. Redinger, R. Podloucky, P. Varga, and H. van Kempen, 2001, Phys. Rev. Lett. **86**, 2396.
Bitzer, T., T. Rada, and N. V. Richardson, 2001, J. Phys. Chem. B **105**, 4535.
Bonnell, D. A., 2000, *Probe Microscopy and Spectroscopy: Theory, Techniques and Applications* (Wiley, New York).
Braun, K. F., and K. H. Rieder, 2002, Phys. Rev. Lett. **88**, 096801.
Briggs, G. A. D., and A. J. Fisher, 1999, Surf. Sci. Rep. **33**, 1.
Briggs, G. A. D., J. Knall, A. J. Mayne, T. S. Jones, W. H. Weinberg, and A. R. Avery, 1992, Nanotechnology **3**, 113.
Bringans, R. D., R. I. G. Uhrberg, A. Olmstaed, and R. Z. Bachrach, 1986, Phys. Rev. B **34**, 7447.
Bürgi, L., H. Brune, O. Jeandupeux, and K. Kern, 2000, J. Electron Spectrosc. Relat. Phenom. **109**, 33.
Burnham, N., R. Colton, and H. Pollock, 1992, Phys. Rev. Lett. **69**, 144.
Burnham, N., R. Colton, and H. Pollock, 1993, Nanotechnology **4**, 64.
Bush, T. S., J. D. Gale, C. R. A. Catlow, and P. D. Battle, 1994, J. Mater. Chem. **4**, 832.
Bütticker, M., Y. Imry, R. Landauer, and S. Pinhas, 1985, Phys. Rev. B **31**, 6207.
Capella, B., and G. Dietler, 1999, Surf. Sci. Rep. **34**, 1.
Catlow, C. R. A., and W. C. Mackrodt, 1982, *Computer Simulation of Solids* (Springer, Berlin).
Cerda, J., M. van Hove, P. Sautet, and M. Salmeron, 1997, Phys. Rev. B **56**, 15 885.
Cerda, J., and F. Soria, 2000, Phys. Rev. B **61**, 7965.
Chen, J. C., 1990a, Phys. Rev. Lett. **65**, 448.
Chen, J. C., 1990b, Phys. Rev. B **42**, 8841.
Chen, J. C., 1993, *Introduction to Scanning Tunneling Microscopy* (Oxford University, Oxford).
Cho, K., and J. D. Joannopoulos, 1993, Phys. Rev. Lett. **71**, 1387.
Clarke, A. R. H., J. B. Pethica, J. A. Nieminen, F. Besenbacher, E. Laegsgaard, and I. Stensgaard, 1996, Phys. Rev. Lett. **76**, 1276.
Crommie, M. F., C. P. Lutz, and D. M. Eigler, 1993, Phys. Rev. B **48**, 2851.
Cross, G., A. Schirmeisen, A. Stalder, P. Grutter, M. Tschudy, and U. Dürig, 1998, Phys. Rev. Lett. **80**, 4685.
Dabrowski, J., and M. Scheffler, 1992, Appl. Surf. Sci. **56-58**, 15.
de Andres, P. L., F. J. Garcia-Vidal, K. Reuter, and F. Flores, 2001, Prog. Surf. Sci. **66**, 3.
de Leeuw, N. H., and S. C. Parker, 1997, J. Chem. Soc., Faraday Trans. **93**, 467.
Dick, B. G., and A. W. Overhauser, 1958, Phys. Rev. **112**, 603.
Driscoll, R. J., M. G. Youngquist, and J. D. Baledschwieler, 1990, Nature (London) **346**, 294.
Dürig, U., 2000, New J. Phys. **2**, 5.
Durkan, C., and M. E. Welland, 2002, Appl. Phys. Lett. **80**, 458.
Engel, A., and D. J. Müller, 2000, Nat. Struct. Biol. **7**, 715.
Engelhardt, J. B., H. Dabringhaus, and K. Wandelt, 2000, Surf. Sci. **448**, 187.
Erlandsson, R., L. Olsson, and P. Mártensson, 1996, Phys. Rev. B **54**, R8309.
Feenstra, R. M., J. A. Stroscio, and A. P. Fein, 1987, Surf. Sci. **181**, 295.
Feuchtwang, T. E., 1974, Phys. Rev. B **10**, 4135.
Feuchtwang, T. E., 1975, Phys. Rev. B **12**, 3979.
Feuchtwang, T. E., 1976, Phys. Rev. B **13**, 517.
Fiete, G. A., and E. J. Heller, 2003, Rev. Mod. Phys. **75**, 933.
Fölsch, S., A. Helms, S. Zöphel, J. Repp, G. Meyer, and K. Rieder, 2000, Phys. Rev. Lett. **84**, 123.
Foster, A. S., C. Barth, A. L. Shluger, R. M. Nieminen, and M. Reichling, 2002, Phys. Rev. B **66**, 235417.
Foster, A. S., C. Barth, A. L. Shluger, and M. Reichling, 2001, Phys. Rev. Lett. **86**, 2373.
Foster, A. S., W. A. Hofer, and A. L. Shluger, 2001, Curr. Opin. Solid State Mater. Sci. **5**, 427.
Foster, A. S., L. N. Kantorovich, and A. L. Shluger, 2000, Appl. Phys. A: Mater. Sci. Process. **72**, S59.
Foster, A. S., A. L. Rohl, and A. L. Shluger, 2000, Appl. Phys. A: Mater. Sci. Process. **72**, S31.
Foster, A. S., and A. L. Shluger, 2001, Surf. Sci. **490**, 211.
French, R. H., R. M. Cannon, L. K. DeNoyer, and Y. M. Chiang, 1995, Solid State Ionics **75**, 13.
Fukui, K., H. Onishi, and Y. Iwasawa, 1997a, Phys. Rev. Lett. **79**, 4202.
Fukui, K., H. Onishi, and Y. Iwasawa, 1997b, Chem. Phys. Lett. **280**, 296.
García, R., and R. Pérez, 2002, Surf. Sci. Rep. **47**, 197.
Gauthier, M., and M. Tsukada, 1999, Phys. Rev. B **60**, 11 716.
Gay, D. H., and A. L. Rohl, 1995, J. Chem. Soc., Faraday Trans. **91**, 925.
Giessibl, F. J., 1994, Jpn. J. Appl. Phys., Part 1 **33**, 3726.

Giessibl, F. J., 1995, Science **267**, 68.
Giessibl, F. J., 1997, Phys. Rev. B **56**, 16 010.
Giessibl, F. J., 2003, Rev. Mod. Phys. **75**, 949.
Giessibl, F. J., H. Bielefeldt, S. Hembacher, and J. Mannhart, 1999, Appl. Surf. Sci. **140**, 352.
Giessibl, F. J., S. Hembacher, H. Bielefeldt, and J. Mannhart, 2000, Science **289**, 422.
Gimzewski, J. K., and R. Moeller, 1987, Phys. Rev. B **36**, 1284.
Glöckler, K., M. Sokolowski, A. Soukopp, and E. Umbach, 1996, Phys. Rev. B **54**, 7705.
Gomez-Moñivas, S., L. S. Froufe-Pérez, A. J. Caamaño, and J. J. Sáenz, 2001, Appl. Phys. Lett. **79**, 4048.
Grimes, R., C. Catlow, and A. Stoneham, 1989, J. Phys.: Condens. Matter **1**, 7367.
Guggisberg, M., M. Bammerlin, C. Loppacher, O. Pfeiffer, A. Abdurixit, V. Barwich, R. Bennewitz, A. Baratoff, E. Meyer, and H.-J. Güntherodt, 2000, Phys. Rev. B **61**, 11 151.
Güntherodt, H.-J., D. Anselmetti, and E. Meyer, 1995, Eds., *Forces in Scanning Probe Methods* (Kluwer, Dordrecht).
Hahn, J. R., and W. Ho, 2001a, Phys. Rev. Lett. **87**, 166102.
Hahn, J. R., and W. Ho, 2001b, Phys. Rev. Lett. **87**, 196102.
Hallmark, V. M., S. Chiang, J. F. Raboli, J. D. Swalen, and R. J. Wilson, 1987, Phys. Rev. Lett. **59**, 2879.
Hamaker, H. C., 1937, Physica (Utrecht) **4**, 1058.
Hamers, R. J., R. M. Tromp, and J. E. Demuth, 1986, Phys. Rev. B **34**, 5343.
Hansen, O., S. Ravnkilde, U. Quaade, K. Stokbro, and F. Grey, 1998, Phys. Rev. Lett. **81**, 5572.
Harris, L. B., and J. Fiasson, 1985, J. Phys. C **18**, 4845.
Hata, K., S. Yasuda, and H. Shigekawa, 1999, Phys. Rev. B **60**, 8164.
Hebenstreit, W., J. Redinger, Z. Horozova, M. Schmid, R. Podloucky, and P. Varga, 1999, Surf. Sci. **424**, L321.
Hebenstreit, W., M. Schmid, J. Redinger, and P. Varga, 2000, Phys. Rev. Lett. **85**, 5376.
Heinze, S., M. Bode, A. Kubetzka, O. Peitzsch, X. Nie, S. Blügel, and R. Wiesendanger, 2000, Science **288**, 1805.
Heller, E. J., M. F. Crommie, C. P. Lutz, and D. M. Eigler, 1994, Nature (London) **369**, 464.
Henrich, V. E., and P. A. Cox, 1996, *The Surface Science of Metal Oxides* (Cambridge University, Cambridge).
Heywood, B. R., 1996, *Biomimetic Materials Chemistry* (VCH, New York).
Hillner, P. E., A. J. Gratz, S. Manne, and P. K. Hansma, 1992, Geology **20**, 359.
Himpsel, F. J., J. E. Ortega, G. J. Mankey, and R. F. Willis, 1998, Adv. Phys. **47**, 511.
Hla, S.-W., L. Bartels, G. Meyer, and K.-H. Rieder, 2000, Phys. Rev. Lett. **85**, 2777.
Hofer, W. A., and A. J. Fisher, 2002, Surf. Sci. Lett. **515**, L487.
Hofer, W. A., and A. J. Fisher, 2003, Phys. Rev. Lett. **91**, 036803.
Hofer, W. A., A. J. Fisher, T. Bitzer, T. Rada, and N. V. Richardson, 2002, Chem. Phys. Lett. **355**, 347.
Hofer, W. A., A. J. Fisher, G. R. Lopinski, and R. A. Wolkow, 2001, Phys. Rev. B **63**, 085314.
Hofer, W. A., A. J. Fisher, R. A. Wolkow, and P. Grütter, 2001, Phys. Rev. Lett. **87**, 236104.
Hofer, W. A., and J. Redinger, 2000, Surf. Sci. **447**, 51.
Hofer, W. A., J. Redinger, A. Biedermann, and P. Varga, 2000, Surf. Sci. Lett. **466**, L795.
Hofer, W. A., J. Redinger, and R. Podloucky, 2001, Phys. Rev. B **64**, 125108.
Hofer, W. A., J. Redinger, and P. Varga, 1999, Solid State Commun. **113**, 245.
Hofer, W. A., G. Ritz, W. Hebenstreit, M. Schmid, P. Varga, J. Redinger, and R. Podloucky, 1998, Surf. Sci. Lett. **405**, L514.
Hoffmann, P., S. Jeffrey, J. B. Pethica, H. O. Özer, and A. Oral, 2001, Phys. Rev. Lett. **87**, 265502.
Hoffmann, R., M. A. Lantz, H. J. Hug, P. J. A. van Schendel, P. Kappenberger, S. Martin, A. Baratoff, and H. J. Güntherodt, 2002, Appl. Surf. Sci. **188**, 238.
Hölscher, H., W. Allers, U. D. Schwarz, A. Schwarz, and R. Wiesendanger, 2000, Phys. Rev. B **62**, 6967.
Hölscher, H., B. Gotsmann, W. Allers, U. D. Schwarz, H. Fuchs, and R. Wiesendanger, 2001, Phys. Rev. B **64**, 075402.
Hosoi, H., K. Sueoka, K. Hayakawa, and K. Mukasa, 2000, Appl. Surf. Sci. **157**, 218.
Hudlet, S., M. S. Jean, B. Roulet, J. Berger, and C. Guthmann, 1995, J. Appl. Phys. **77**, 3308.
Inglesfield, J. E., 1982, Rep. Prog. Phys. **45**, 223.
Israelachvili, J., 1991, *Intermolecular and Surface Forces* (Academic, London).
Jacobs, H. O., and A. Stemmer, 1999, Surf. Interface Anal. **27**, 361.
James, P. J., M. Antognozzi, J. Tamayo, T. J. McMaster, J. M. Newton, and M. J. Miles, 2001, Langmuir **17**, 349.
Jandt, K. D., 2001, Surf. Sci. **491**, 303.
Jean, M. S., S. Hudlet, C. Guthmann, and J. Berger, 1999, J. Appl. Phys. **86**, 5245.
Kantorovich, L. N., A. S. Foster, A. L. Shluger, and A. M. Stoneham, 2000, Surf. Sci. **445**, 283.
Kantorovich, L. N., A. L. Shluger, and A. M. Stoneham, 2000, Phys. Rev. Lett. **85**, 3846.
Kantorovich, L. N., A. L. Shluger, and A. M. Stoneham, 2001, Phys. Rev. B **63**, 184111.
Ke, S. H., T. Uda, R. Pérez, I. Stich, and K. Terakura, 1999, Phys. Rev. B **60**, 11 631.
Ke, S. H., T. Uda, I. Stich, and K. Terakura, 2001, Phys. Rev. B **63**, 245323.
Ke, S. H., T. Uda, and K. Terakura, 2002, Phys. Rev. B **65**, 125417.
Keldysh, L. V., 1965, Sov. Phys. JETP **20**, 1018.
Kliewer, J., and R. Berndt, 2002, Phys. Rev. B **65**, 035412.
Kresse, G., and J. Furthmüller, 1996, Phys. Rev. B **54**, 11 169.
Kresse, G., and J. Hafner, 1993, Phys. Rev. B **47**, 558.
Lang, N. D., 1988, Phys. Rev. B **37**, 10 395.
Lantz, M. A., H. J. Hug, R. Hoffman, P. J. A. van Schendel, P. Kappenberger, S. Martin, A. Baratoff, and H. J. Güntherodt, 2001, Science **291**, 2580.
Lantz, M. A., H. J. Hug, P. J. A. van Schendel, R. Hoffman, S. Martin, A. Baratoff, A. Abdurixit, H. J. Güntherodt, and C. Gerber, 2000, Phys. Rev. Lett. **84**, 2642.
Lauhon, L., and W. Ho, 1999, Phys. Rev. B **60**, R8525.
Lauhon, L. J., and W. Ho, 2000, Phys. Rev. Lett. **85**, 4566.
Lemay, S. G., J. W. Janssen, M. van den Hout, M. Mooij, M. J. Bronikowski, P. A. Willis, R. E. Smalley, L. P. Kouwenhoven, and C. Dekker, 2001, Nature (London) **412**, 617.
Liang, Y., A. S. Lea, D. R. Baer, and M. H. Engelhard, 1996, Surf. Sci. **351**, 172.
Livshits, A. I., and A. L. Shluger, 1997a, Phys. Rev. B **56**, 12 482.
Livshits, A. I., and A. L. Shluger, 1997b, Faraday Discuss. **106**, 425.
Livshits, A. I., A. L. Shluger, A. L. Rohl, and A. S. Foster, 1999, Phys. Rev. B **59**, 2436.

London, F., 1937, Trans. Faraday Soc. **33**, 8.
Loppacher, C., M. Bammerlin, M. Guggisberg, S. Scär, R. Bennewitz, A. Baratoff, E. Meyer, and H. J. Güntherodt, 2000, Phys. Rev. B **62**, 16 944.
Lorente, N., and M. Persson, 2000a, Faraday Discuss. **117**, 277.
Lorente, N., and M. Persson, 2000b, Phys. Rev. Lett. **85**, 2997.
Lucas, A. A., 1990, Europhys. News **21**, 63.
Luna, M., F. Rieutord, N. A. Melman, Q. Dai, and M. Salmeron, 1998, J. Phys. Chem. A **102**, 6793.
Martin, Y., C. C. Williams, and H. K. Wickramasinghe, 1987, J. Appl. Phys. **61**, 4723.
Meir, Y., and N. S. Wingreen, 1992, Phys. Rev. Lett. **68**, 2512.
Molinas-Mata, P., A. J. Mayne, and G. Dujardin, 1998, Phys. Rev. Lett. **80**, 3101.
Morita, S., R. Wiesendanger, and E. Meyer, 2002, Eds., *Noncontact Atomic Force Microscopy* (Springer, Berlin).
Mulliken, R. S., 1949, J. Chim. Phys. Phys.-Chim. Biol. **49**, 497.
Nakamura, K., H. Hasegawa, T. Oguchi, K. Sueoka, K. Hayakawa, and K. Mukasa, 1997, Phys. Rev. B **56**, 3218.
Nakamura, K., T. Oguchi, H. Hasegawa, K. Sueoka, K. Hayakawa, and K. Mukasa, 1999, Appl. Phys. Lett. **140**, 243.
Ness, H., and A. Fisher, 1997a, Phys. Rev. B **55**, 10 081.
Ness, H., and A. Fisher, 1997b, Phys. Rev. B **56**, 12 469.
Ness, H., and F. Gautier, 1995, Phys. Rev. B **52**, 7352.
Nishiguchi, T., M. Kageshima, N. Ara-Kato, and A. Kawazu, 1998, Phys. Rev. Lett. **81**, 3187.
Nishikawa, S., and T. Isu, 1999, J. Microsc. **194**, 415.
Nishino, T., P. Bühlmann, T. Ito, and Y. Umezawa, 2001, Surf. Sci. Lett. **490**, L579.
Ohnesorge, F., and G. Binnig, 1993, Science **260**, 1451.
Ohno, K., K. Esfarjani, and Y. Kawazoe, 1999, *Computational Materials Science* (Springer, Berlin).
Pavese, A., M. Catti, S. C. Parker, and A. Wall, 1996, Phys. Chem. Miner. **23**, 89.
Payne, M. C., and J. C. Inkson, 1985, Surf. Sci. **159**, 485.
Payne, M. C., N. Roberts, R. J. Needs, M. Needels, and J. D. Joannopoulos, 1989, Surf. Sci. **211**, 1.
Pérez, R., M. Payne, I. Stich, and K. Terakura, 1997, Phys. Rev. Lett. **78**, 678.
Pérez, R., I. Stich, M. Payne, and K. Terakura, 1998, Phys. Rev. B **58**, 10 835.
Pethica, J. B., and A. P. Sutton, 1988, J. Vac. Sci. Technol. A **6**, 2490.
Philippsen, A., W. Im, A. Engel, T. Schirmer, B. Roux, and D. J. Muller, 2002, Biophys. J. **82**, 1667.
Piezsch, O., A. Kubetzka, M. Bode, and R. Wiesendanger, 2001, Science **292**, 2053.
Pratzer, M., H. J. Elmers, M. Bode, O. Pietzsch, A. Kubetzka, and R. Wiesendanger, 2001, Phys. Rev. Lett. **87**, 127201.
Reichling, M., and C. Barth, 1999, Phys. Rev. Lett. **83**, 768.
Reuter, K., P. L. de Andres, F. J. Garcia-Vidal, and F. Flores, 2001, Phys. Rev. B **63**, 205325.
Sacks, W., 2000, Phys. Rev. B **61**, 7656.
Sacks, W. S., and C. Noguera, 1988, J. Microsc. **152**, 23.
Sasahara, A., H. Uetsuka, and H. Onishi, 2001, J. Phys. Chem. B **105**, 1.
Sasaki, N., and M. Tsukada, 1999, Appl. Surf. Sci. **140**, 339.
Sautet, P., 1997, Chem. Rev. (Washington, D.C.) **97**, 1097.
Schintke, S., S. Messerli, M. Pivetta, F. Patthey, L. Libouille, M. Stengel, A. de Vita, and W.-D. Schneider, 2001, Phys. Rev. Lett. **87**, 276801.
Schmid, M., 1998, http://www.iap.tuwien.ac.at/www/surface/STM_Gallery//stm_schematic.html
Schmid, M., H. Stadler, and P. Varga, 1993, Phys. Rev. Lett. **70**, 1441.
Schulz, J. J., M. Sturmat, and R. Koch, 2000, Phys. Rev. B **62**, 15 402.
Schuster, R., J. V. Barth, J. Wintterlin, R. J. Behm, and G. Ertl, 1992, Ultramicroscopy **42**, 533.
Schwarz, A., W. Allers, U. D. Schwarz, and R. Wiesendanger, 2000, Phys. Rev. B **61**, 2837.
Schwarz, U. D., H. Hölscher, and R. Wiesendanger, 2000, Phys. Rev. B **62**, 13 089.
Schwarz, A., U. D. Schwarz, S. Langkat, H. Hölscher, W. Allers, and R. Wiesendanger, 2002, Appl. Surf. Sci. **188**, 245.
Shen, J., and J. Kirschner, 2002, Surf. Sci. **500**, 300.
Shindo, H., and H. Nozoye, 1992, J. Chem. Soc., Faraday Trans. **88**, 711.
Shluger, A. L., L. N. Kantorovich, A. I. Livshits, and M. J. Gillan, 1997, Phys. Rev. B **56**, 15 332.
Shluger, A. L., A. I. Livshits, A. S. Foster, and C. R. A. Catlow, 1999, J. Phys.: Condens. Matter **11**, R295.
Shluger, A. L., and A. L. Rohl, 1996, Top. Catal. **3**, 221.
Shluger, A. L., A. L. Rohl, D. H. Gay, and R. T. Williams, 1994, J. Phys.: Condens. Matter **6**, 1825.
Skinner, A. J., J. P. LaFemina, and H. J. F. Jansen, 1994, Am. Mineral. **79**, 205.
Sounilhac, S., E. Barthel, and F. Creuzet, 1999, Appl. Surf. Sci. **140**, 411.
Stipe, B., M. Rezaei, and W. Ho, 1999, Phys. Rev. Lett. **82**, 1724.
Stipp, S. L. S., 1999, Geochim. Cosmochim. Acta **63**, 3121.
Stipp, S. L. S., C. M. Eggleston, and B. S. Nielsen, 1994, Geochim. Cosmochim. Acta **58**, 3023.
Stipp, S. L. S., and M. F. Hochella, Jr., 1991, Geochim. Cosmochim. Acta **55**, 1723.
Stöhr, J., A. Scholl, T. J. Regan, S. Anders, J. Lining, M. R. Scheinfein, H. A. Padmore, and R. L. White, 1999, Phys. Rev. Lett. **83**, 1862.
Stokbro, K., C. Thirstrup, M. Sakurai, U. Quaade, B. Y.-K. Hu, F. Perez-Murano, and F. Grey, 1998, Phys. Rev. Lett. **80**, 2618.
Stroscio, J. A., D. T. Pierce, A. Davies, R. J. Celotta, and M. Weinert, 1995, Phys. Rev. Lett. **75**, 2960.
Sugawara, Y., M. Ohta, H. Ueyama, and S. Morita, 1995, Science **270**, 1648.
Suresh, L., and J. Y. Walz, 1996, J. Colloid Interface Sci. **183**, 199.
Sushko, P. V., A. S. Foster, L. N. Kantorovich, and A. L. Shluger, 1999, Appl. Surf. Sci. **144-145**, 608.
Tagami, K., N. Sasaki, and M. Tsukada, 2000, J. Phys. Soc. Jpn. **69**, 3937.
Tagami, K., and M. Tsukada, 2000, Jpn. J. Appl. Phys., Part 1 **39**, 6025.
Taylor, J., H. Guo, and J. Wang, 2001, Phys. Rev. B **63**, 245407.
Terakura, K., A. R. Williams, T. Oguchi, and J. Kübler, 1984, Phys. Rev. B **30**, 4734.
Tersoff, J., and D. R. Hamann, 1985a, Phys. Rev. Lett. **50**, 1998.
Tersoff, J., and D. R. Hamann, 1985b, Phys. Rev. B **31**, 805.
Tóbik, J., I. Stich, R. Pérez, and K. Terakura, 1999, Phys. Rev. B **60**, 11 639.
Tóbik, J., I. Stich, and K. Terakura, 2001, Phys. Rev. B **63**, 245324.
Todorov, T., J. Hoekstra, and A. P. Sutton, 2000, Philos. Mag. B **80**, 421.

Touhari, F., X. Bouju, C. Girard, M. Devel, and G. Cohen-Solal, 1998, Appl. Surf. Sci. **125**, 351.

Turchi, P. E. A., A. Gonis, and L. Colombo, 1998, Eds., *Tight-Binding Approach to Computational Materials Science* (Materials Research Society, Warrendale, PA).

Uchihashi, T., Y. Sugawara, T. Tsukamoto, T. Minobe, S. Orisaka, T. Okada, and S. Morita, 1999, Appl. Surf. Sci. **140**, 304.

Uozumi, T., Y. Tomiyoshi, N. Suehira, Y. Sugawara, and S. Morita, 2002, Appl. Surf. Sci. **188**, 279.

Ventra, M. D., and S. T. Pantelides, 1999, Phys. Rev. B **59**, R5320.

Wertz, M. P. L., E. W. van der Vegte, and G. Hadziioannou, 1997, Langmuir **13**, 4939.

Wiesendanger, R., and M. Bode, 2001, Solid State Commun. **119**, 341.

Wiesendanger, R., H. J. Güntherodt, R. J. Gambino, and R. Ruf, 1990, Phys. Rev. Lett. **65**, 247.

Wille, L. T., and P. J. Durham, 1985, Surf. Sci. **164**, 19.

Wimmer, E., H. Krakauer, and A. J. Freeman, 1985, Adv. Electron. Electron Phys. **65**, 357.

Wintle, H. J., 1997, Meas. Sci. Technol. **8**, 508.

Wolkow, R. A., 1992, Phys. Rev. Lett. **68**, 2636.

Wolkow, R. A., 1999, Annu. Rev. Phys. Chem. **50**, 413.

Wouda, P. T., B. E. Nieuwenhuys, M. Schmid, and P. Varga, 1996, Surf. Sci. **359**, 17.

Zaibi, M., J. Lacharme, and C. Sebenne, 1997, Surf. Sci. **377**, 639.

Zanette, S. I., A. O. Caride, V. B. Nunes, G. L. Klimchitskaya, F. L. Freire, Jr., and R. Prioli, 2000, Surf. Sci. **453**, 75.

Zangwill, A., 1988, *Physics at Surfaces* (Cambridge University, Cambridge).